Multiple Monoenergetic Gamma Radiography (MMGR) using compact superconducting cyclotron

by
Hin Yeung Lee
B.S., University of California, Berkeley (2015)

Submitted to the Department of Nuclear Science and Engineering
in partial fulfillment of the requirements for the degree of
Doctor of Philosophy in Nuclear Science and Engineering
at the
MASSACHUSETTS INSTITUTE OF TECHNOLOGY
May 2020

Author .....
Hin Yeung Lee
Department of Nuclear Science and Engineering
May 4, 2020

Certified by .....
Areg Danagoulian
Associate Professor of Nuclear Science and Engineering
Thesis Supervisor

Certified by .....
Richard C. Lanza
Senior Research Scientist, Nuclear Science and Engineering
Thesis Reader

Certified by .....
Zachary S. Hartwig
John C. Hardwick Assistant Professor of Nuclear Science
and Engineering
Research Committee

Accepted by .....
Ju Li
Battelle Energy Alliance Professor of Nuclear Science and Engineering
and Professor of Materials Science and Engineering
Chair, Department Committee on Graduate Students

Multiple Monoenergetic Gamma Radiography (MMGR) using compact superconducting cyclotron

by

Hin Yeung Lee

Submitted to the Department of Nuclear Science and Engineering
on May 4, 2020, in partial fulfillment of the
requirements for the degree of
Doctor of Philosophy in Nuclear Science and Engineering

Abstract

Smuggling of special nuclear materials (SNM) and nuclear devices through borders and ports of entry constitutes a major risk to global security. Reliable technologies are imperative for screening the flow of commerce for the presence of high-Z materials such as uranium and plutonium. This thesis presents an experimental proof-of-concept system using low energy $(p, p'\gamma)$ nuclear reactions to generate monoenergetic photons to provide a means to measure the areal density and the effective atomic number (Z_{eff}) of an object with accuracy that surpasses existing interrogation methods and other major deployed systems. This radiography system was designed using an ION-12$^{\text{SC}}$ compact superconducting 12 MeV proton cyclotron. Using a specially designed hybrid graphite water target, monoenergetic photons were generated at 4.4, 6.1, 6.9, and 7.1 MeV from $(p, p'\gamma)$ nuclear reactions. By performing GEANT4 simulations and numerical integration on existing cross sections, the gamma yield from MMGR are shown to be comparable to the X-ray yield from a bremsstrahlung-based system, with the advantage of lower radiation dose using MMGR. In a series of MMGR experiments using 4.4, 6.1, 6.9, and 7.1 MeV gammas, the author gamma transmission spectra on a variety of homogeneous (Z from 13-92) and heterogeneous mock cargoes. With the newly developed reconstruction algorithm, the author accurately predicted the areal density and Z_{eff} of the experimental cargoes with an average Z_{eff} reconstruction accuracy of 3.7 and an uncertainty of 6.2. The experimental results were also used to perform extrapolation and performance estimations for a future theoretical deployable system with higher beam current and proton energy for improved reconstruction precision. In addition, a penetration study following the ANSI N42.46 standard was performed, demonstrating a maximum penetration thickness of 45 cm with a hypothetical beam current (14 μA) and scanning speed (4 cm/s). In conclusion, MMGR using compact superconducting cyclotron was demonstrated to be a low-dose and mobile method to screen commercial cargoes with high material specificity, provided a means of distinguishing benign materials from SNM to prevent the smuggling of SNM and improve overall global security.

Thesis Supervisor: Areg Danagoulian
Title: Associate Professor of Nuclear Science and Engineering

Thesis Reader: Richard C. Lanza
Title: Senior Research Scientist, Nuclear Science and Engineering

Research Committee: Zachary S. Hartwig
Title: John C. Hardwick Assistant Professor of Nuclear Science and Engineering

Acknowledgments

It's been both a privilege and a pleasure to be a part of the MIT NSE PhD program. To start, I would like to thank my supervisor Professor Areg Danagoulian for giving me the opportunity to participate in a challenging and exciting project. He provided the much needed understanding, guidance, and support through difficult times. My sincere gratitude to both Dr. Dick Lanza and Professor Zach Hartwig for being a part of my research committee and offering valuable insights on my PhD work. They helped me avoid all the rabbit holes, and pushed me to be a better researcher. I would also like to thank Dr. Brian Henderson for his mentorship, especially on explaining his previous work, which served as the foundation of this project.

The NSE also have numerous excellent staff members. I would like to thank Rachel Batista and Peter Brenton for their assistance with the MIT facility and helping me with all the administration related issues to ensure my work went as smooth as possible. Many thanks also to Heather Barry and Brandy Baker for always having their door opened for small chats when I was stressed and candies which I can steal.

I also owe special thanks to my peers at MIT. Bobby Nelson, thanks for working with me for a year and a half with CHARON. He was always willing to help when I have to run experiments. Dr. Jayson Vavrek, TD MacDonald, Ethan Klein, and Will Koch, thanks for being awesome office mates in the Fishbowl. In the Vault Lab, thank you to Dr. Leigh Ann Kesler for organizing the lab and her advice on how to deal with people. Most importantly, Steve Jepeal for being the other CHARON user and taking charge for managing the lab. Without him, the many problems we encountered would have hindered my research much more severely. He and the MIT Communication Lab also helped tremendously on my thesis editing.

Lastly, to my family. My cat Mittens for the fluff and helping with typing. She was always there for me (mostly for food). My Arcadia mother Dr. Christina Chow who always pushed me to be a better person and a master leech. Without her, I might not have even finished my undergraduate degree. And most of all, my wife Anita which followed me to Cambridge and supported me to pursue my PhD.

Contents

List of Figures

List of Tables

Chapter 1

Introduction

This chapter aims to provide a brief overview on the current situation with regards to cargo security, with a focus on nuclear smuggling, and a follow-up discussion on its shortcomings as well as potential solutions. It is essential to establish a strong understanding of the underlying issues in nuclear smuggling as that determines current policies on border security, specifically ones related to radioactive materials. A brief summary will follow regarding deployed cargo screening systems and conclude with details on the composition of containers passing through the U.S. based on previous studies by Henderson et al. [7] and O'Day et al. [5].

1.1 Issues with cargo security and nuclear smuggling

To formally address the question of whether nuclear smuggling constitutes a major concern, we first look at the International Atomic Energy Agency (IAEA) Incident and Trafficking Database (ITDB). The ITDB program currently consists of 136 participating countries in a joint effort to keep a record of all incidents related to radioactive materials [9]. Since its establishment in 1995, 3235 incidents had been registered. Among this number, only 278 incidents were either confirmed or determined likely to be related with trafficking or malicious activities, with some involving Special Nuclear Material (SNM) [9]. Defined by Title I of the Atomic Energy Act of 1954, SNMs are either plutonium, ^{233}U, or uranium enriched isotopes ^{233}U or ^{235}U,

but does not include source material [10]. It also includes any other material that the NRC determines to be special nuclear material. Between 1992 and 2001, including unconfirmed reports, 18 different incidents have involved 41 kg of SNM with over 99% of them being highly enriched uranium (HEU) [11, 12]. HEU is defined as being more than 20% enriched. Furthermore, 9.25 kg of them were over 87% enriched. Below is a condensed list of selective incidents [11, 12, 13]:

- 1992 - First known case involving the theft of weapons-grade uranium. A scientist from Podolsk, Russia stole a total of 1.5 kg of 90% enriched ^{235}U from the Luch Scientific Production Association. Each time, he took 50 g of uranium and stored them in a jar over the course of five months. The Russian police arrested him due to an unrelated investigation.

- Dec 1998 - The Russian Federal Security reported they prevented the theft of 18.5 kg of HEU from an unspecified nuclear facility in Chelyabinsk Oblast, Russia. The Russian Ministry of Atomic Energy confirmed the involvement of HEU but did not disclose information regarding the exact enrichment.

- May 2000 - According to a report prepared by the Russian Nuclear Regulation Agency Gosatomnadzo, a resident of Elektrostal was detained during an attempt to sell 3.7 kg of 21% enriched ^{235}U.

- 2008 - Two Ukrainians were arrested with possession of 4.1 million USD worth of cesium and uranium, which they planned to sell to a criminal organization.

While the aforementioned incidents do indicate that smuggling and trafficking of SNM is an existing problem, they were also mostly conducted by amateurs. However, a handful of cases did involve professional organizations. One such example is the arrest of the captain of a ship in Batumi in 2001 with possession of 1.7 kg low enriched uranium, which subsequently led to the investigation of multiple related smuggling in the area [12]. Since maritime and land transportation are the most common means for nuclear smuggling, sufficient security is of utmost importance to prevent future nuclear trafficking.

In December 2018, the Countering Weapons of Mass Destruction (CWMD) Office was established to counter and prevent any attempts to use weapons of mass destruction (WMD) against the United States and its interests [14]. Reports have also suggested an increase in black market activities for nuclear materials since September 11, 2001 [11, 15]. These numbers suggested an increase in demands and willingness of criminals to use WMD for illicit activities. As more scientists and researchers became involved in nuclear security, they began to estimate the potential impact of a nuclear terrorist attack. From a study in 2018, Arguello and Buis [16] estimated a detonation of a small 1-kiloton atomic bomb in any large capital city would result in thousands of deaths and injuries, escalate social fragmentation, and increase global poverty as a result of the economic impacts [16]. While an atomic bomb explosion can cost hundreds of billions of dollars, it is by no means the only potential method for a terrorist carrying out a nuclear attack [16]. Other radioactive materials can also be utilized to produce a radiological dispersal device (RDD), also known as a "dirty bomb," to contaminate an area around the blast zone with high levels of radiation [17]. Although RDD are much less damaging in terms of explosive energy, there could be significant socioeconomic damage from the forced evacuation of residents, disruption in trades, and the costs of radiological decontamination, along with the number of resulting injuries related to the explosion or exposure to radiation [18, 19, 17].

Radiactive materials for a RDD may also be easier to obtain and more readily available than we anticipated. In 2018, the Ukrainian security services arrested six individuals attempting to sell police an unknown quantity of ^{226}Ra [20]. Those individuals were believed to belong to an international radioactive materials smuggling ring. Furthermore, there were also indications of many abandoned radiation sources and materials in Ukraine. On October 2016, the supreme council of Ukraine, the Verkhovna Rada, passed a law allowing for voluntary surrender of radioactive materials without criminal liability. There were increasing cases of illegal possession and disposal of such materials because poor performing and bankrupted companies would save on disposal fee and taxes [21]. With the aid of the U.S. and other countries, 14755 spent radiation sources were collected between 2009 to 2015, with a total ac-

tivity of 1.27 PBq (34.3 kCi). Many of them were left abandoned and unguarded in landfills [21]. In conclusion, nuclear smuggling is indeed an existing issue and there needs to be safety measures in place to prevent such illicit activities.

1.2 Border security and deployed screening systems in the U.S. ports of entry

Currently, most cargo containers undergo two screening processes prior to formal entry into the U.S: the first prescreening occurs at the outbound ports and the second at the different U.S. ports of entry. Within months following the terrorist attacks on September 11, 2001, the U.S. Customs Services established the Container Security Initiative (CSI), aiming to protect the U.S. border against potential smuggling of nuclear weapons by the terrorist [22]. The CSI have three main goals: 1) Identify high-risk containers based on advance information and strategic intelligence. 2) Prescreen and evaluate cargo container at the port of departure. 3) Using technology such as X-ray machine and radiation detection systems to ensure rapid prescreening [22]. Currently, the CSI prescreens 80% of all maritime containers at 58 ports located in Africa, Asia, Europe, Latin and Central America, the Middle East, and North America [22].

Within the U.S. borders, the U.S. Customs and Border Protection (CBP) provides the required safeguard with different technologies based on different operations. Large-Scale (LS) Non-Intrusive Inspection (NII) systems are deployed to image passenger vehicles and cargo conveyance mainly for the presence of concealed contraband such as money, narcotics, and weapons [23]. As of July 2017, 301 LS-NII systems are deployed at different ports of entry out of the 328 ports. During the 2016 fiscal year, more than 6.45 million screens were conducted, leading to over 2600 seizures and over 359000 pounds of seized narcotics [24]. According to Kauchak et al. [25], one common inspection system is the Mobile Vehicle and Cargo Inspection System (Mobile VACIS), which utilizes a 1.0 Ci ^{137}Cs or 0.75 Ci ^{60}Co for gamma imaging [25]. How-

ever, the major draw back is that the penetration of the low energy gamma is small, approximately 10 to 15 cm of steel [26]. Furthermore, the nominal resolution is only 12.7 mm at 8 km/h scanning speed [26]. Although there are more advanced systems utilizing dual-energy X-ray to image containers with improved material discrimination ability and penetration (30 cm of steel at 8km/h), they come with disadvantages that will be discussed in a later section [27, 28]. In case of stowaways, the dose to a single person in the cargo by a scan from the system mentioned above at a scan speed of 3.2 km/h is 1.028 mrem, which is approximately equivalent to the average daily radiation exposure in the U.S. from natural sources of radiation [28]. It is also important to know that for all the LS-NII systems mentioned above, the 2 mR/h dose access control boundary takes up a considerable amount of valuable space in the port as it is at least 8 m in size [26, 27, 28].

Other than LS-NII systems, CBP also worked with the Domestic Nuclear Detection Office (DNDO) with the mission to "prevent nuclear terrorism by continuously improving capabilities to deter, detect, respond to, and attribute attacks, in coordination with domestic and international partners" [29]. This provided the main layer of defence against smuggled or illicit radiological materials through passive and non-intrusive means without the necessity of physically unloading the inspected cargo. Together, CBP and DNDO deployed nuclear detection systems such as large Radiation Portal Monitors (RPM), Radiation Isotope Identification Devices (RIID), and Personal Radiation Detectors (PRD) [24]. As of June 2017, a fleet of 1276 RPMs, 3316 RIIDs, and 34387 PRDs operational systems have been deployed nationwide [24].

Within these deployed nuclear detection systems, the most important ones are the larger and stationary RPMs, which screen for nuclear materials in all truck cargoes, all vehicles arriving from Canada and Mexico, and nearly all maritime cargo containers [17]. Nearly all RPMs are designed and manufactured by Leidos Holdings, Inc. and Ludlum measurements, Inc. They are similar in design, with five large plastic scintillator totalling a volume of 2.26 square meters [30]. However, there are two major drawbacks to these systems. First, those detectors can only identify radiation signatures passively, meaning a knowledgeable smuggler could theoretically

bypass the system by shielding radiation signals to prevent them from triggering the RPMs. Another drawback to the large plastic scintillator is that they do not provide information about the gamma energy in the detection signals. As such, they cannot distinguish between naturally occurring radioactive materials (NORM) and SNM. Over the history of deployment, almost 2% of all cargo screened triggered hundreds of thousands of false alarms by the RPMs [17]. Although it is under the typical 3% alarm rate sought by cargo security authority, it nevertheless resulted in officers having to physically examined those cargoes using RIID and spent thousands of hours of inspection time, thus disrupting the flow of containers in ports.

1.3 Composition of containers entering the U.S.

This thesis will discuss and develop a proof-of-concept radiography system as well as reconstruction techniques. Since this system targets cargo screening, it is important to have general knowledge about the content and amount of cargo containers in circulation. In 2015 alone, the U.S. traded 31.5 millions TEU of goods in both export and import [31]. TEU (twenty-foot equivalent unit) is a measure of volume in units of twenty-foot long containers with a maximum total load of 24 metric tons. In terms of monetary values, the U.S. traded a total of 468.8 billion U.S. dollars worth of international trading of goods and services in June of 2019. [32]. A total of more than 300 official ports of entry and 600 crossings into the U.S. are in place to handle such high amount of tradings. In a study by Lawrence Livermore National Laboratory (LLNL), cargo manifests of U.S. imports through 44 North American ports over 14 randomly selected days in 2005 were analyzed [8]. 496990 records were collected from 149 different countries and the tabulated percentages of imported commodities by categories are shown in Table 1.1. From the data, the first five most common categories made up over 61% of all the imports. Within all the goods, 12% were stone, ceramics, mineral products, 28% of them were metal based and almost 60% of them were organic. Metals have a medium to high atomic number (Z) while organic materials and ceramics have a low Z. More discussion on atomic number will be

discussed in Sec. 6.2.

Table 1.2 also lists other materials of interest such as naturally occurring ra-

Product	TEU [% total]
Furnitures, Toys, Misc. Manufacturing Articles	20.18
Machinery and mechanical appliances	15.48
Textiles and Textiles articles	10.75
Base metals and articles thereof	7.11
Plastic and rubber	7.00
Articles of Stone, plaster, cement, asbestos	4.00
Footwear, headgear	3.98
Wood and Wood products	3.64
Chemical products	3.12
General merchandise	3.09
Vegetable Products	2.66
Wood pulp products	2.47
Hides and skins	2.24
Animals and animal products	1.60
Instruments measuring-musical	1.41
Mineral products	0.63
Animal or vegetable fats	0.15
Works of art	0.07
Pearls, precious and semi-precious stones, metals	0.05
Arms and ammunition	0.03

Table 1.1: Distribution of U.S. imports organized by commodity categories and ordered by %TEU based on 14 days of cargo manifests from 44 North American ports [8].

dioactive materials (NORM) as well as high Z materials. SNM have a high Z as well, so a system set to screen cargoes for SNM using a Z threshold may set off false alarms. However, NORM cargoes also raise a large concern since there are many more NORM than high Z cargoes. NORM sources contain ^{40}K, ^{232}Th, and ^{226}Ra. In particular, these can be found in bananas, ceramics, cut stones, fertilizer, salts, and rocks. In a similar fashion, NORM in imported cargoes may also trigger existing passive detection systems, thus causing false alarms and interference. The table lists the total volume in TEU, total mass, number of days with records of the goods and the extrapolated number of day per years with such records.

Product	weight [ton]	TEU [% total]	#days/year
Bananas	32348	0.42	365
Ceramics	264056	2.31	364
Cut Stones	84730	0.58	364
Fertilizer (K)	1697	0.01	52
Rock or Salt	73989	0.49	364
Rad Sources	30	3.30e-6	52
U	52.48	6.02e-6	26
U metal	1.15	1.24e-6	26
UF6	153	2.80e-5	130
Pb articles	323	3.00e-3	26
W ores	280	2.4e-3	312
W articles	123.4	7.0e-4	52

Table 1.2: Potential materials of interference and cargoes of interest, including NORM and materials emitting natural radiation that may cause false alarms (top section with five products), medical and industrial sources and objects related to the nuclear fuel cycle (middle section with four entries), and high Z materials that are difficult to image and close in Z with SNM (bottom section).
[8]

Other than content categories and Z, it is essential to know the areal density of the cargo contents for the purposes of setting alarm thresholds and gamma penetration study. In a study by Henderson [1], a dataset of 122,500 cargo container scanning images acquired from a 6 MeV gamma radiation system entering a European port by rail was analyzed and the distributions for the effective areal density by pixel of the cargo are shown in Fig. 1-1. In order to convert cm-steel equivalent to areal density, the cm-steel equivalent should be multiplied by the standard density of steel (approximately 8 g/cm^3). One major implication is that almost 25% of 20 foot containers and 40% of 40 foot containers are empty. Another implication is that almost 40% of cargoes are above the 15 cm-steel equivalent which is the quoted penetrations of the Mobile VACIS system (10 to 15 cm-steel equivalent) as mentioned in Sec. 1.3. Although there are more advanced systems utilizing single energy X-ray to image containers with higher penetration (30 cm of steel at 8km/h), it dose not provide Z discrimination [28].

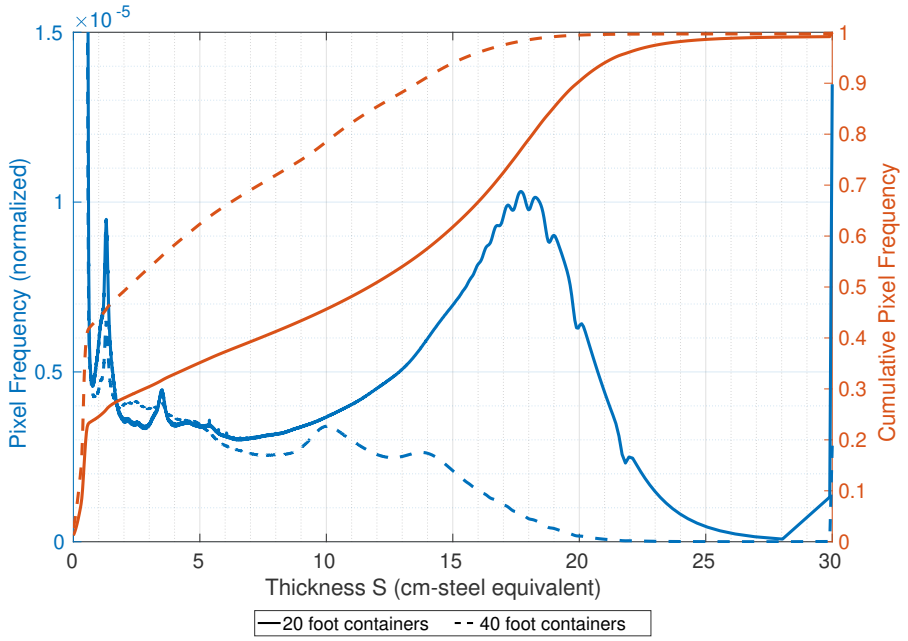

Figure 1-1: Distributions of the effective areal density (in units of cm-steel equivalent) by pixels of cargo images, separated by 20 and 40 foot containers with corresponding cumulative distribution. The peak corresponding to pixels of less than 0.5 cm-steel equivalent (no material present between container walls) is truncated. This image also omitted the pixels of container roofs. Reprinted with permission from Henderson [1].

Chapter 2

Common SNM Detection Techniques

This chapter will introduce readers to passive and active interrogations in addition to other common techniques. Simple radiography will also be discussed as a conceptual introduction on how one should use gamma transmission measurements for SNM detection. Each technique will also be scrutinized for its shortcomings and limitations. A section examining the requirements of a system for SNM detection will conclude this chapter. It is important to note that this PhD thesis is an extension of previous works conducted by O'Day et al. [5] [6] and Henderson et al. [7] to further improve the multiple monoenergetic gamma radiography techniques. The chapter will concluded with the results of using a compact superconducting cyclotron to generate the needed gammas through low energy nuclear reactions from a compact superconducting cyclotron for MMGR, which would potentially lead to a more deployable mobile system.

2.1 Passive interrogation

2.1.1 Basic principle

Passive interrogation is not well named since it does not involve interrogation of the inspected object using probing radiation. A more apt term would be the passive detection of radiation signatures emanating naturally from materials such

as SNM. These signatures of emitted gamma-rays, neutrons, or charged particles from decays of nuclei would then penetrate and attenuated by surrounding shielding materials before being detected by detectors. This process does not involve using an accelerator, making it one of the simplest and relatively inexpensive detection methods. Many passive detection systems currently utilize this for deployment, such as large RPM, RIID, and PRD mentioned in Sec. 1.2. Most deployed RPM are equipped with large volumes of cheap plastic scintillator such as polyvinyltoluene (PVT) to measure gamma signatures. Some systems are also fitted with an ^{3}He or ^{10}B detector to measure neutron signatures due to the neutron's higher penetration capability. Additionally, there is smaller natural neutron background compared to gammas [33, 34]. However, systems fitted with ^{3}He or ^{10}B detectors are more costly due to the potential limited supply of ^{3}He [33, 34].

2.1.2 Limitations

To fully understand the limitations of passive interrogation, the radiation signatures from SNMs need to first be discussed and a metric defined to qualify the detection signal. Due to the weak penetration abilities of alpha and beta particles, this section will focus on gamma and neutron only.

Gamma signatures from SNMs originated from radioactive decay by isotopes along the decay chain of SNMs. Common high intensity gammas are at 767 and 1,001 keV from the decay of ^{234m}Pa (^{238}U decay chain) and 662 and 772 keV from the decay of ^{241}Am (^{241}Pu decay chain)) [35]. For ^{235}U, the gammas are much lower in energy at 186 keV and can be easily shielded by the surrounding material. In Fetter et al. [36], a hypothetical weapon with a hollow sphere of 12 kg (7 cm radius) weapons-grade uranium (WgU) or 4 kg of weapons-grade plutonium WgPu (5 cm radius), along with 2 cm thick Be reflector, 3cm W tamper, 10 cm high explosive, and 1 cm Al case were used as a model to calculate the gamma and neutron emission rates at the surface. As for gammas, the emission rates of 1001 keV gammas from an uranium device and 662 keV gammas from a plutonium device at the surface of the sphere are 30 and 600 per second respectively [36]. This number is low due to the self-attenuation of the SNMs

and the attenuation of gammas by the tamper material, especially high Z materials such as the W tamper. Additional shielding could easily reduce this number down to the background level. On the other hand, neutrons not only have relatively higher penetration capabilities but also a lower natural background, thus yielding higher detection signals. In the same hypothetical weapon discussed above, the emission rate of neutron at the surface of the WgU and WgPu model are 30 and 400,000 per second respectively. It is important to note that the neutron flux from ^{235}U is extremely low due to its low spontaneous fission rate, a main contributor of natural neutron production in SNMs. This neutron flux from ^{235}U is orders of magnitudes lower than ^{238}U, ^{238}Pu, and ^{240}Pu. Although neutrons are more penetrative in general, they can easily be shielded with water or plastic.

The next task is to quantify the strength of the passive signals. A common metric for quantifying the signal is to determine the signal to background ratio between two measurements (one long overall background measurement and one passive interrogation measurement), given in the following formula [6]:

$$\frac{c_s}{\sqrt{\sigma^2_{c_s+c_b} + \sigma^2_{c_b}}} \tag{2.1}$$

where $c_s + c_b$ represents the total counts from the passive interrogation measurement, c_b represents the background counts scaled to the same measurement time. c_b could be found precisely from a long background measurement prior to the passive interrogation measurement and scaled appropriately. c_s is the net counts of the radiation signature which is the difference in total counts between the two measurements of the same length $(c_s+c_b)-c_b$, $\sigma^2_{c_s+c_b} = c_s+c_b$, and $\sigma^2_{c_b} = c_b$ assuming the uncertainty of each measurement is just the square root of the counts and there is no correlation between the background and the radiation signature.

For 1001 keV gamma from a 12 kg WgU weapon, the number of 1001 keV gammas measured without taking background into account would be reduced to approximately 0.035 cpm. This count rate calculated takes into account the solid angle of detection at 2 m away from the surface of the device, the peak efficiency of a 1.5"×1.5" $LaBr_3$

at approximately 25%, and the attenuation of gammas by 2 mm of steel which represents the wall thickness of a cargo [37, 38]. With the background gamma rate of 33 cpm at the Vault Laboratory in the basement of building NW13 for the same 1001 keV energy window, the signal to background ratio is only 0.0043 if a one minute measurement is taken. Hence, this small signal is not practical for cargo screening if only one small volume detector is used. Similarly, the background neutron flux at sea level in New York is 14 neutrons/cm^2/hour which is over 20 times higher than the neutron emission from the modelled 12 kg WgU weapon at 2 m away [39]. As such, SNMs are difficult to detect with passive detection methods, especially WgU. If the weapon design contains depleted uranium tamper or is a Pu-based device, the gamma and neutron emission rate will be much higher and possible to be detected by passive interrogation. In reality, most deployed RPMs utilized large plastic scintillator totalling a volume of 2.26 square meters in order to detect such small signals [30]. However, passive detection of radioactive materials remains challenging if even a small amount of shielding is involved.

For the cases which involve NORM, passive detection of SNMs becomes especially challenging. Richard T. Kouzes and Dowyer [40] mentioned "discrimination of sources of concern such as SNMs from NORM cannot be accomplished with a simple gross-count approach" [40]. To avoid false alarms caused by NORM, a more sophisticated passive detection method has to be developed to better differentiate the signals between NORM and SNMs. One approach to discriminate SNMs from NORM is by separating the transmitted gamma spectrum into three energy windows along with an energy-window ratio algorithm for passive detection. This technique provides excellent sensitivity to modest amounts of SNM while allowing NORM discrimination [40]. However, passive detection remains efficient to only SNMs with no intentional shielding. A more logical approach suggested by Kouzes [41] is to use passive detection as the primary screening method while radiography is used for secondary screening and targeted containers [41].

2.2 Active interrogation and radiography

2.2.1 Basic principle

Due to the poor detection and characterization capability of passive interrogation on SNMs, research studies have shifted focus towards development of active interrogation and radiography techniques with great potential for detection of small quantities of SNMs and explosives [42]. Active interrogation is defined as the directing of ionizing radiations into the inspected object and measuring secondary radiations from induced nuclear reactions between the probing radiation and the inspected object for characterization and information gathering. As such, active interrogation excludes radiography in which ionizing radiations are directed to and subsequently attenuated by the inspected object prior to detection for material discrimination. Typical ionizing radiations used for active interrogations and radiographies include gamma, X-ray,and neutrons. Although systems utilizing other particles such as muons exist, this thesis will not discuss these in details as they are mostly proof-of-concepts systems.

The three dominant gamma and X-ray sources are: 1) accelerator-based source accelerating electrons to a few MeV into metal targets, creating X-rays via bremsstrahlung radiation. 2) accelerator-based source accelerating protons or heavy ions to high-energy and creating gammas through different $(p, p'\gamma)$ reactions. 3) radioisotope-based source utilizing gammas from the decay of radioactive isotopes such as ^{137}Cs and ^{60}Co.

The most common method of generating neutrons is through fusion of light nuclei such as $\mathrm{D(d,n)^3He}$ (deuteron-deuteron [DD]) and $\mathrm{D(T,n)^4He}$ (deuteron-tritium [DT]), generating neutrons at 2.5 and 14.1 MeV respectively. Depending on the size of the generator, the neutron flux typically lies in a range of 10^6 to 10^{10} per second [43]. Another method to generate neutrons is by using photon-neutron (γ,n) sources to generate gamma by (γ,n) reaction with beryllium or deuterium. There are also accelerator-based systems that utilize proton-induced reactions such as $\mathrm{^{11}B(d,n\gamma)^{12}C}$, generating neutrons at multiple energies [3]. The last category of neutron sources are based on radioisotopes such as spontaneous fission of ^{252}Cf or alpha emitter (such as

^{241}Am) with ^{9}Be to produce neutrons through $^{9}\mathrm{Be}(\alpha, \mathrm{n})^{12}\mathrm{C}$ reactions.

2.2.2 Prompt and delayed signal detection from induced fission

The active interrogation technique of measuring signatures from induced fission will be discussed in this section. Since fission is a unique interaction with SNMs and actinides, the signatures from this process can be used to identify such material. Two types of induced fission are relevant for active interrogation. One is neutron-induced fission while the other is photofission induced by gammas. Photofission is a threshold reaction, requiring gammas to be above a certain threshold energy before it can occur (eg. ^{235}U and ^{238}U photofission have an experimental threshold of 5.31 and 5.08 MeV respectively) [44]. There are several advantages of using induced fission for active interrogation. First, the cross section for both neutron and photon induced fission are relatively high. The fission cross section are in the $\mathcal{O}(b)$ and $\mathcal{O}(0.1b)$ respectively for source particles in the MeV range [43]. Furthermore, multiple signatures from the fission reactions can be utilized for screening purposes.

A fission reaction produces two radioactive fission products at Z of approximately 95 and 135 that subsequently decay through beta decay or neutron emission [43]. Signatures from fission are typically separated into four categories: prompt fission gammas, prompt fission neutrons, delayed fission gammas, and delayed fission neutrons. These signatures differ in terms of yield, energy and temporal profile. For example, a signal is considered prompt if it is emitted within 10 ns following fission. Verbinski et al. [45] reported that each neutron-induced fission of ^{235}U yielded 6.6 prompt gamma rays, which averaged at 0.970 MeV. As for prompt neutron from neutron-induced fission of ^{235}U, the yield averaged around 2.4 per fission with approximately 20% of them above 3 MeV with the neutron spectrum following the Watt distribution. Photofission yields were similar to neutron-induced fission in terms of both prompt and delayed signal [46]. For delayed signatures, the literature usually distinguished the signals into six different groups, depending on the half life of the isotopes. Fission

fragments emitting delayed neutrons are known as neutron precursors with a half-life between 0.074 to 58.2 s and a low yield of only 0.045 neutron per neutron induced fission on ^{238}U [47]. Following photofission, the delayed neutron has even lower yield in general. According to Runkle et al. [43], delayed neutron yield following photofission from a bremsstrahlung source with an endpoint of 8 MeV was approximately 0.0090 per fission. There were also delayed gammas being emitted from radioactive decay of these fission fragments. For more details discussing neutron and gamma yields from induced fission, see Gozani et al. [48] and Runkle et al. [43]. With the use of a different kind of accelerator, such as pulsed LINAC, experimental systems were made to conduct experiments to detect and measure these prompt and delayed signatures [43, 48]. However, due to challenges such as active background and interference of source radiation, and most importantly, the cost and operational complexity of such systems, almost none of the actively deployed cargo scanning systems in the U.S. utilize induced fission.

2.2.3 Backward scattered photon detection

Another commercially deployed technique for cargo screening is backward scattering photon detection. When photons irradiate an object, some of them may scatter off at various angles relative to the beam. This occurs primarily through two processes. Compton scattering is one mechanism in which the photon is scattered off the electrons of an atom. During Compton scattering, part of the gamma energy gets transferred to the electron as recoil energy. The gamma itself then scatters in different directions, with a small chance to backward scatter for high energy gamma. The main process where photons are "scattered" backward is through pair production. When a high energy gamma interacts with material via pair production, a high energy electron-positron pair is produced where they will subsequently create new X-rays by bremsstahlung radiations. Because bremsstahlung has a strong dependency on atomic number ($\sigma_{brem} \propto Z^2$) and pair production also has a Z dependency as shown in Sec. 2.2.6, there is a strong correlation between the number of off-axis scattered photons and the interrogated materials. Companies such as Passport Systems,

Inc. developed systems utilizing a similar principle, called EZ-3D^{TM} and utilized it in conjunction with other interrogation techniques for material discrimination [49]. However, most systems implementing backscattered photon detection, such as those made by American Science & Engineering and Rapiscan Systems, are large in size. Furthermore, their main purpose of these systems are to detect the presence and positions of organic components in the inspected objects instead of an accurate Z discrimination [50].

2.2.4 Gamma radiography

The focus of the technique developed, discussed, and implemented in this PhD thesis is based on gamma radiography. A simple transmission gamma radiography relies on measuring the attenuated flux of the interrogating particles with respect to the incident flux, and using that attenuation information to possibly infer the areal density and the material type of the inspected object at the scanned position. This makes radiography a common imaging technique, allowing for visualization of the internal compositions of the cargo without the need for a manual inspection. The attenuation of gamma rays in materials is given by the following equations:

$$Attenuation = \frac{I}{I_0} = e^{-\mu x} \tag{2.2}$$

$$\mu = \mu_{pe} + \mu_{cs} + \mu_{pp} \tag{2.3}$$

where I is the transmitted gamma intensity, I_0 is the source intensity, x is the areal density, and μ is the total mass attenuation coefficient from photoelectric effect, Compton scattering, and pair production as indicated by Eq. 2.3. The attenuation image of the object can be constructed by taking transmission measurements across it. SNMs can strongly attenuate gamma rays (with high μ) as they are materials with high atomic number (Z). As such, simple gamma radiography can be used to identify SNMs if a significant quantity of them get scanned. However, this simple radiography technique has limitations as indicated in Eq. 2.2, where attenuation depends on μx, in which small amounts of SNM (small x, large μ) and large amounts of weak attenuating

benign materials (large x, small μ) will lead to the same attenuation. In this case, simple radiography will not be able to distinguish between the two. Therefore, this makes setting an alarm threshold for simple transmission gamma radiography to indicate potential SNMs difficult.

2.2.5 Neutron radiography

Aside from using single energy gammas for radiography, neutrons could also be used for radiography. Previous work by Rahon et al. [3] have demonstrated the use of neutrons generated from $^{11}\mathrm{B}(\mathrm{d},\mathrm{n}\gamma)^{12}\mathrm{C}$ reaction to perform neutron radiography on various objects. In a similar principle to gamma radiography, transmitted neutron spectral analysis is used to image the inspected material, especially to quantify the hydrogenous content. The basic idea is to exploit the large differences of neutron scattering cross section at different neutron energies between hydrogen and high Z material. As an example, $^{1}\mathrm{H}$ has a total neutron attenuation cross section of 4.25 and 0.94 b at 1 and 10 MeV respectively, while $^{56}\mathrm{Fe}$ has a total neutron attenuation cross section of 2.28 and 3.03 b at 1 and 10 MeV respectively [51]. In the experiment conducted by Rahon and Danagoulian [4] , this technique was able to quantify up to 30 g/cm^2 of high density polyethylene, even with the mix of metallic materials [4]. Although neutron radiography is efficient and effective at quantifying hydrogenous content, it cannot accurately discriminate medium to high Z materials. As mentioned in Blackburn et al. [52], it is possible to use fast neutron resonance radiography to reconstruct elemental maps of hydrogen, carbon, nitrogen, oxygen, and silicon of the inspected objects [52]. However, there is concern related to induced neutron dose when using neutrons as the probing particles for active interrogation or radiography.

2.2.6 Dual-energy bremsstrahlung radiography

One method to simultaneously determine the effective atomic number (Z_{eff}) value and areal density (x) of the cargo material is to exploit the Z dependence of μ at different energy ranges and to take transmission measurements at two or more en-

ergies [5, 6, 7]. In the MeV range, the major gamma interaction mechanisms are Compton scattering (CS) and pair production (PP) and their mass attenuation coefficients are represented by [7, 53]:

$$\mu_{cs} = ZN_A\sigma_c(E, Z)/A \tag{2.4}$$

$$\mu_{pp} = N_A\sigma_{pp}(E, Z)/A \tag{2.5}$$

$$\sigma_c \propto 1/E \tag{2.6}$$

$$\sigma_{pp} \propto Z^2 f(E) \tag{2.7}$$

where μ_{cs} and μ_{pp} are the mass attenuation coefficient of CS and PP with the corresponding interaction cross section σ_{cs} and σ_{pp}, N_A is the Avogadro number, A is the mass number of the material, m_e is the rest mass of electron, and E is the energy of the gamma [53]. As mentioned in Runkle et al. [43] and discussed in [7], the $f(E)$ in the pair production cross section estimation is a function of energy with negligible dependence on Z [7, 53]. This negligible dependence on Z stems from the Bohr correction and is explained in details in Leo et al. [53]. From the equations above and the characteristic that the ratio of atomic number-to-mass (Z/A) is approximately 0.4 to 0.5 for most stable isotopes, the mass attenuation coefficient of Compton scattering does not heavily depend on the Z of the materials, only areal density (x) and energy of the gamma. Similarly, the mass attenuation coefficient of pair production is linearly dependent on the Z of the materials and can be exploited to identify the material type (Z_{eff}). Fig. 2-1 demonstrates the behavior of mass attenuation coefficient for different materials as a function of energy.

Traditional dual-energy bremsstrahlung radiography systems use electron beam switching between two energies and a metal target to generate gammas for dual-energy radiography. Taking energy-integrated transmission measurements at the two energies allows one to perform material discrimination [54, 55]. Coincidentally, the only pertinent information required to determine the Z and areal density of the object in transmission radiography stems from the difference between the two energy spectra at high energies. As a result, the similar low energy bremsstrahlung continuum

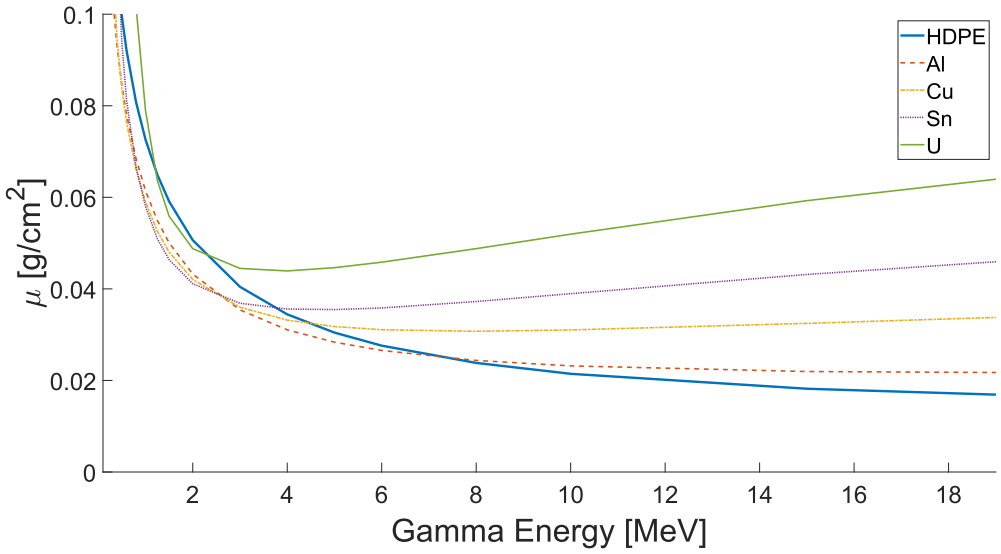

Figure 2-1: Mass attenuation coefficient of various materials with different Z as a function of energy. Figure is reproduced using data from the XCOM: Photon Cross Sections Database [2].

between the two energy spectra only lead to unnecessary dose without contributing to the meaningful signal. In a study by Jones et al. [56], the measured dose rate of a 10 MeV end-point bremsstrahlung source at a 2 m stand-off distance is over 10 rem/min/μA, a significantly high radiation dose rate which will be harmful after prolonged exposure. Although hardening of bremsstrahlung beam could be performed by filtering out X-rays below a few hundred keV to reduce induced dose during radiography, there is still significant similarity between two bremsstrahlung continuum with different energy end-points in the higher energy region. Common X-ray filtering materials include aluminum, copper, tin, and lead, which can be used in combination to attenuate low energy gammas. Since photoelectric effects is the dominating interaction by photons below a few hundred keV and the attenuation coefficient is higher at low energy as shown in Fig. 2-1, low energy gammas can be filtered out, producing a "harder" bremsstrahlung spectrum [57]. Another disadvantage of the bremsstrahlung-based system is most existing systems are designed to seek out organic materials and explosives but not SNMs. In the product overview of the Eagle P60 with dual energy X-ray of 4 and 6 MeV end-points, it states that their sys-

tem "enables low atomic number (low density) contraband, such as explosives, to be distinguished from high atomic number (high density) materials such as steel" [58].

2.3 Objectives and proposed system

Ideally, a screening system will have the ability to distinguish all kinds of materials (organic, inorganic, heavy metal, weapons, drugs, or SNMs) in any quantities without false alarms. It should also be cheap to manufacture, maintain, and operate. Furthermore, it should have fast scanning time and high resolution in addition to a short setup time and being simple to operate. Low induced dosage is also essential in case of stowaways.

In reality, there are restrictions to what a system can accomplish. They may be limited by the accelerator, machines, or detectors. This research proposes a multiple monoenergetic gamma radiography system utilizing a 12 MeV compact superconducting cyclotron and builds on the MMGR techniques with the goal to achieve the following:

- A compact radiography system that could be transported and deployed easily.
- A system with a short setup time in $\mathcal{O}(hours)$.
- A system that could produce radiographic image with resolution in $\mathcal{O}(cm)$.
- A system with the ability to discriminate between low, medium, and high Z materials (i.e. SNM) without physically opening the inspected cargoes.
- A system that is easy to operate and maintain with reasonable cost and is accessible for use at any given time.
- The scanning time for a cargo to be in $\mathcal{O}(mins)$.

Chapter 3

Multiple Monoenergetic Gamma Radiography (MMGR)

Here, a novel system will be presented for low-dose gamma radiography using multiple monoenergetic gamma rays generated by low energy nuclear reactions. The goal of Multiple Monoenergetic Gamma Radiography (MMGR) was to simultaneously predict the effective atomic number (Z_{eff})[1] and areal density (x) of the interrogated materials. MMGR has the advantage of delivering less dose to cargo while performing similar or superior Z discrimination as opposed to the dual-energy bremsstrahlung radiography system mentioned in Sec. 2.2.6. A comparative analysis of dose between the two methods will be discussed in Sec. 3.3. Potential reactions to generate monoenergetic gammas will also be discussed along with other criteria for what constitutes as a good candidate reaction. In addition, reactions used in previous MMGR experiments will be discussed, as well as the limitations encountered in this past system.

3.1 Multiple Monoenergetic Gamma Radiography

This section will examine a simple model of MMGR using both a low energy (E_0) gamma attenuated primarily by Compton scattering and a higher energy (E_1)

[1]For consistency, Z_{eff} will represent the reconstructed effective atomic number and Z as the atomic number.

gamma attenuated primarily by pair production. Further discussion on this simple model can be found in Henderson et al. [7]. With the exponential gamma attenuation equation and gamma transmission at two energies (E_0 and E_1), one could compute the following [7]:

$$R = \frac{\mu_1 x}{\mu_0 x} = \frac{\mu_1}{\mu_0} = \frac{\log(I(E_1)/I_0(E_1))}{\log(I(E_0)/I_0(E_0))} \tag{3.1}$$

where μ_0 and μ_1 are the mass attenuation coefficients of the material at E_0 and E_1. $I_0(E)$ and $I(E)$ are the unattenuated and attenuated counts of gammas at energy E. Assuming gammas at E_0 are completely dominated by Compton scattering and gammas at E_1 are dominated by pair production, and Eq. 2.3, 2.4, 2.5, 2.6, 2.7, Eq. 3.1 becomes:

$$R = \frac{N_A Z^2 f(E_1)/A \cdot \text{const}_1}{Z N_A / E_0 A \cdot \text{const}_2} = C Z E_0 f(E_1) \tag{3.2}$$

where C is the constant equal $\text{const}_1/\text{const}_2$ from the mass coefficient equation. With all these assumptions and experimental measurements of I and I_0 at energies E_0 and E_1, this simple model can be used to directly determine Z_{eff} and x of the interrogated material.

This is by no means the most accurate method to estimate the Z_{eff} and areal density of the inspected object, due to the assumption that the gammas are completely dominated by Compton scattering or pair production. In the previous experiments conducted by O'Day et al. [5] and Henderson et al. [7], MMGR were performed using 4.4 MeV and 15.1 MeV gammas from the ^{11}B(d,nγ)^{12}C reaction. In reality, 4.44 MeV gammas are dominated by pair production instead of Compton scattering for materials with $Z >\approx 70$. However, this simple model captures the idea of using ratios of attenuation ratios for Z_{eff}, which were used for the reconstruction method developed in this thesis for MMGR.

A more accurate method for dual energy or multiple energy radiography is by computing an attenuation table across different Z and different areal densities at each of those energies and comparing the experimental attenuations with the theoretical attenuations. The Z_{eff} and predicted areal density will be the ones that result in the best match between the experimental and theoretical attenuations. For the specific

reconstruction method used for this thesis experiment, please see Sec. 6.1.

3.2 Gamma production from nuclear reaction

The most critical component of MMGR is embedded in the name: the generation of multiple monoenergetic gammas. In order for the new MMGR system to work, multiple monoenergetic gammas in the range of a few (∼3-15) MeV are required to exploit the Z dependence of gamma attenuation at different energies. To generate such gammas, low energy nuclear reactions are the primary mechanisms. Since the newly proposed system accelerate protons to approximately 12 MeV, a search was conducted in existing literature for nuclear reactions that can be utilized to generate multiple monoenergetic gammas. There are a few criteria for selecting the optimal nuclear reactions for this technique. For one, gammas at multiple energies need to be generated from nuclear reactions with 12 MeV source protons in order to perform multiple energy gamma radiography. Additionally, the gamma yield will need to be high in order to reduce the scanning time per scan. To maximize the gamma yields, the target must be relatively dense (excluding the use of gases) and have a high cross section for the gamma-producing reaction.

Minimization of generated neutrons is important as MMGR do not require the use of neutrons, which contribute to unnecessary and significant dose during gamma radiography. In order to minimize the generation of neutrons, the threshold for (p,n) reactions need to be high and the cross section of (p,n) reactions need to be low. Generally, the threshold for (p,n) reaction in the target material decreases as Z increases, therefore low Z elements are preferable target materials. As such, the target reactions are $(\mathrm{p},\mathrm{p}'\gamma)$ reactions on low Z isotopes. Listed in Table. 3.1 are some reactions that would generate high energy gammas along with the reaction threshold and cross sections at certain energies. There are a few reactions of particular interest: the $(\mathrm{p},\mathrm{p}'\gamma)$ reactions on ^{12}C and $(\mathrm{p},\mathrm{p}'\gamma)$ reactions on ^{16}O. With 12 MeV protons, 4.4 MeV gammas were generated from $^{12}\mathrm{C}(\mathrm{p},\mathrm{p}'\gamma)^{12}\mathrm{C}$ reaction while 6.13, 6.92, and 7.12 MeV gammas were generated from $^{16}\mathrm{O}(\mathrm{p},\mathrm{p}'\gamma)^{16}\mathrm{O}$ reaction. All these reactions

have very high reaction cross sections with some more than five times higher than the previous system that utilized $^{11}\mathrm{B}(\mathrm{d},\mathrm{n}'\gamma)^{12}\mathrm{C}$ reactions for gamma generations. For example, the reaction cross section for 4.44 MeV gammas from $^{12}\mathrm{C}(\mathrm{p},\mathrm{p}'\gamma)^{12}\mathrm{C}$ reaction is 270 mb with 12 MeV incident proton. In comparison, the reaction cross section for 4.44 MeV gammas from $^{11}\mathrm{B}(\mathrm{d},\mathrm{n}'\gamma)^{12}\mathrm{C}$ reaction is 30 mb with 3.07 MeV incident deuteron. Furthermore, protons on $^{12}\mathrm{C}$ and $^{16}\mathrm{O}$ have a neutron generation threshold at 19.6 and 16.7 MeV respectively, which exceeds the specification of 12 MeV for the cyclotron in the proposed system.

The threshold of the reactions were determined using the Q-value Calculator, developed by the National Nuclear Data Center based on the two consecutive calculations [59]. The Q-value of a nuclear reaction is the amount of energy absorbed or released during the nuclear reaction. It can be determined from either the binding energies or the masses of the reactants and products using the following equation:

$$Q = B_{\mathrm{p}} - B_{\mathrm{r}} - E_{\gamma} = (m_{\mathrm{r}} - m_{\mathrm{p}}) \cdot 931 - E_{\gamma} \text{ MeV} \tag{3.3}$$

where B_{p} and B_{r} are the binding energies of the sum of all the products and the sum of all the reactants respectively, m_{p} and m_{r} are the masses of the sum of all the products and the sum of all the reactants respectively, and E_{γ} is the excitation energy for the state of specific gamma emission. Consider the reaction $\mathrm{x} + \mathrm{X} \rightarrow \mathrm{y} + \mathrm{Y}$ where x is the incident particle and X is the target at rest. If the energy of incident x is much less than the rest mass energy of the target X, then the conservation of mass and momentum under non-relativistic conditions can be used to calculate the energy threshold of the reaction:

$$E_{\mathrm{thre}} = -Q\frac{m_{\mathrm{y}} + m_{\mathrm{Y}}}{m_{\mathrm{X}}} \tag{3.4}$$

where E_{thre} is the minimum threshold kinetic energy that the incident particle needs to carry for the reaction to happen, m_{y} and m_{Y} are the mass of the products (two or more), m_{X} is the mass of the target, and Q is the reaction Q value calculated using Eq. 3.3.

In Table. 3.1, reaction cross sections at exactly 12 MeV are listed if there were

any existing literature. However, some of the cross sections are listed at a lower or higher energy due to the lack of existing data at 12 MeV. The neutron generation reactions with threshold are also tabulated for reference. The table also contains some reactions with low neutron and gamma generation threshold since they have large gamma cross sections. An example involving such isotopes are the $^{19}\mathrm{F}(\mathrm{p},\mathrm{x})$ reactions, which have a high cross section for 6.1 to 7.1 MeV gamma production and without an energy threshold. The $^{11}\mathrm{B}(\mathrm{d},\mathrm{n}'\gamma)^{12}\mathrm{C}$ reaction are also mentioned since it was the reaction utilized in the past proof-of-concept system. Table 3.1 also records the detection angle for the specific cross section because most of the reactions are not isotropic. Some reactions have an order of magnitude difference in cross sections between different angles of gamma generations. One example would be the 4.44 MeV gamma via $^{12}\mathrm{C}(\mathrm{p},\mathrm{p}'\gamma)^{12}\mathrm{C}$ reaction with 14 MeV incident proton. The ratio of gamma generation cross section between 45 and 90 degrees was approximately 2.19 and as high as 7.5 between 17.6 and 90 degree [60, 61, 62]. Sec. 4.5 contains a more detailed discussion on reaction cross sections at different angles and proton energies for the reactions that were actually used in the proposed system.

Reaction	E_γ ($E_{excitation\ level}$) [MeV]	Gamma Cross Section	Excitation Cross Section	Incident Energy [MeV]	Detection Angle [degree]	Threshold [MeV]	Ref.
$^{12}C(p,p'\gamma)^{12}C$	4.44	270 mb	-	12	all	4.81	[63]
$^{12}C(p,p'\gamma)^{12}C$	3.21+4.44 (7.65)	-	0.117 mb/sr	16.7	87.2	8.30	[61, 64]
$^{12}C(p,p'\gamma)^{12}C$	9.64	-	5.32 mb/sr	16.7	88.1	10.40	[61, 64]
$^{12}C(p,p'\gamma)^{12}C$	8.27+4.44 (12.71)	-	1.1 mb/sr	17.5	60	13.71	[64]
$^{12}C(p,p'\gamma)^{12}C$	12.71	-	1.1 mb/sr	17.5	60	13.71	[64]
$^{12}C(p,p'\gamma)^{12}C$	15.1	-	0.11 mb/sr	18.0	60	16.40	[64]
$^{12}C(p,\alpha'\gamma)^{9}B$	2.33	-	0.96 mb/sr	17.5	60	10.70	[64]
$^{12}C(p,n)^{12}N$	-	-	-	-	-	19.64	-
$^{12}C(p,np)^{11}C$	-	-	-	-	-	20.29	-
$^{10}B(p,p'\gamma)^{10}B$	0.718	-	8.5 mb	12	all	0.790	[65, 66]
$^{10}B(p,p'\gamma)^{10}B$	1.74	-	1.07 mb	12	all	1.915	[65]
$^{10}B(p,p'\gamma)^{10}B$	2.15	-	5.4 mb	12	all	2.366	[65]
$^{10}B(p,p'\gamma)^{10}B$	3.59	-	9.5 mb	12	all	3.95	[65]
$^{10}B(p,p'\gamma)^{10}B$	4.77	-	6.8 mb	12	all	5.25	[65]
$^{10}B(p,p'\gamma)^{10}B$	5.16	-	3.8 mb	12	all	5.68	[65]
$^{10}B(p,p'\gamma)^{10}B$	6.04	-	56.0 mb	12	all	6.65	[65]
$^{10}B(p,\alpha'\gamma)^{7}Be$	0.429	-	55 mb	4.0	all	0.0	[65, 66]
$^{10}B(p,n)^{10}C$	-	-	17.6 mb	4.0	all	4.876	[65, 67]
$^{10}B(p,n'\gamma)^{10}C$	3.35	-	2 mb	12	all	8.563	[65]
$^{11}B(p,p'\gamma)^{11}B$	2.125	0.9 mb/sr	-	3.13	90	2.32	[68]
$^{11}B(p,n)^{11}C$	-	11.8 mb/sr	-	3.58	0	3.017	[69]
$^{11}B(d,n'\gamma)^{12}C$	4.44	30.5 mb	-	3.07	4.0	0	[70]
$^{11}B(d,n'\gamma)^{12}C$	15.1	15.71 mb	-	3.0	4.0	1.62	[70]
$^{16}O(p,p'\gamma)^{16}O$	6.13	160 mb	-	12	all	6.52	[63]
$^{16}O(p,p'\gamma)^{16}O$	6.92	-	33 mb	12	all	7.36	[60]
$^{16}O(p,p'\gamma)^{16}O$	7.12	-	39 mb	12	all	7.57	[60]
$^{16}O(p,p'\gamma)^{16}O$	2.74+6.13 (8.87)	-	10 mb	12	all	9.43	[60, 71]
$^{16}O(p,p\alpha'\gamma)^{12}C$	4.44	64 mb	-	17	all	12.33	[63]
$^{16}O(p,np)^{15}O$	-	-	-	-	4.0	16.65	
$^{16}O(p,n)^{16}F$	-	-	-	4.0	4.0	17.22	
$^{19}F(p,p'\gamma)^{19}F$	0.110	6 mb/sr	-	5.5	135	0.116	[68, 72]
$^{19}F(p,p'\gamma)^{19}F$	0.197	14 mb/sr	-	5.5	135	0.207	[68, 72]
$^{19}F(p,p'\gamma)^{19}F$	1.24	1.6 mb/sr	-	5.5	135	1.31	[72]
$^{19}F(p,p'\gamma)^{19}F$	1.36	10.5 mb/sr	-	5.5	135	1.43	[72]
$^{19}F(p,\alpha'\gamma)^{16}O$	6.1-7.1	14.8 mb/sr	-	5.0	135	0.0	[72]
$^{19}F(p,n)^{19}Ne$	-	57 mb/sr	-	6.0	15	4.24	[73]

Table 3.1: Reactions of interest and their corresponding cross sections along with the reaction threshold. These include gamma and neutron emitting reactions. Existing data may not include cross section for the whole range of proton energies of interest nor for every excitation level. The table only presents cross section at specific energies (12 MeV for protons or 3 MeV for deuterons, or maximum cross section in existing data). Angles of the measurements are tabulated due to the angular dependence on different cross sections. For comparison, data for $^{11}B(p,n'\gamma)^{12}C$ reaction is also tabulated. For more details on cross sections for other angles and energies, see references listed on the table.

3.3 Dose comparison between dual-energy bremsstrahlung radiography and MMGR

3.3.1 Introduction and background

Using mononergetic gammas can result in much less dose to perform radiography than using bremsstrahlung X-rays. It is then important to compare the dose between a dual-energy bremsstrahlung radiography system and a MMGR system. Jones et al. [56] conducted a study to compare the differences in dose between a monoenergetic photon source and a bremsstrahlung source by using the general purpose Monte Carlo charge and neutral particle transport code (MCNPX). Jones et al. [56] estimated the gamma dose for a 10 MeV end-point bremsstrahlung source with 0.25 cm thick tungsten target and a monoenergetic photon beam of 10 MeV. At a stand-off distance of 10 m, the photon dose rate by bremsstrahlung was 0.41 Rem/min/μA while the photon dose rate by monoenergetic photon was only 0.062 Rem/min/μA. A major assumption was that the monoenergetic photon source was isotropic and had a unity conversion efficiency, which meant every incident particle produced one monoenergetic photon. This conversion efficiency is much less than unity in reality. Calculations in Sec. 4.5 suggest this conversion efficiency is in the order of 10^{-3}. The simulation conducted in Jones et al. [56] also provided the number of bremsstrahlung-induced and monoenergetic-induced photonuclear interactions in Pb with a stand-off distance of 10 m, and they are 6.09×10^{-11}/cm^3/source particle and 2.66×10^{-10}/cm^3/source particle respectively [56]. Using the interaction probability and dose rate given in Jones et al. [56], the dose from 10 MeV end-point bremsstrahlung source would be approximately 30 times higher than MMGR if the goal is to have the same number of photonuclear interactions in Pb at a stand-off distance of 10 m. Another paper by Jones et al. [74] gave the fractions of photons with energies greater than 6 MeV at a given standoff distance along the beam axis between a 10 MeV bremsstrahlung and a 10 MeV monoenergetic source [74]. The fractions at a 5 m standoff distance are 6.5% and 100% for a bremsstrahlung and a monoenergetic source respectively, which is

a significant difference. Although the study performed by Jones et al. [56] focus in long standoff distances and the collimation conditions between the monoenergetic photon source and the bremsstrahlung sources were different, it concluded that "monoenergetic photon sources provide overall photon doses that are much lower than comparable energy bremsstrahlung sources for at least up to 1 km inspections and 30-MeV interrogations" [56]. However, the results are not an apples to apples comparison as there exist no evaluation of material discrimination between the two sources.

3.3.2 Method and Simulations

To quantify the dose between the two different systems at the same material discrimination performance, a series of simulations were run using Grasshopper, an application based on the Geant4 development toolkit, to simulate particle interaction with materials by the Monte Carlo method [75, 76]. As explained in Sec. 2.2.6, a major advantage of using monoenergetic gamma rays is that the distinct gamma peaks at specific energy allow us to isolate the photon counts at specific energy for subsequent spectral analysis. The similar low energy bremsstrahlung continuum between the two energy spectra only lead to unnecessary dose without contributing to the meaningful signal. Although hardening of bremsstrahlung beam could be performed by filtering out X-rays below a few hundred keV, there is still significant similarity between the two bremsstrahlung continuums with different energy end-points in the higher energy region [57]. When these simulations were performed, the only X-ray filtering in the bremsstrahlung continuum was through the 1 cm W target used to generate the gammas for the bremsstrahlung source.

The goal of these simulations was to quantify the differences in dose between the bremsstrahlung-based system and the MMGR system when both were used to identify the spectral differences in gamma transmission between two mock cargoes (iron-iron vs iron-uranium). In the simulation, four gamma spectra were used for a simple cargo differentiation task. The four gamma spectra were:

- Bremsstrahlung gammas generated with 6 MeV electrons and a 1 cm thick W target
- Bremsstrahlung gammas generated with 9 MeV electrons and a 1 cm thick W target
- 4.4 MeV monoenergetic gammas generated from $^{11}B(p, n'\gamma)^{12}C$ reaction
- 15.1 MeV monoenergetic gammas generated from $^{11}B(p, n'\gamma)^{12}C$ reaction

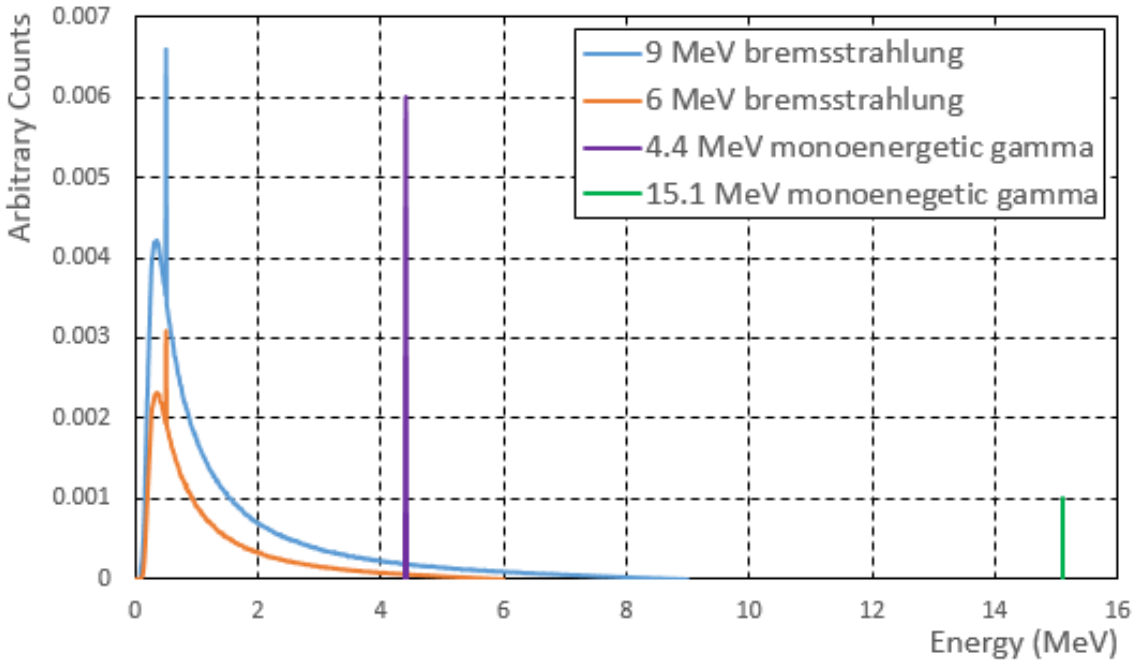

Figure 3-1: Source monoenergetic and bremsstrahlung spectra for dose comparison simulation. The 6 and 9 MeV bremsstrahlung spectra were proportional to the generation of simulated bremsstrahlung at a fixed source current. The ratio of 4.4 and 15.1 MeV monoenergetic gamma reflects the yield ratio from calculations in Sec. 4.5.

Fig. 3-1 shows the source gamma used. The separation between the monoenergetic 4.4 and 15.1 MeV gammas peaks is distinct while there is a large overlap between the 6 and 9 MeV bremsstrahlung gamma spectra, especially in the low energy region. In the simulation, even though NaI was used as the detector volume, detector resolution was not simulated in the energy spectrum. From the analysis of the spectrum, the 9 to 6 MeV bremsstrahlung photon ratio used in subsequent analyses was 2.5:1 and

it was determined by the number of emitted photons in the forward direction from the bremsstrahlung simulations with the same source current. Meanwhile, the 4.4 to 15.1 MeV monoenergetic gamma ratio was approximately 6:1, determined from yield calculations in Sec. 4.5 assuming $^{11}\mathrm{B}(\mathrm{p},\mathrm{n}'\gamma)^{12}\mathrm{C}$ reaction was used. The geometry and component of the experiment can be found in Tab. 3.2 and a side view of the simulation geometry is shown in Fig. 3-2.

Distance from source to center of object 1	1.2 m
Distance from center of object 1 to center of object 2	0.2 m
Distance from source to center of NaI detector	2.2 m
Full angle of the fan beam (width)	0.286°
Full angle of the fan beam (height)	29°
Size of NaI detector (height, width, length)	(5.08 cm, 10.16 cm, 40.64 cm)
Size of object 1 (Fe) for both cargo (height, width, thickness)	(80 cm, 40 cm, 25 cm)
Size of object 2 (Fe) for cargo 1 (height, width, thickness)	(4 cm, 10.16 cm, 5 cm)
Size of object 2 (U) for cargo 2 (height, width, thickness)	(4 cm, 10.16 cm, 2 cm)

Table 3.2: Geometric parameters of the simulation setup for the dose comparison simulations.

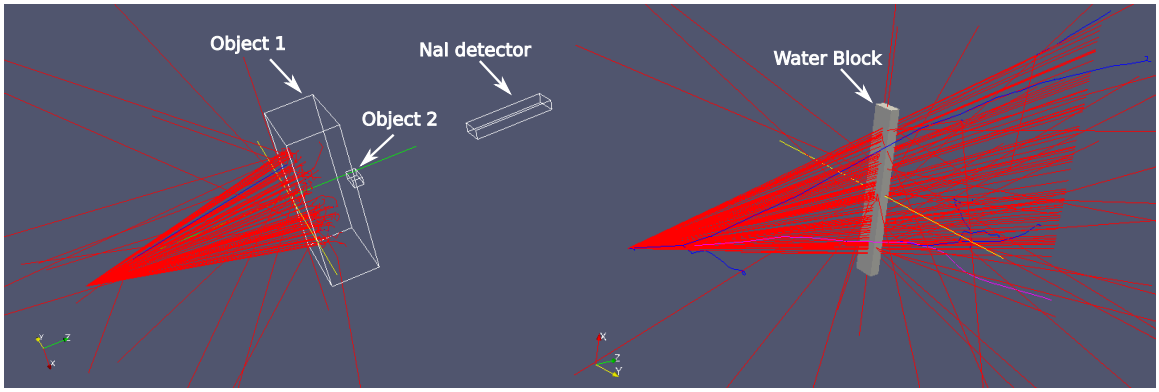

Figure 3-2: Left: Visualization of the simulation setup for the dose comparison simulations with parameters found in Tab. 3.2. The object 2 in this figure is a block of Fe (cargo 1). Right: Visualization of the simulation setup for acquiring the dose induced from the source photons to a block of water.

To quantify the ability to distinguish the change of object 2 from iron to uranium

between two mock cargoes, an index of separation was used:

$$F = \frac{|r_2 - r_1|}{\sqrt{\sigma_{r_1}^2 + \sigma_{r_2}^2}} \tag{3.5}$$

$$r_1 = \frac{S_{\text{cargo}_1, E_{\text{high}}}}{S_{\text{cargo}_1, E_{\text{low}}}} \tag{3.6}$$

$$r_2 = \frac{S_{\text{cargo}_2, E_{\text{high}}}}{S_{\text{cargo}_2, E_{\text{low}}}} \tag{3.7}$$

where $S_{\text{cargo}_1, E_{\text{high}}}$ and $S_{\text{cargo}_1, E_{\text{low}}}$ is the signal from the high energy and low energy transmitted spectra of cargo 1 (Fe+Fe) respectively. The same definition is used for $S_{\text{cargo}_2, E_{\text{high}}}$ and $S_{\text{cargo}_2, E_{\text{low}}}$ but for cargo 2 (Fe+U) instead of cargo 1. The high and low energy transmitted spectra for MMGR were the 15.1 and 4.4 MeV transmitted spectrum respectively. As for bremsstrahlung, they were the 9 and 6 MeV bremsstrahlung transmitted spectra. MMGR simulation used the counts from 3.3 to 4.9 MeV as the 4.4 MeV signal and the counts from 11.5 to 16 MeV as the 15.1 MeV signal. As for bremsstrahlung simulations, the total counts from 6 and 9 MeV transmitted spectra were used as the signal, based on the fact that most deployed bremsstrahlung-based radiography system mentioned in previous sections used 5mm×5mm×30mm $CdWO_4$ detector as a calorimeter to measure the total deposited energy, hence there were no energy cuts for analysis [77]. The goal for comparison was to obtain the same F for both sources. This led to having the number of events needed (total number of source photons) for bremsstrahlung source and MMGR source to achieve the same F value.

Another simulation was ran in order to convert the source counts from both sources to dose. As seen in Fig. 3-2, a slab of water (80 cm×10 cm×5 cm in size) was placed at the location of object 1 in order to capture the whole fan beam. Water was used for this conversion due to the fact that human are composed of 60 to 70% water. A total of 10^6 source photons were generated from each of the four source spectra. The energy deposited from each of the sources were tallied and converted into Gy by dividing the deposited energy with the mass of the water block. As such, dose conversion in units of Gy/million source photons were found for each of the four source gamma spectra. The simulated dose conversions are as follows:

	6 MeV brem	9 MeV brem	4.4 MeV MMGR	15.1 MeV MMGR
Energy deposited (GeV)	154	176	383	596
μGy	6.15	7.03	15.33	23.89

Table 3.3: Total energy deposited and the induced dose to a block of water from 10^6 source photons sampled from each of the four source spectra.

3.3.3 Result

The resulting simulated transmitted spectra for the two cargo scans using two different sources are shown in Fig. 3-3. In order to achieve a F of 4.2, the number of source photons used for MMGR at 4.4 and 15.1 MeV were 2.55×10^7 and 4.25×10^6 respectively. For the same F of 4.2, the number of 6 and 9 MeV source bremsstrahlung photons used were 4.68×10^8 and 1.17×10^9 respectively. These counts get converted to 0.49 mGy for the 4.4/15.1 MeV MMGR system and 11.1 mGy for the 6/9 MeV bremsstrahlung system.

The results from these simple simulations demonstrated the dose from the 6/9 MeV bremsstrahlung system was 22.6 times higher than the dose from 4.4/15.1 MeV MMGR. However, this result was the upper bound on the dose differences as the simulations did not take into account the gamma or neutron induced background, the resolution of the detector, and most importantly, the spacial resolution of the radiography system and the possibility of spectral hardening of the bremsstrahlung beam. Additionally, the results do not address the potential of using more than two monoenergetic gamma for radiography. However, these served the general purpose of providing an estimation on the dose difference between the two systems.

It is also important to note there exists different ways to utilize bremsstrahlung photons for material discrimination. In a paper by Anatoli Arodzero [78], an Adaptive Multi-Energy Cargo Inspection System (AMEXIS) was being developed using a linax-based, adaptive, ramped-energy Modulated-Energy X-ray Pulses (MEXP) for advanced radiography and material discrimination analysis [78, 79]. It showed the possibility to perform radiography using an X-ray source and achieved four Z-groups of material discrimination with the given examples of lead, steel, aluminum

and polyethylene, at a dose rate of 0.125 rad per scan line for a moderately loaded cargo [78].

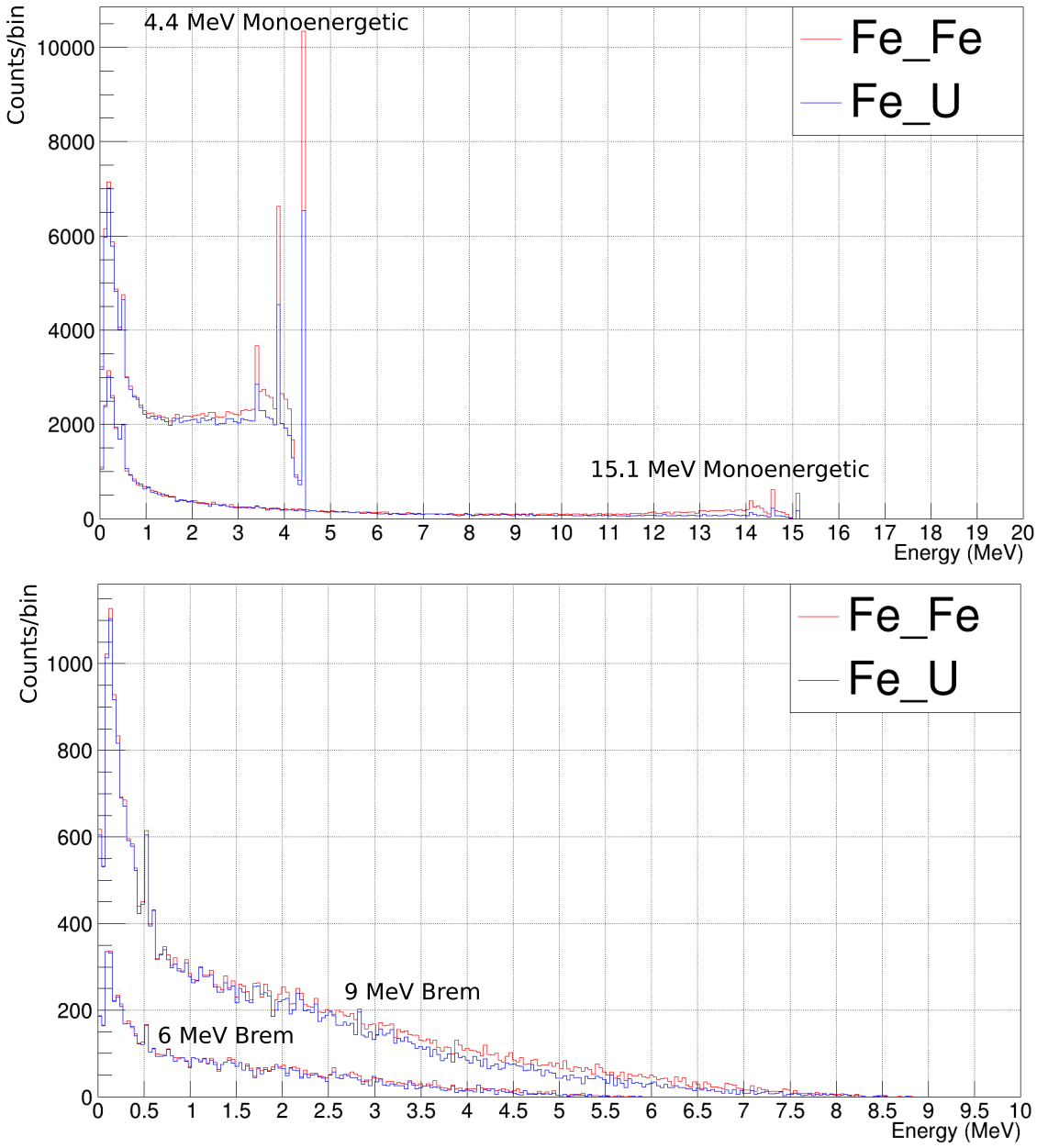

Figure 3-3: Simulated gamma spectra from the results of all simulations performed. The figure on the top contains all the spectra for MMGR simulations while the figure on the bottom contains all the spectra from bremsstrahlung-based system. The red colored spectra are the transmitted spectra from cargo 1 (Fe+Fe) simulations while the blue colored transmitted spectra are from cargo 2 (Fe+U) simulations. In these simulation, a fan beam was used with the simulation geometry mentioned in Table. 3.2

3.4 Past MMGR system and its limitations

The Laboratory of Nuclear Security and Policy (LNSP) at MIT previously conducted a few proof-of-concept MMGR experiments using dual monoenergetic gammas from an accelerator-based system [6, 7]. Using the same system, several neutron radiography experiments were performed as well [3, 4]. $^{11}\mathrm{B}(\mathrm{d},\mathrm{n}\gamma)^{12}\mathrm{C}$ was the reaction used in these past experiments, with a positive Q value of 13.73 MeV that was released from the reaction [59]. Deuterons were accelerated to 3 MeV by a pulsed Radio Frequency Quadrupole (RFQ), and 4.44 and 15.1 MeV gammas were generated via the de-excitation of $^{12}\mathrm{C}^{*}$ from $^{11}\mathrm{B}(\mathrm{d},\mathrm{n}\gamma)^{12}\mathrm{C}$ reaction for MMGR. It was demonstrated that this MMGR system along with an improved reconstruction algorithm has the capability to reconstruct Z_{eff} with a specificity of 3 in Z, even separating different high Z materials such as tungsten and lead [7].

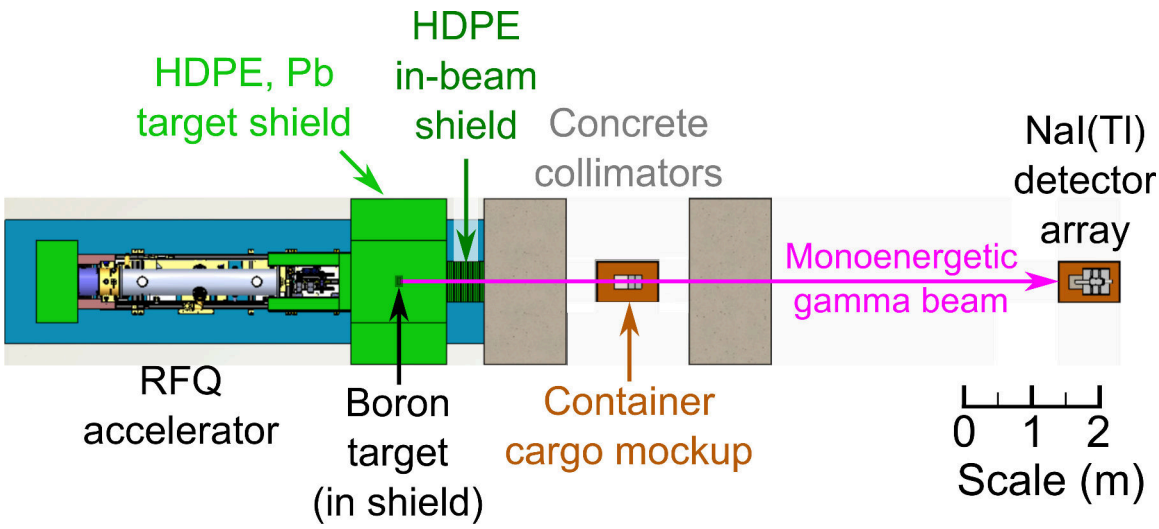

Figure 3-4: Schematic of the past MMGR system used for experiments in Ref. [3, 4, 5, 6, 7]. Reprinted from O'Day et al. [5]

In this past MMGR system, the Accsys Technologies DL-3 Radio Frequency Quadruple used was a very large and bulky system, measuring more than four meters in length as shown in Fig. 3-4. It also required a long setup time for initial alignment and calibrations. As a result, this particular system is not well suited for use in a deployable system. Small RFQ capable of accelerating particles to a few MeV do exist,

but they come with their own disadvantage: the source particle and energy is fixed, limiting the reactions that could be utilized. For systems that accelerated deuterons to 3 MeV, the $^{11}\mathrm{B}(\mathrm{d},\mathrm{n}\gamma)^{12}\mathrm{C}$ reaction used to generate the 4.4 and 15.1 MeV gammas was another source of disadvantage. This reaction generated a relatively low yield of gammas (1.31×10^{-5} and 3.39×10^{-6} photons per source deuteron) while generating neutrons at the same time. For the sole purpose of MMGR, these neutrons produced from the reaction generated unnecessary and significant radiation dose.

Chapter 4

Compact Superconducting Cyclotron for MMGR

This chapter focuses on the details of the accelerator used in this PhD thesis, including but not limited to the superconducting cyclotron's specifications and internal components. A significant portion of this PhD study was spent on the target design and performance characterization of the cyclotron, which was the first machine manufactured by Ionetix Corporation and not designed for radiography. Instead, it was designed with an internal target for medical isotopes production. Operational routines and parameters related to the cyclotron are discussed below to provide a general knowledge about the complexity of running the cyclotron and potential burdens for mobile applications. A list of cyclotron maintenance and upgrades during the span of this PhD work are tallied as well to show the downtime of this new cyclotron design and provide insight on its reliability.

4.1 Accelerator choices for MMGR

While many accelerators are now commercially available, the options are limited for ones usable in a deployable MMGR system. A deployable MMGR system needs to be readily mobile and with a maximum weight of 26,000 lbs (11.8 tonnes), the weight limit for Class A commercial driving license in the U.S. [80]. It also corresponds to

a Class 6 medium duty truck, in which the maximum gross vehicle weight rating is 26,000 lbs (11.8 tonnes), according to the U.S. Department of Transportation Federal Highway Administration [81, 82]. This maximum gross weight of 26,000 lbs (11.8 tonne) also includes the curb weight of the truck, which is approximately 9,000 lbs (4.1 tonnes) [83].

The accelerator should also accelerate ions to energies above 10 MeV to enable the use of low energy nuclear reactions to generate multiple monoenergetic gammas. With such limitations in mind, many accelerators such as the RFQ used for previous MMGR studies, are too large, too heavy, and require too long of a set up time for initial alignment and calibration that renders it impractical for mobile application [6, 7, 5]. Small RFQ systems capable of accelerating particles to a few MeV do exist but those come with their own disadvantage: the source particle and energy is fixed, limiting the reactions that could be utilized. Furthermore, a 3 MeV deuteron accelerator utilizing $^{11}\mathrm{B}(\mathrm{d},\mathrm{n}\gamma)^{12}\mathrm{C}$ reaction would generate unnecessary and significant radiation dose from the neutrons. Other accelerators such as a DC tandem Van de Graaff accelerator have a high current output, can accelerate different particles, and is very reliable; however, Van de Graaff accelerators are large and heavy. For example, the 15 MV tandem Van de Graaff at Brookhaven National Laboratory is 24 m in length [84]. As mentioned in Sec. 3.3, bremsstrahlung based systems are also not favorable due to the high dose induced during the screening compared to a monoenergetic based system.

The last type of accelerator discussed here will be the cyclotron, a well-developed technology first established by Ernest Lawrence in 1932. The cyclotron accelerates charged particles along a spiral trajectory by the combination of a static magnetic field and varying electrical fields between the "Dees". Commercially available cyclotrons such as Cyclone KIUBE and Cyclotron 30 can be used to accelerate protons to 18 and 30 MeV respectively [85, 86]. However, the bulky conventional magnets used to generate a magnetic field of 1.7 T makes the cyclotrons large and heavy. Cyclotron 30 weighs over 45.4 tonnes and is 8 m by 7 m by 4 m, while the newer Cyclone KIUBE manufactured by IBA still weighs 16.3 tonnes without self-shielding and is

2 m by 2 m by 2 m, making both highly unsuitable for mobile applications. As superconducting technology becomes more commonplace and readily available, there is significant effort to develop a compact superconducting cyclotron. Ideally, one would want a cyclotron capable of accelerating different particles to as high as 20 MeV while generating higher magnetic fields and using smaller magnets.

4.2 Cyclotron specification

The cyclotron used in this thesis is the ION-12^{SC} compact superconducting isochronous cyclotron made by Ionetix Corporation. It is located in the Vault Laboratory in building NW13 at MIT. This cyclotron is named CHARON (Cyclic Hydrogen Accelerator for Radiography and Other Nuclear-applications) and it can accelerate protons to approximately 12 MeV. It is a novel superconducting cyclotron using niobium-titanium (NbTi) superconductor for the magnet [87]. NbTi has a critical temperature of approximately 10 K [88]. Superconducting technology enables the magnetic field in the cyclotron to reach as high as 4.5 T, according to the manufacturer specification [89, 90]. It is also very compact at only 89 cm in diameter, 196 cm in height, and weighs only 2.27 tonnes [91]. Fig. 4-1 shows a photo of CHARON with a person next to it for scale. CHARON is an isochronous cyclotron, meaning the axial magnetic field is designed to increase with radius to compensate the effects of relativistic mass increase of protons at 12 MeV. As protons accelerate, the cyclotron frequency remains constant.

Derived from the Lorentz Force Law, the gyroradius, gyrofrequency, and period of the cyclotron have the following relations:

$$r_g = \frac{mv}{qB(r)} \tag{4.1}$$

$$T_g = \frac{2\pi r_g}{v} \tag{4.2}$$

$$f_g = \frac{qB(r)}{2\pi m} \tag{4.3}$$

Figure 4-1: Isometric view of the cyclotron with the author next to it for scale.

where r_g is the gyroradius, m is the mass of the ion, v is the velocity of the ion, q is the charge of the ion and $B(r)$ is the axial magnetic field at radius r, T_g is the period of the cyclotron, and f_g is the gyrofrequency.

From Eq. 4.1, 4.2 and 4.3, the cyclotron energy and magnetic field was estimated to confirm the manufacturer's specifications. From the specification, the final acceleration radius of the cyclotron is 11.5 cm [91]. The experimentally measured gyrofrequency was 67,360 kHz, which gives a calculated magnetic field of 4.42 T and a calculated final proton energy of 12.4 MeV. Since the radiofrequency (RF) voltage

oscillates from -17 kV to +17 kV, giving up to 34 KeV to a proton each revolution around the cyclotron, the proton is estimated to have cycled approximately 360 revolutions in the cyclotron during acceleration, the equivalent to more than a quarter of a km in path length travelled.

In addition to the cyclotron, there are three main auxiliary components for CHARON's operations: the water cooled PLC control rack, the cryocooling system, and the Fluid Chillers Inc. WAT 5000 Chiller [92, 93]. Because the superconducting magnet needs to be cooled down to 5 K for normal operations, a cryocooler has to be used. In the current setup, the Cryomech water cooled CPA1110 cryo compressor along with PT-415 two-stage pulse tube (PT) cryocooler provide the necessary cooling of the magnet down to 5K [92, 94]. The cryo compressor compresses helium to 280 psi and subsequently expands the gas to 100 psi via a piston, which cools down the cryohead by the pressure differential, and recirculates the helium gas back to the compressor. The cooling capacity of the two-stage cryosystem is 1.5 W at 4.2 K and 40 W at 45 K. The cryogenic helium gas circulates in a closed loop and does not deplete over time, hence the system does not require refilling after the initial setup. The size of the cryo compressor is 61 cm by 61 cm by 78 cm and the power consumption is 10.7 kW and runs at 3 phase 230 V. The cryo compressor itself is cooled by a closed chilled water loop provided by the Fluid Chillers Inc. WAT 5000 Chiller.

The WAT 5000 chiller is a 107 cm by 70 cm by 167 cm water cooled chiller with an integrated pump and tank system. It has a cooling capacity of 61,000 BTUs/hr and a two loop system where the primary loop uses the unfiltered MIT facility water at 100 psi chilled to 9 degree Celsius while the secondary loop is a closed loop of distilled water at 12 degree Celsius. This system provides the necessary cooling for the cryo compressor, RF power supply on the PLC rack, and different components of the cyclotron. For example, the RF resonator of the cyclotron is cooled with chilled water flowing at 2.5 gpm. The chiller runs at 3 phase 230 V and consumes approximately 12 kW of power.

The last major component for CHARON is the PLC control rack. It contains all the controllers and communication modules necessary for CHARON's operations,

including the RF combiner, RF power supply, RF controller, magnet power supply, ion source power supply, cryogenics control, turbo pump control, and all other controllers. The rack measures 94 cm by 58 cm by 195 cm. Some of the components are cooled by the chilled distiller water such as the two 3 kW RF power supply that provide the necessary power to the RF system. Photos of all three systems mentioned are shown in Fig. 4-2.

Figure 4-2: Photos of the three main auxiliary components. From left to right is the CPA1110 cryo compressor, WAT 5000 chiller, and the PLC control rack.

4.3 Ion source and the dummy Dee

The ion source and the dummy Dee make up two critical components of the cyclotron. In CHARON, the accelerating voltage of the Dee oscillates between +17 kV and -17 kV at a radiofrequency of 67,360 kHz while the dummy Dee is held at ground. The region of acceleration for the protons lies in the gap between the Dee and dummy Dee. Fig. 4-3 shows a photo of the Dee and dummy Dee. A piece of ceramic insulator supports the Dee stem, which connects to the Dee inside the cyclotron. During normal operations, arcings might occur between the Dee stem and the RF cavity, leading to normal degradation of this ceramic insulator. Misalignment of the Dee stem could induce uneven stress on the ceramic insulator that rapidly increases

wear and tear of the equipment, and more frequent replacement of the insulator. In the first two years of operations alone, a total of four insulators have broke.

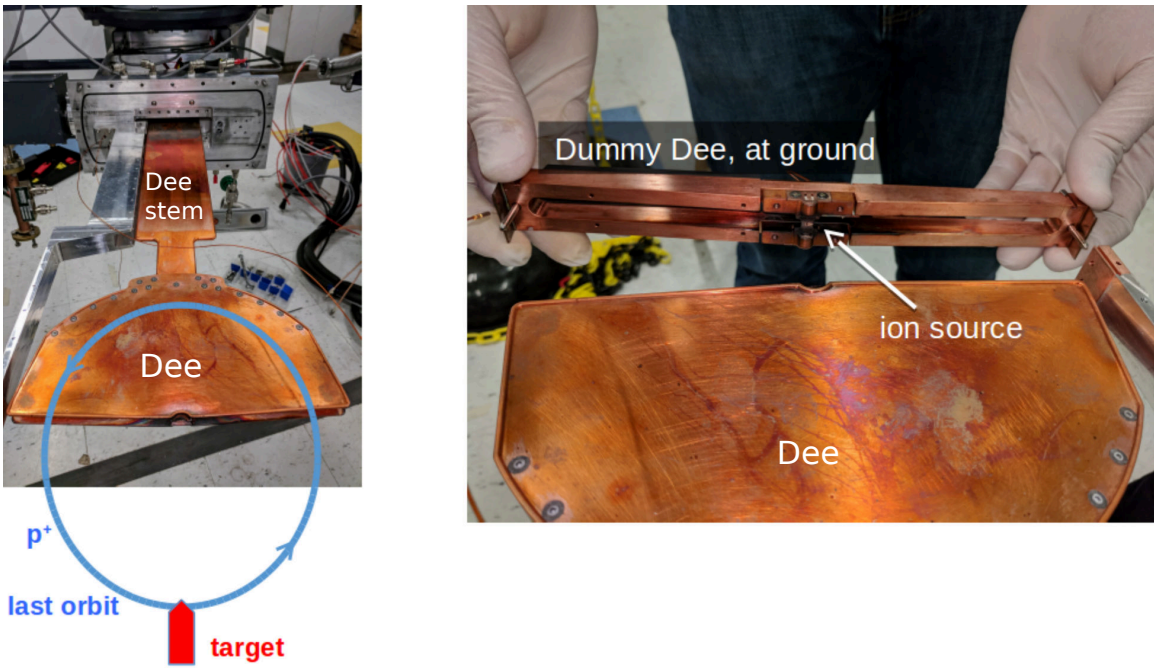

Figure 4-3: Photo of the Dee, dummy Dee, and the Dee stem with the approximate location of the last accelerated orbit and water target sketched.

CHARON uses a cold cathode penning ion source with two high negative voltage tantalum or titanium cathode with boron nitride insulators, which subsequently ionizes the hydrogen in the chimney of a single-body of Beryllium Copper as shown in Fig. 4-4 [89]. The source opening is a 2×0.5 mm slit with a 30 degree bevel at 2 mm offset from the center of the cyclotron to initially pull and accelerate the protons close to the slit [90]. The flow of gas and operating current of the arc in the ion source ranges from 0.3 to 1.0 sccm and 0.1 to 15 mA respectively. The voltage for the ion source automatically adjusts between 600 and 1,800 V, according to the ion source current output. At the time of this thesis study, the nominal operating ion source current was approximately 4 mA at 1,300 V to produce 5 μA of beam on water target and 0.8 μA of beam on the graphite collimator. Though the power consumption of the ion source fell below 6 W, the temperature rose significantly during operations due to the poor cooling performance of the dummy Dee, which negatively affected the

output and caused the ion source to become unstable. With an unstable ion source, the proton beam became unfocused and the amount of beam hitting the water pocket and the graphite collimator would start to vary over time. Towards the end of this PhD study, a new cooling circuit was installed to directly cool the dummy Dee and the ion source to address the heating issues discussed above. However, no radiography experiments were performed with the cyclotron after the upgrade. Additionally, two other ion sources were manufactured with 3 and 4 mm extraction slits (see Fig. 4-4) instead of the standard 2 mm slit in an attempt to produce a much higher beam current on target. However, these were not tested in this PhD study.

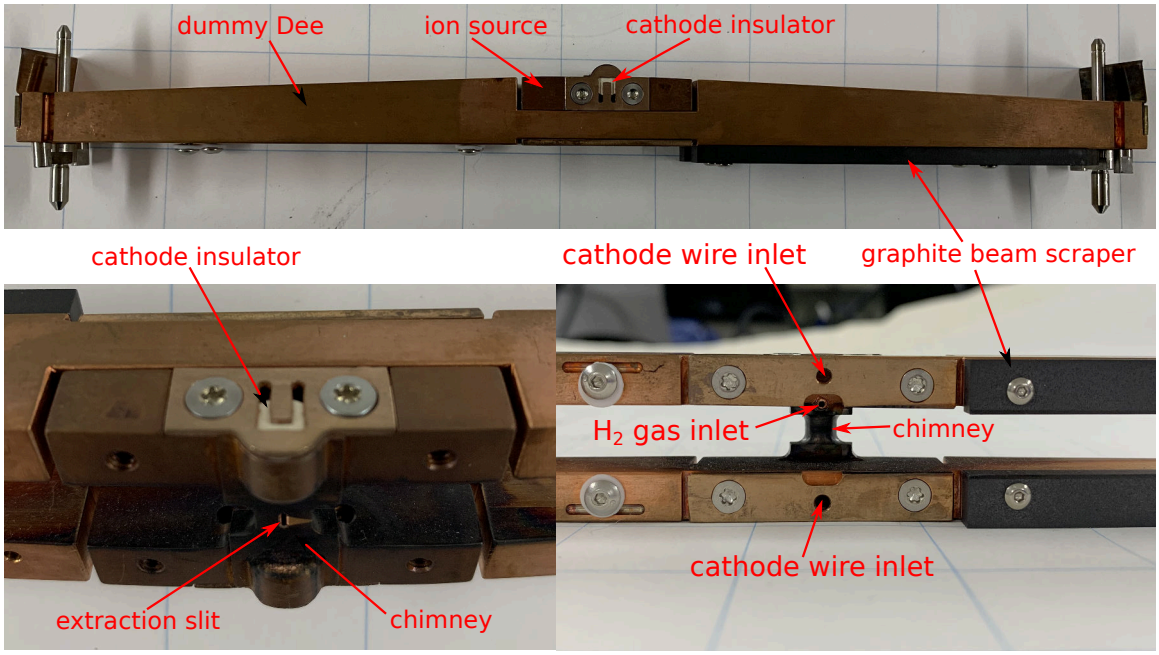

Figure 4-4: Top: Photos of the full assembly of the first generation dummy Dee, including the ion source and the graphite scraper. Bottom left: Zoomed in image of the ion source showing the boron nitride cathode insulator, chimney, and extraction slit. Bottom right: Front view of the ion source showing the hydrogen gas inlet and cathode wire inlet of the ion source.

Fig. 4-4 details the ion source design, including the cathode insulator, extraction slit, the chimney, and all the inlets. It also shows the first generation dummy Dee design with indirect cooling via the heat conduction of two copper leaf spring. The indirect conduction cooling design of the leaf spring led to beam instability and reduc-

tion in ion source performance due to the increase in ion source temperature during operations. This PhD study utilized the second dummy Dee design, replacing the leaf springs with two coil springs and a much larger aluminum contact. Although this improved the cooling of the ion source, significant heating still occurred during operations. The latest upgrade of CHARON completely rebuilt the RF stem support and dummy Dee, and introduced active cooling to the dummy Dee. However, no radiography data has been collected since the latest upgrade. Another feature of the dummy Dee is the graphite beam scraper. It is 10 cm long and 4 mm thick with a 9.2 mm gap in the middle covering the copper dummy Dee. The purpose of the beam scraper is to prevent protons that are not focused and/or fully accelerated from gaining more energy. Those protons will be stopped by the graphite to prevent proton activation of the copper dummy Dee. A series of diagnostic tests have been performed to show that the 4.4 gammas did not originate from the scraper since most of the protons hitting the graphite scraper fell below the energy threshold.

4.4 Target design and considerations

Fig. 4-5 details the target design of CHARON. The water target is located 14.1 cm from the center of the cyclotron. This target contains a static 3 mL liquid pocket held together by a target window and window frame. The static liquid pocket was actively cooled by a closed loop of deionized chilled water. In front of the water target, an electronically insulated graphite collimator collimates the proton beam horizontally (radially). From multiple beam imaging experiments, the beam spot was found to have a radial width of approximately 12 mm (FWHM) and a height of 3 mm (FWHM). In the target assembly, two wires independently measured the current from protons stopped by the front water target assembly and the graphite collimator using two 9103 USB Picoammeter made by RBD Instruments. In this design, approximately one fifth of the beam was stopped by the graphite collimator, creating 4.4 MeV gammas while the rest was attenuated by the 50 μm aluminum window and subsequently stopped in the static water pocket, creating 6.13, 6.92, and 7.12 MeV gammas. The average

current on the water and collimator for all 19 radiography experiments were at 6.0 μA and 0.56 μA respectively.

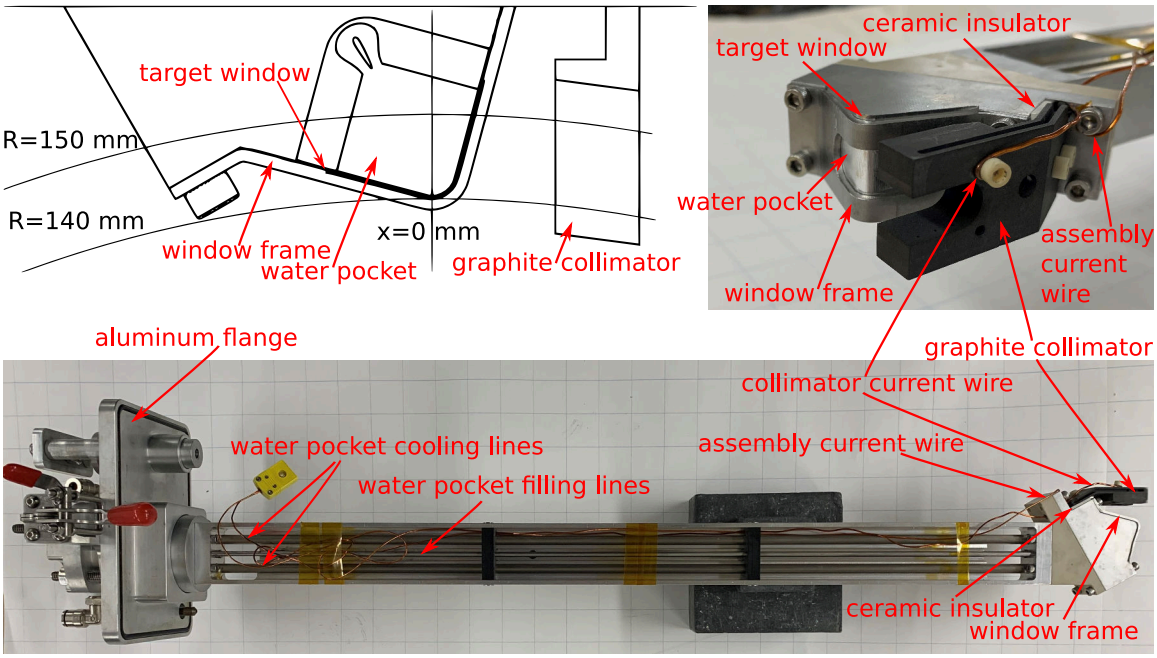

Figure 4-5: Top left: Sketch of the top view of the front water assembly with the proton trajectory drawn and radius labelled along with the target window, window frame, water pocket, and the graphite collimator. Top right: an isometric view of the front water assembly with all parts labelled. Bottom: top view of the full water target assembly with water pocket cooling lines and filling lines shown.

From the list of nuclear reactions, water and PF-5080 (perfluorooctane,C_8F_{18}) were tested as a target material in the liquid pocket. When the beam hit the liquid pocket, PF-5080 released fluorine gas through a possible combination of thermal, chemical, and nuclear reaction. As a result, the 50 μm thick aluminum window ruptured after just 30 s of irradiation at 5 μA, aborting the experimental run. Unless alternative circulation methods can be found to handle this issue, PF-5080 is not a suitable target material, leaving water as the only candidate material.

The original window designs from Ionetix were also modified in an attempt to increase gamma production and reduce material activation. While kapton windows have a low neutron yield from proton induced reactions, it makes a poor conductor of heat (1.76 $Wm^{-1}K^{-1}$ at 300 K) and tends to degrade and embrittle over time [95].

With CHARON accelerating protons to approximately 12 MeV and 5 μA for this study, 72 W of energy were transferred into the window by the protons. As a result, the 125 μm thick kapton window would break after only operating for an hour. A low Z metal such as aluminum makes the next logical choice for the window as low Z materials have a higher (p,n) reaction threshold, and therefore less neutron production. Aluminum has a thermal conductivity over 100 times higher than kapton, at 205 $\mathrm{Wm^{-1}K^{-1}}$ [96]. Even then, active water pocket cooling will be necessary. The aluminum window also needs to be as thin as possible to reduce the loss in proton energy before reaching the water to maximize gamma yield and reduce neutron creation. A series of short tests were conducted with aluminum windows at thicknesses of 25, 50, and 75 μm. The 25 μm thick aluminum window was found to be unusable after only an hour of operating due to rapid deformations that caused vacuum to leak from the water pocket.

Besides the liquid and the window, the window frame was also specially designed to minimize activation so the target could be handled sooner with less dose and generate less gamma background during the experiment. The window frame is composed of aluminum rather than the originally designed steel. Below is the record of neutron and gamma dose measurements by the Thermo Fisher Scientific ASP2e neutron survey meter and Ludlum 9DP-1 dosimeter at a distance of 259 cm from the target behind the concrete and lead collimator respectively [97, 98]. A schematic for the locations of the dosimeters is provided in Fig. 5-1.

As seen in Table. 4.1, there was a significant increase in gamma and neutron dose when the target window changed from 125 μm thick kapton to 50 μm thick aluminum to 75 μm thick aluminum. However, the neutron and gamma dose appear to remain the same regardless of the window frame material. This indicates only a minimal amount of proton beam actually hit the window frame when the beam was tuned and focused with optimal parameters. Measurements taken previously indicated more radioactivity in the steel frame compared to the aluminum frame after running the experiments. The primary cause of such higher radioactivity was due to the radioactive isotopes generated from proton induced reactions on steel being

Materials	current on water [uA]	current on jaw [uA]	neutron dose rate [mRem/min]	gamma dose rate [mR/min]
Without HDPE shield				
Al frame + 125 um kapton + water	5.02	0.28	0.058	0.26
Al frame + 50 um Al + water	5.1	0.50	0.284	0.32
Steel frame + 50 um Al + water	4.38	0.39	0.259	0.30
Al frame + 75 um Al + water	4.8	0.56	0.420	0.40
Steel frame + 75 um Al + water	4.58	0.72	0.395	0.36
With HDPE shield				
Al frame + 125 um kapton + water	4.8	0.24	4.32×10^{-4}	0.128
Al frame + 50 um Al + water	5.2	0.47	4.88×10^{-3}	0.181
Al frame + 75 um Al + water	4.82	0.45	5.36×10^{-3}	0.172
Steel frame + 75 um Al + water	4.7	0.65	5.7×10^{-3}	0.163

Table 4.1: Tabulated experimental data of neutron and gamma dose measurements at a distance of 259 cm from the target behind the concrete and lead collimator measured by the Thermo Fisher Scientific ASP2e neutron survey meter and Ludlum 9DP-1 dosimeter respectively. Different combinations of the target window and target frame have been tested. The data were also measured with and without 20.32 cm of HDPE for neutron dose reduction during the screening. The duration of the experimental run for each data subset in this PhD thesis was six minutes with an average current on water and collimator at 6.0 μA and 0.56 μA respectively

longer lived than those from protons on aluminum. According to the rule of ALARA, the aluminum window frame was a much more suitable choice since it reduced the dose to the person handling the target. Because of these considerations, the target combination used were aluminum frame with 50 μm thick aluminum window and water pocket. Table. 4.1 also shows significantly reduced neutron dose by more than a factor of 50 if 20.32 cm of HDPE were in place. In order to translate the dose rate to dose for a typical radiography scan, the duration of the experimental run for each data subset in this PhD thesis was six minutes with an average current on water and collimator at 6.0 μA and 0.56 μA respectively.

4.5 Gamma yield calculation

To produce the necessary gammas, the internal target used was a mixed target consisting of a graphite collimator and a static water pocket with a 50 μm thick aluminum window in front. With 12 MeV photons and graphite (C) target, the

strongest de-excitation gamma line was 4.44 MeV from the ^{12}C(p,p$'\gamma$)^{12}C reaction. From oxygen (in water), gammas were produced by the de-excitation of ^{16}O* through (p,p$'\gamma$) reaction at energies of 6.13, 6.92, and 7.12 MeV. Using the existing cross-section data for the above reactions listed in Table.4.2 [60, 63] and the stopping powers of proton [99], the gamma yield per incident proton were calculated by performing a numerical integration with the following equation:

$$yield = \int_{E_{th}}^{E_p} dE \frac{\sigma(E)}{-\frac{dE}{dx}(E)} \cdot \frac{\rho N}{A} \tag{4.4}$$

where E_{th} is the threshold energy of corresponding (p,p$'\gamma$) reaction, E_p is the energy of the accelerated protons (12 MeV in the current accelerator), $\sigma(E)$ is the cross section of the (p,p$'\gamma$) reaction at energy E, $\frac{dE}{dx}(E)$ is the stopping power of the proton in the target material at energy E, ρ is the density of the material, N is the Avogadro number, and A is the atomic weight of the target. The energy steps used in the numerical integration were 10 eV and $\frac{dE}{dx}(E)$ at each step were calculated from interpolation of the available proton stopping power data (-dE/dx), taken from the "stopping power and range tables for protons database", published by the National Institutes of Standards and Technology [99]. The database used several methods with multiple corrections to evaluate the stopping power. One of the base equations was the Bethe formula:

$$-\frac{dE}{dx} = \frac{4\pi e^4 z^2}{m_0 v^2} NZ\{ln(\frac{2m_0 v^2}{I}) - ln(1 - \frac{v^2}{c^2}) - \frac{v^2}{c^2}\} \tag{4.5}$$

where ze and v are the charge and velocity of the incident particle, m_0 is the rest mass of electron, c is the speed of light, N is the number density of the stopping material, and Z is the atomic number of the stopping material.

The range of the incident particle was then calculated by performing another numerical integral using the formula:

$$Range = \int_{E}^{0} -\frac{dx}{dE}(E) \cdot dE \tag{4.6}$$

where E is the energy of the incident particle. The range of protons at 12 MeV in graphite and water were 1.12 cm and 1.7 cm respectively. Based on the trajectory of the protons sketched in Fig. 4-5, most of the proton beam would either be fully stopped by the graphite collimator or the water in the water pocket. Similarly, the cross sections used in each of the 10 eV steps for the numerical integral were calculated via linear interpolation of existing data from Table. 4.2. Using all the information gathered, the 4.44, 6.13, 6.92, and 7.12 MeV gamma yields were calculated and plotted in Fig. 4-6. Similarly, the gamma yields from the old RFQ-based system were also calculated using Table. 4.3. As seen in Fig. 4-6, most of the gamma yields from the (p,p$'\gamma$) reactions used in CHARON exceed the yield of gammas from the old (d,nγ) reaction, with some more than 100 times higher.

It is important to note all the cross section data used were averaged over all angles, not given as a specific angle. However, gamma cross sections have an angular dependency with gamma yields varying strongly as the measurement angle changes relative to the proton beam direction. To estimate the impact of measurement angle, literature values for the ratio of cross sections at different angles were examined. For 4.44 MeV gamma and 14 MeV incident proton, the ratio of cross sections was 2.19 when comparing 45 to 90 degrees, and was as high as 7.5 when comparing 18 to 90 degrees [60, 61, 62]. The ratios of cross sections between 45 and 90 degree for 6.13, 6.02, and 7.12 MeV gammas are approximately 1.36, 1.20, and 1.03 respectively [60, 100]. Because all the experimental gamma transmission measurements were made at 90 degree while the theoretical yield calculation used integrated cross sections across all angles, there could be a discrepancy of more than a factor of 2 between the theoretical and experimental yield results.

Reaction	^{12}C(p,p$'\gamma$)^{12}C	^{16}O(p,p$'\gamma$)^{16}O					^{16}O(p,p$\alpha\gamma$)^{12}C
Transition	^{12}C*4.44 $\rightarrow$ g.s.	^{16}O*8.88 $\rightarrow$ ^{16}O*6.13	^{16}O*6.13 $\rightarrow$ g.s.	^{16}O*6.92 $\rightarrow$ g.s.	^{16}O*7.12 $\rightarrow$ g.s.	^{16}O*8.88 $\rightarrow$ g.s.	^{12}C* $\rightarrow$ g.s.
E_γ (MeV)	4.44	2.74	6.13	6.92	7.12	8.88	4.44
Reference	[63]	[60]	[63]	[60]	[60]	[60, 71]	[63]
E_p (MeV)	σ (mb)						
6	55						
7	108						
8	240		38				
9	290		69	93	21		
10	265	2.7	97	124	37	0.9	
11	317	7.8	122	50	51	2.6	
12	270	10	160	33	39	3.33	
13	282	23	163	33	45	7.67	
14	281	39	130	29	58	13	3
15	217	24	128	34	54	8	16
16	193	34	115	35	46	11.3	40
17	169	34	107	29	41	11.3	64
18	156	27	97	28	33	9	85
19	140	26	92	26	30	8.67	123

Table 4.2: Tabulated cross section data from multiple articles. All of the values are integrated cross section and do not contain angular dependency information. These cross section data were used to calculated the theoretical yields for 2.74, 4.44, 6.13, 6.92, 7.12, and 8.88 gamma and also for in-situ proton energy measurement.

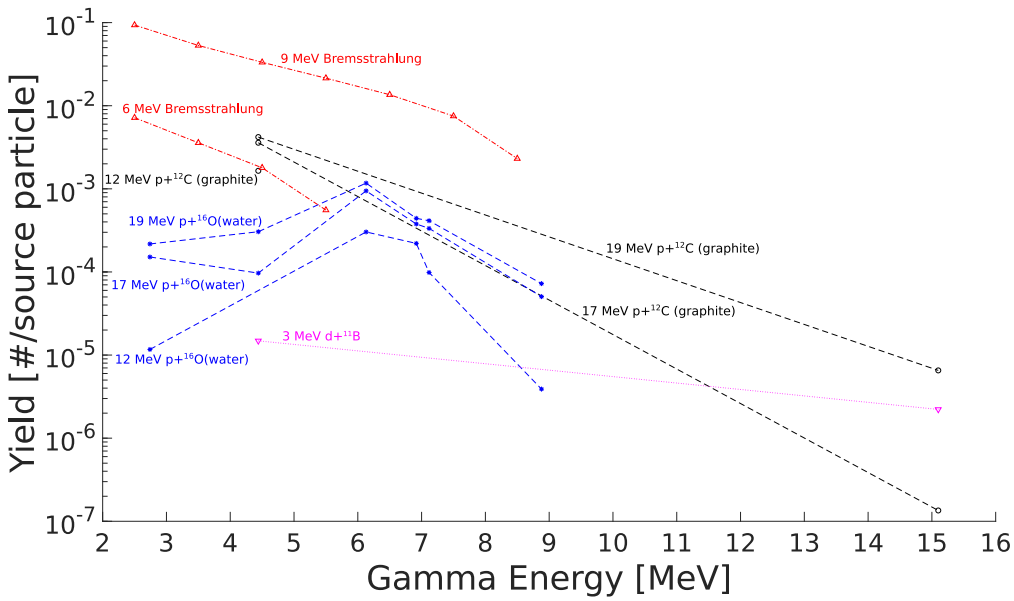

Figure 4-6: Gamma yield from different $(p, p'\gamma)$ calculated using Eq. 4.4 for protons at different energies. The symbols represent the calculated gamma yields, and the dotted lines are for visual discrimination only. The magenta line represents the reaction used for the previous RFQ-based system. The black and blue lines represent reactions of protons on graphite and water respectively. The red symbols represent the yield from bremsstrahlung, and were calculated by binning the simulated bremsstrahlung spectrum into 1 MeV bins (e.g. the 5.5 MeV symbol is total the yield of 5-6 MeV gammas). Simulated bremsstrahlung spectra were generated from the GEANT4 simulation of electrons at the indicated end point energy with a 1 cm thick tungsten target. For conversion, a 1 μA proton beam corresponds to 6.242×10^{12} protons per second.

Reaction	$^{11}B(d,n'\gamma)^{12}C$		
Transition	$^{12}C^{*}4.44 \rightarrow$ g.s.	Transition	$^{12}C^{*}15.1 \rightarrow$ g.s.
E_γ (MeV)	4.44	E_γ (MeV)	15.1
Reference	[70]	Reference	[70]
E_d (MeV)	σ (mb)	E_d (MeV)	σ (mb)
1.51	42	1.75	3.14
1.96	36	2	5.65
2.36	29	2.25	8.80
2.77	25	2.5	11.31
3.07	30.5	2.75	12.57
3.47	31	3	15.71
3.77	32	3.5	16.96
4.11	38	4	16.59
4.68	28	4.5	16.34

Table 4.3: Tabulated cross section data for the $^{11}B(d,n'\gamma)^{12}C$ reaction. All of the values are integrated cross sections and do not contain information on angular dependency. These cross section data were used to calculate the theoretical yields for 4.44 and 15.1 MeV gammas from the past RFQ-based system.

4.6 Cyclotron operation

4.6.1 Operating parameters, effects, and routine procedures

The cyclotron is a complicated machine to operate. In order for CHARON to perform optimally, specific procedures must be followed with multiple parameters requiring fine tuning during operations. First and foremost, the filling procedures must be properly followed to ensure complete filling of the water pocket. Multiple early experiments demonstrated large variations on the gamma peak heights from the oxygen gamma lines in the transmission spectra. There were even occasions when no oxygen lines were observed due to the lack of water in the pocket. To completely fill the water pocket with the least amount of air trapped in it, the water target must first be filled outside the cyclotron, then filled again when it is in the cylotron and under vacuum. Prior to the start of the experiment each day, the water pocket needed to be refilled with fresh, deionized water. This served two purposes. First, it lowered the false "ghost" current reading stemming from the conductivity of slightly ionized

water (which is a path to ground in the otherwise electrically isolated target). The small conductivity might stems from the reactions between slightly acidic water in the pocket and the aluminum of the target. With fresh deionized water, the ghost current was reduced from 100s of nA to approximately 25 nA. Second, it reduced the amount of empty vacancy in the water pocket. As the 50 um aluminum window aged over time with usage, it stretched and deformed such that empty space was created. It was essential to fill those spaces up to ensure the protons were fully stopped by the water.

When internal components of CHARON were inadequately cooled in earlier experiments, multiple procedures were in place to increase the cooling power of the dummy Dee, RF cavity, water target, and ion source in order to increase the beam time. Increasing the temperature of the RF cavity of CHARON led to out gassing of internal components and reduction of the beam output and stability. Similarly, the increased temperature of the dummy Dee and ion source had the same effects. If the vacuum of the beam chamber reached 1.2×10^{-4} Torr, the cyclotron RF power would automatically trip to prevent arcing and damaging of internal components. As such, before the experiment, the water target chiller and main water chiller temperature had to be lowered from 15 degree to 5 degree Celsius and 12 degree Celsius respectively to increase the beam time. After the experiment concluded, the temperature was manually reset to 15 degree Celsius to reduce the risk of damage to the electronic components from condensation in the PLC racks.

In order to maintain proper cooling of the RF cavity so the cyclotron can operate continuously without tripping the vacuum, all the water lines needed to be flushed to prevent clogging in the cooling loops of the cyclotron. Flushing was required if the water flow of either one of the two cyclotrons' cooling loops fell below 2 gpm or once a month as part of a preventive measures procedure. The source of clogging originated from the corrosion resulting from mixed metal effects of copper, steel, and aluminum in the cyclotron components and minerals in the cooling water.

The limited life span of the 50 μm thick aluminum window of the water pocket meant routine replacement of the windows were required for every 10-20 hours of

experiment to prevent rupture. When the target was removed from the cyclotron, the beam chamber needed to be filled with nitrogen and then sealed to prevent atmospheric air with water moisture from entering the cavity. This drastically reduced the amount of time needed to pump the beam chamber back down to the recommended operating pressure of 3×10^{-5} Torr. Without hydrogen gas flowing into the ion source, the beam chamber could be pumped down to 3×10^{-5} Torr within 20 mins after the window replacement.

The ion source was capable of operating within a voltage range of 500 to 1800 V and the range of hydrogen gas flow to the ion source was 0.1 to 1 sccm. Currently, only the gas flow from the ion source can be changed and the ion source power supply would be automatically tuned to the necessary voltage to achieve the ion source current set point between 0.1 to 15 mA. Increasing the ion source gas flow at a fixed ion source current comes with pros and cons. With higher gas flow, the ion source voltage would be lowered so less ion source heating would occur. As a result, the beam chamber vacuum pressure increased at a slower rate and the cyclotron could operate longer before it tripped at 1.2×10^{-4}Torr. The drawback of increasing gas flow was that it increased the baseline beam chamber vacuum pressure so there was a smaller buffer between the starting vacuum pressure and the trip pressure. Furthermore, if there was a bad vacuum, then the beam current on target would decrease due to the decrease of acceptance and beam loss during acceleration. It was trial and error to determine the balance of the ion source gas flow at different ion source current settings to achieve the maximum beam current on target. Most of the experiments in this study ran the ion source at 4 to 6 mA and the hydrogen mass flow was 0.5 to 0.6 sccm to achieve approximately 5 to 6 μA and 0.5 to 0.8 μA on water target and graphite collimator jaw respectively. Out of 19 one-hour long experiments, the average current on water and graphite collimator were 6.0 μA and 0.56 μA respectively.

To maximize the current output on the water and the collimator, the RF voltage and frequency also needed to be tuned prior to the start of the experiment. The RF voltage would affect the fraction of the beam that makes it to the target (known as the transmission). With each cycle around the cyclotron, the proton beam be-

comes slightly less focused, and more of the beam is lost before reaching 12 MeV. With increased voltage, accelerating protons would spend less time and less turns in the cyclotron so the current on target would be higher. In the setup at the time, CHARON operated at 17 kV for MMGR experiments, with some beams able to reach the target at as low as 15.5 kV. After a recent upgrade, CHARON is now able to operate at 18 kV with improved efficiency.

RF frequency was another parameter that affected beam output. Changing the RF frequency led to radial focusing and defocusing of the proton beam. In other words, the amount of beam hitting the water pocket assembly and the graphite collimator jaw depended on the RF frequency. With increasing frequency, the current on the water pocket also increased steadily until it reaches a maximum, followed by a region of steep decrease. Under the range of RF conditions, the current on the graphite collimator jaw increased consistently with increasing RF, increasing the most quickly at the range where the water pocket-current decreased. The results of a series of experiments to investigate this effect are shown in Table. 4.4. In the current operation procedure, the experiment would begin with the RF frequency set close to the edge where the current on water was maximized before the steep drop. As the experiment proceeded, the RF cavity would heat up and the frequency needed to manually decrease in 100 Hz steps to compensate the cavity heating while maintaining the same current on the water pocket. With RF cavity heating during the experiment, the beam became less focused radially, leading to a slight current increase on the graphite jaw. This beam defocusing also led to inaccurate current measurements of the water pocket because the measured current was induced by protons stopping in any part of the whole front assembly with the exact stop location unclear. This frequency tuning was required at the start of each experiment as there were occasions when the beam was too focused with no beam hitting the graphite jaw, thus yielding no 4.4 MeV gammas.

The Dee gap between the Dee and dummy Dee were also calibrated through a series of tests to maximize the ion source acceptance. CHARON was designed to accept approximately 4% (15 degrees) of the total beam produced by the ion source,

RF frequency [kHz]	current on water target [uA]	current on graphite collimator [uA]
67357	1.4	0.4
67358	1.4	0.4
67359	1.4	0.5
67360	1.4	0.8
67361	1.3	0.11
67362	1.1	0.13

Table 4.4: Experimental results showing the change of current on the water target and the graphite collimator at different RF frequencies under the same RF voltage (17 kV), ion source current (1 mA), and ion source gas flow (0.5 sccm).

and an increase in the Dee gap would reduce this acceptance and subsequently reduce the current on target. During calibration, the Dee gap manually increased in small steps ($\sim$ 0.05 mm) until the RF voltage was reached and could remain at 17 kV without arcing for 30 mins. This was then set to be the Dee gap corresponding to the maximum current output. For the current tuning, this Dee gap was 1.75 mm.

4.6.2 Interlock

The Vault laboratory has two interlock systems in place: a mechanical interlock system for perimeter safety and an active dose monitoring system for radiation limits. The two interlocked areas where mechanical interlock systems are installed are the vault and the staging utility room. The operator needs to perform a series of manual and visual checks to ensure no unauthorized personnel remains in or enters the restricted area during the operation of CHARON. As for active area dose monitoring, one Ludlum model 133-2 gamma dosimeter and one Ludlum model 42-30H neutron dosimeter are located next to the vault door in the control room. They are controlled by the Ludlum model 375 digital area monitor and represent the dose to the operators of CHARON in the control room. If the dose rates are above 5 mrem/hr for either gamma or neutron, the alarm will sound, indicating a detectable amount of dose is being generated. If the dose is above the cut off limit of 50 mrem/hr, the cyclotron will automatically shut off to ensure operator safety.

4.6.3 Cyclotron cooling time profile

CHARON operates at around 5 K, making it pivotal to consider the cooling time profile of the cyclotron in order to estimate the time needed for initial setup. From April 30th to May 2nd of 2018, temperature of the persistent switch of CHARON was recorded from 266.8 to 4.94 K during the cooldown. The persistent switch temperature is a close representation of the temperature of the magnet. The persistent switch is a piece of superconducting wire across the terminals of the magnet that is resistive when warm. It is usually made with the same material as the superconducting magnet. When the magnet is being charged, the persistent switch will be heated above its critical temperature such that the magnet forms a complete circuit with the magnet power supplier. When the magnet is charged, the persistent switch heater will be turned off and the switch will be cooled and become superconducting. As a result, the energized magnet will be short circuited by the persistent switch and the persistent current will flow for weeks or months in the superconducting loop.

From April 30th to May 2nd of 2018, temperature of the persistent switch representing the magnet temperature of CHARON was recorded during a full cooldown sequence. In this particular cooldown sequence, the cryo vessel had been left at room temperature for too long and accumulated excess water vapor. As a result, it took two days from April 28th to April 30th with several cycles of nitrogen purging and pumping to lower the cryo vessel pressure below 10 mTorr before the cryo compressor could be safely turned on again to start the cooldown sequence. In Fig. 4-7, the temperature of the magnet steadily dropped at a rate of 22.2 K per day before reaching 75 K. After reaching 75 K, the magnet cooled down at a faster rate until it reached 4.9 K in approximately 1,800 mins due to a reduction in heat capacity at low temperatures. There is a 5 K and 75 K horizontal line plotted in the figure to indicate the operating temperature of CHARON and the approximated temperature after the quench of a fully charged magnet. In case facility cooling water is not available or facility power is lost, the magnet will quench and the stored current will be discharged into the built-in heat sink and heat shield of CHARON. The temperature of the magnet will

then increase to approximately 75 K.

The long cooldown period of 10 to 11 days poses a huge hurdle for deployment systems requiring speedy efficiency. However, some precautions and possible solutions to this exist. First, the water chiller can be air cooled instead of water cooled. Air cooled chillers exist with the same power, output, and size from the same company [101]. As such, the cyclotron could be kept cooled during transportation. There may also be measures to prevent quenching of the cyclotron. The exact quenching temperature of the magnet is unknown but it is at approximately 6 to 7 K. In the event that cryo cooling is lost, it takes 30 to 45 mins to reach this temperature and there can be some emergency procedures to mitigate this effect or even prevent the quench.

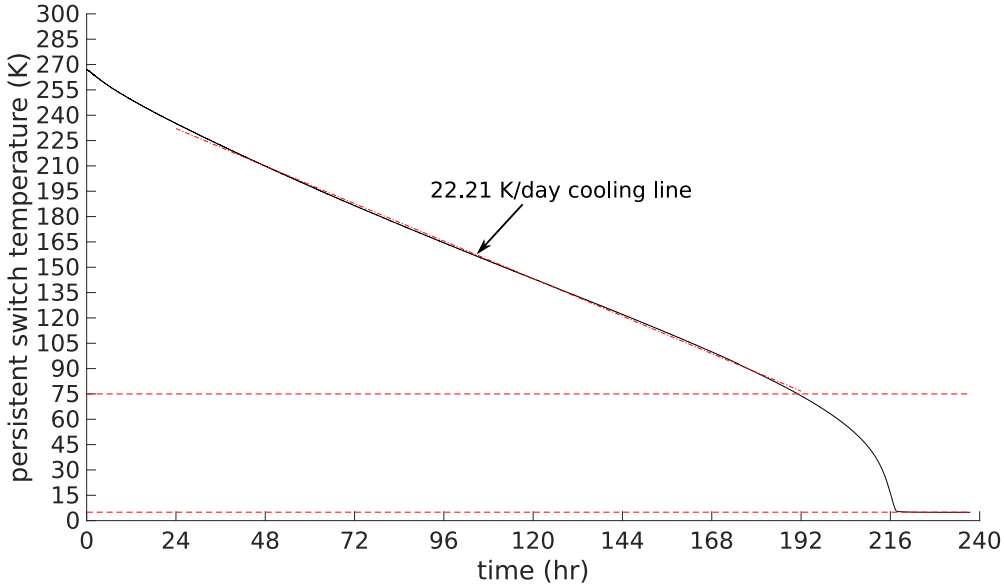

Figure 4-7: Cooling profile of the cyclotron from 266.8 to 4.94 K from the temperature of the persistence switch. Data taken from 266.8 to 263.3 K were recorded in 1 s intervals while data taken from 263.3 to 4.94 K were recorded in 30 s intervals with a total of 36215 entries. The total cooling time was 223.67 hours excluding the pump down time before the cool down. The red dotted lines are the 22.2 K per day cooling line, 5 K, and 75 K line.

4.6.4 Cyclotron magnet ramp up profile

Other than the cooling of the magnet, the ramp up of the magnet was also a time consuming process. CHARON needed to ramp up and charge to 130 A in order to reach the 4.5 T operating magnetic field. During the ramp up, the magnet might heat up slightly so the process needed to be performed slowly to prevent quenching. Fig. 4-8 includes both the persistent switch temperature and the magnet power supply current during a ramp up in Oct 17^{th}, 2019. An increase of persistent switch temperature indicated the "connection" between the magnet circuit and the power supply. The magnet rapidly charged to 90 A during the first 130 mins, then the ramp up slowed down as indicated by the decrease of persistent switch temperature. As the risk of quenching increases, the last 40 A of ramping were done in smaller steps as indicated by the bumps of the persistent switch temperature in Fig. 4-8. It took 12 steps and an additional 87 mins to complete the ramp up. The 217 mins ramp up time contributed to the majority of the initial setup time and cannot be further reduced as there are high risks associated with the magnetic field and the possibility of quenching the magnet during the transportation of a fully charged cyclotron.

4.6.5 Cyclotron upgrades and maintenance

The final consideration on using a superconducting cyclotron for MMGR is the reliability and the uptime (time accessible for use) of the system. Since the commission of CHARON in Feb 9^{th} 2017, there have been multiple cyclotron maintenance, repairs, and upgrades performed, resulting in a large amount downtime. Appendix A lists all the important events related to CHARON. Out of the 126 weeks since the installation up until Oct 1^{st} 2019, there was a total of 43 weeks in which CHARON was down, including 29 weeks due to cyclotron related issues and 14 weeks due to facility related issues. This consists of more than 34% of total time since commission. This demonstrates the unreliability of a novel machine. However, one can foresee much longer uptime as the development of super conducting cyclotron continues to mature. As the technology becomes more developed, downtime related to cyclotron

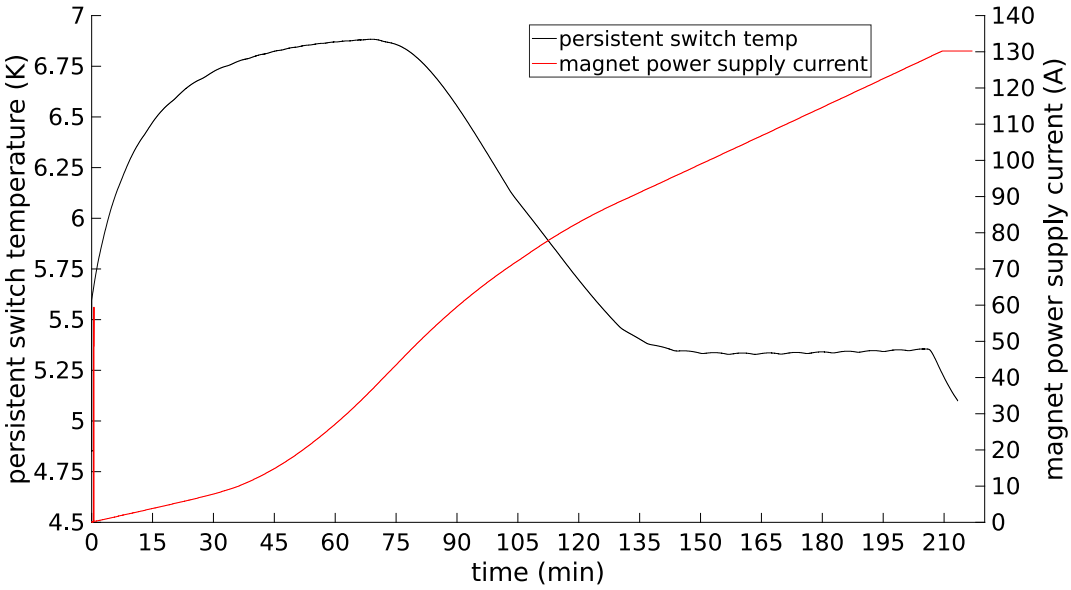

Figure 4-8: Magnet ramping profile of the cyclotron. Data were recorded in 1 s intervals for the whole ramping period. The entirety of the ramping procedure consisted of multiple small steps of ramps indicated by the increasing persistent switch temperature above 5.5 K, which led to the connection of the magnet circuit to the power supply. The total ramping time was 217 mins.

issues should decrease as well. Downtime related to facilities can also be avoided after acquiring data of known existing causes. For example, one could switch the water cooled chiller to air cooled chiller to reduce the reliability on MIT chilled water.

Chapter 5

Experimental Setup and Data Processing for MMGR

This chapter will discuss in details the experimental setup for this PhD thesis. It provides information necessary for individuals to repeat the experiments, including the detector specification, data acquisition system, and floor plan for the entire experimental setup. Data processing methods and techniques are also documented, including background subtraction, energy calibration, and peak fitting perimeters for measuring transmitted counts for each gamma peaks. As mentioned previously, CHARON was originally designed with an internal target for medical isotope production but not MMGR, hence a beam characterization needed to be performed. The results the characterization with an HPGe detector will be discussed in this chapter. Last but not least, all the mock cargoes (homogeneous and heterogeneous) used in this study were tabulated with their corresponding areal density and theoretical Z_{eff}.

5.1 Concept and goals

A few major components make up the experimental setup, including the 12 MeV compact super conducting cyclotron with water target acting as the gamma source, the staging area, and the detector array. Gammas were generated at 4.44, 6.13, 6.92, and 7.12 MeV from (p,p$'\gamma$) reactions on ^{12}C and ^{16}O. For more details on

gamma generation, see Sec. 4.5. The gammas were then collimated by concrete and lead. A block of borated high density polyethylene (HDPE) was also used to reduce the neutron dose. When CHARON got switched on and off, it caused a fair amount of beam variations that leads to beam instability. In order to minimize this impact, mock cargoes were positioned on a standing table in the staging area such that multiple measurements could be taken without switching CHARON on and off. In the detector array, two $LaBr_3$ detectors were used, with one measuring the on-axis transmission spectrum and one located off-axis to acquire unattenuated gamma spectrum for normalization purposes since CHARON developed large beam stability variations at the time.

5.2 Experimental layout

Fig. 5-1 shows a schematic of the experimental setup. CHARON first accelerated the protons to approximately 12 MeV in circular orbits. The protons then hit the internal target assembly, placed at the radius of 14 cm relative to the center of the cyclotron. At the target, the proton beam got collimated by the graphite collimator jaw in the internal target assembly. The collimated beam then hit a 50 μm aluminum window, followed by a static pocket of water. About one tenth of the beam was stopped in the graphite collimator compared to the water target. Although all the gammas generated via (p,p$'\gamma$) reactions were assumed to be isotropic, there were angular dependence on the gamma production cross sections. The gamma yields between different angles for some gammas can differ by more than a factor of two, due to the angular dependence as discussed in Sec. 4.5. The 5 cm steel wall of the cyclotron then collimated the gammas through an 8.9 cm by 12.7 cm opening at 63.8 cm from the front of the water target. In order to minimize neutron activation and background radiation in the detector room (staging area), a block of 20.6 cm thick borated high density polyethylene (HDPE) was placed in the Vault 150 cm away from the source to reduce the number of neutrons transmitted to the staging area. The gammas immediately got collimated through a large 10.2 cm by 81.3 cm high

density concrete opening. At 251.8 cm from the target, the gammas were further collimated by 20.3 cm of lead to a 5.1 cm by 20.3 cm beam in the on-axis direction. The gammas then got transmitted through the interrogated material and measured by detector (Det 1, channel 1) at a distance of 399 cm away from the target. Another detector (Det 0, channel 0) was positioned 45.7 cm to the side of Det 1, considered equivalent to an angle of 6.54 degree relative to the on-axis direction, and measured gammas not collimated by lead nor attenuated by the mock cargo.

The interrogated materials were placed on a standing desk with its height ad-

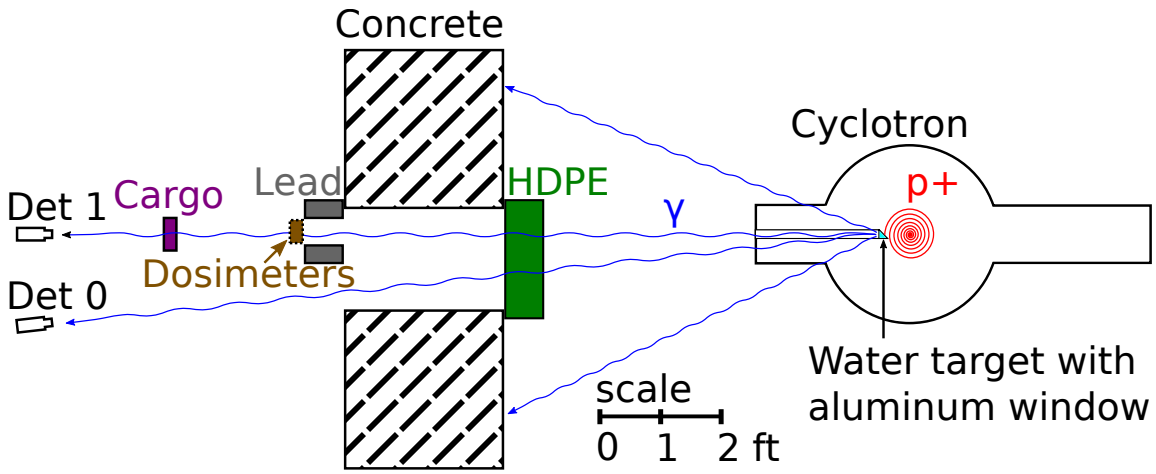

Figure 5-1: Top view schematic of the MMGR experiment. All the objects on the right of the concrete were in a heavily shielded vault while everything on the left were in a less shielded detector room. The dosimeters were only placed in the marked location during the dose measurement experiments.

justable during the experiment. Each scan begun with 5 mins of open air measurements and subsequently 60 mins of transmission measurements of a mock cargo. For the result presented in the thesis, all the 60 min experimental transmission data were divided by the time/order of the recorded events into 10 data subsets for reconstructions. During the experiment, the cargo was lowered into the collimated gamma beam without stopping CHARON to prevent switching it on and off. This was important since the proton beam from CHARON was unstable when it was first switched on. For the same reason, each of the first 5 mins open air measurements were acquired 5 mins after CHARON was switched on, to let CHARON and the proton beam condition to stabilize. If the beam condition was stable after the first MMGR measurement,

another 5 mins plus 60 mins measurement would be made without stopping the cyclotron. With the current space of the staging area, a maximum of 3 different mock cargoes could be place for one continuous scan.

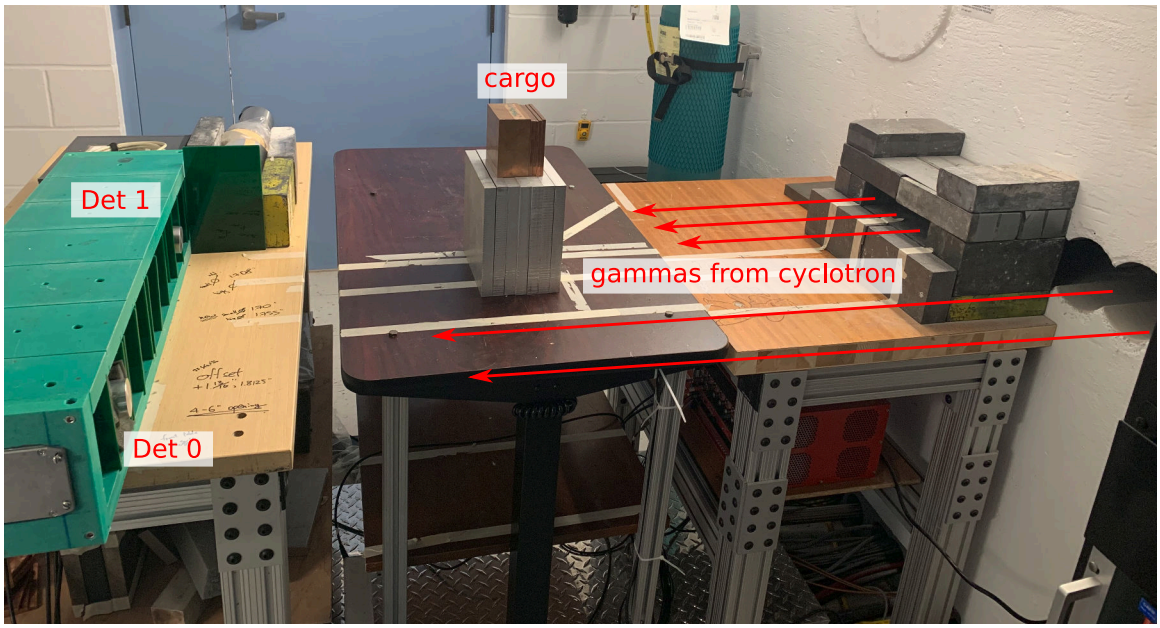

Figure 5-2: Side view of the staging area of the screening experiment. Two different mock cargoes were set up for a continuous run.

5.3 Data Acquisition

5.3.1 Detector discussion

Both detectors used to measure the transmission spectra consisted of a 3.81 cm $\times$ 3.81 cm cylindrical $LaBr_3$(Ce) scintillator, allowing for a high energy resolution of $\sim$3.2% (FWHM) at 661 keV and fast processing (0.016 μs primary decay time) of gamma measurements in the energies of interest. This provided the needed energy precision for material discrimination [102, 103]. Detector 0 was assembled by Saint-Gobain while detector 1 was assembled by Canberra Industries. The time integration windows for the detector signals were set to 0.34 μs, allowing for full capture of the digitized signal from the $LaBr_3$ detector, including all necessary signal processing time. Both detectors with photomultiplier tubes were driven by a positive high voltage

of 750 V to allow the full energy range of gamma detection up to approximately 9.5 MeV.

5.3.2 Electronics and Data acquisition

The two $LaBr_3$(Ce) scintillator detector with photomultiplier tubes were driven by a positive high voltage of 750 V, supplied by the CAEN V6534M VME high voltage board. At 750 V, the current used for detector 0 and detector 1 were 94 and 58 μA respectively. From previous experiments, the detector bases manufactured by ScintiTech have serious gain shifting issues affected by the counting rate, ambient temperature, and the length of operations, leading to detector instability. To rectify this, the bases used in all experiments in this PhD thesis were the Saint-Gobain model AS20 for detector 0 and the Ludlum Model 417-3 high count rate Zener PMT base for detector 1. The Ludlum PMT base was a 10 stages standard 14pin socketed tube base with two Zener stabilized dynodes to allow high rate and stable data acquisition. The gain shift in the current setup was less than 2% .

The detector pulses from the $LaBr_3$(Ce) scintillator were digitized and processed using CAEN V1725 VME waveform digitizer operating in digital pulse processing pulse shape discrimination (DPP-PSD) mode [104]. All the pulse data were recorded and saved in a time-stamped list mode to allow high data transmission rates and throughput performances. The sampling rate of the V1725 digitizer was 4 ns and has 14-bit resolution in ADC unit.

Both of the V6534M VME high voltage board and V1725 VME waveform digitizer were powered by the VME 8008B 8 Slot VME64 mini crate with a 48 cm by 4 U enclosure. It was very compact and can be easily transported. Along with the V1718 VME-USB2.0 bridge, the data transferred at a rate up to 30 MB/s. All detector electronics were controlled using the ADAQ (AIMS Data AcQuisition) framework, producing data files for subsequent analysis [105]. The waveform digitizer with ADAQ recorded the timing and energy information of each detection pulse to form a transmitted energy spectrum. For both detectors, the energy trigger threshold were set to approximately 0.6 to 0.7 MeV, filtering the majority of low energy background counts

and the 511 keV signals. The time integration windows were set at 0.34 μs, allowing full capture of the detector signal from the $LaBr_3$ detector.

The detailed signal processing setting for V1725 digitizer were as follows: DC offset was at 0x1B00 (hex) ADC units and the pulses were in negative polarity, the Q sensitivity of the signals was 40 fC/LSB, and the record length was 85 samples with 15 samples baseline, 16 samples short gate, 50 samples long gate, 30 samples pre-trigger, and 10 samples gate offset. For trigger setting, the trigger threshold was 400 ADC with 50 validation samples.

5.4 Energy spectra from HPGe for beam characterization

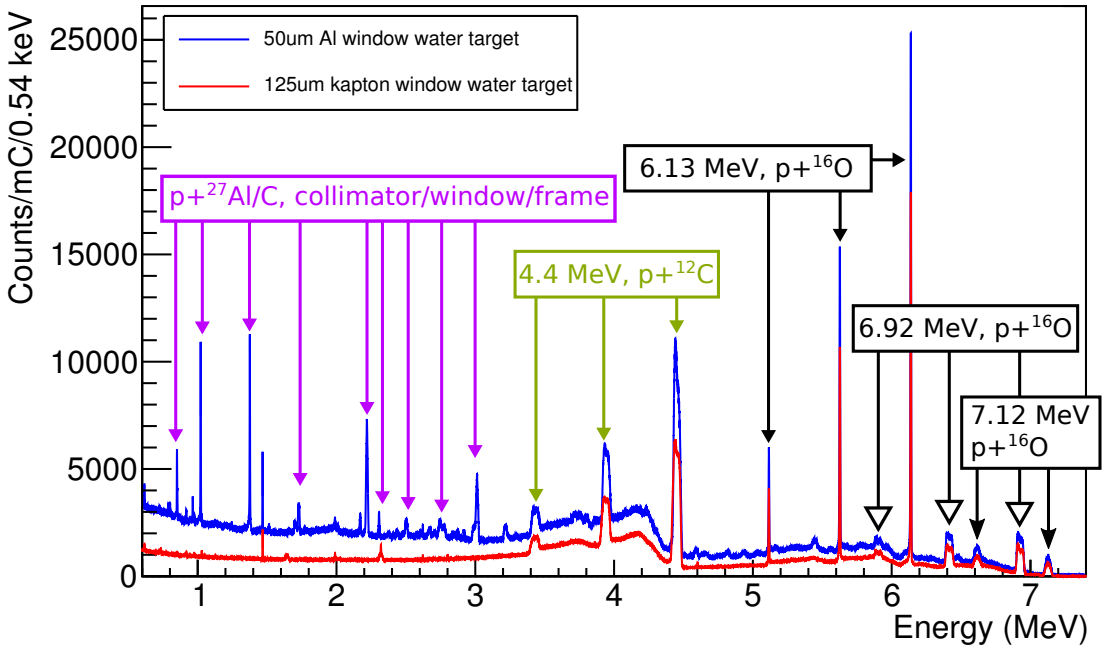

Figure 5-3: Open air gamma spectra acquired by an HPGe detector for two different target setups: water target with 50 μm aluminum window and water target with 125 μm kapton window

The first experiment performed in this PhD study was characterizing the gamma spectrum generated by CHARON. Two HPGe spectra were acquired on May 3rd and

May 10th, 2018 by an HPGe detector on two experimental target setups: one from a 50 μm thick aluminum window with water while the other was a 125 μm thick kapton window with water. In both spectra, the 4.44 MeV gammas and the two escape peaks from $^{12}\mathrm{C}(\mathrm{p},\mathrm{p}'\gamma)^{12}\mathrm{C}$ reaction on graphite, as well as the 6.13, 6.92 and 7.12 MeV gammas and their escape peaks from $^{16}\mathrm{O}(\mathrm{p},\mathrm{p}'\gamma)^{16}\mathrm{O}$ reaction on water were observed. Upon closer inspection, there was a broader double escape peak from 7.12 MeV gammas at approximately 6.10 MeV, slightly to the left of the sharp 6.13 MeV peaks.

The two gamma spectra were significantly different from each other as the aluminum window spectrum has a much higher background and more gamma peaks. The potential cause of the the high background may be due to photons generated from neutron activation in which the neutrons were generated from the protons on aluminum reactions. From the $^{27}\mathrm{Al}(\mathrm{p},\mathrm{p}'\gamma)^{27}\mathrm{Al}$ reaction, multiple high energy gammas above 3.5 MeV can be generated and contributed to some of the very small peaks at about 3.5 MeV [106]. The last potential background was through proton induced bremsstrahlung on aluminum and water; for more details, a study on $^{12}\mathrm{C}(\mathrm{p},\mathrm{p}'\gamma)^{12}\mathrm{C}$ yield measurements with mentions of bremsstrahlung from proton on aluminum was conducted by Nattress et al. [107].

Using the NuDat 2 database, information on nuclear structure such as nuclear level properties and decay data can be searched for and extracted interactively [106]. From this, origins of multiple peaks found exclusively on the aluminum window spectrum were identified: the 1.37 and 2.75 MeV gamma from $^{27}\mathrm{Al}(\mathrm{p},\alpha'\gamma)^{24}\mathrm{Mg}$ reaction and 0.843, 1.014, 1.720, 2.212, 2.734, and 3.004 MeV gamma from $^{27}\mathrm{Al}(\mathrm{p},\mathrm{p}'\gamma)^{27}\mathrm{Al}$ reaction. This result indicated the 2.2 MeV gammas did not originate from the $^{1}\mathrm{H}(\mathrm{n},\gamma)^{2}\mathrm{H}$ reaction on the HDPE. There was also a common gamma peak from both gamma spectra which was the 2.32 MeV peaks from $^{13}\mathrm{C}(\mathrm{p},\gamma)^{14}\mathrm{N}$ reaction.

Another artifact observed in the HPGe spectra were the broadening of gamma peaks from gammas emitted by deexcitation of excited nuclei via $(\mathrm{p},\mathrm{p}'\gamma)$ reactions. Should these nuclear reactions occur on a light target nuclei, then the target nuclei usually carries a considerable amount of kinetic energy after the excitation. If the

mean lifetime of the excited nucleus is shorter than the stopping time of the nucleus in the target medium, the recoiled nucleus may not fully stop prior to deexcitation. As a result, the energy of the gamma radiation will differ from the energy emitted if the nucleus was at rest, leading to a broadened gamma peak. This phenomenon is called a Doppler energy shift [108]. This coherent Doppler effect can also resulted in double-peaking effects if the photons were release at an angle close to 90 degree with respect to the recoil direction. A detailed explanation of this phenomenon can be found in Janout et al. [108] and Kolata et al. [109]. Doppler effects can only be observed if the maximum Doppler shift is much greater than the resolution of the detector and if the lifetime of the excited state is much less than the stopping time of the recoil in the target [109]. As mentioned in Kolata et al. [109]., for a solid target of light nuclei ($A \leq 40$) with incident protons of energy less than 50 MeV, the lifetime of the state needs to be on the order of 10^{-13}s or less in order to observe the Doppler broadening [109]. Devons et al. [110] mentioned the 4.44 MeV state of ^{12}C has a mean lifetime of $2.6 \pm 0.9 \times 10^{-14}$s, hence there should be Doppler broadening. Using the NuDat 2 database, the 6.13, 6.92, and 7.12 MeV state of ^{16}O has a mean lifetime of $2.65 \pm 0.07 \times 10^{-11}$s, $6.78 \pm 0.19 \times 10^{-15}$s, and $1.20 \pm 0.07 \times 10^{-14}$s, hence there should be Doppler broadening on all peaks except the 6.13 MeV peaks and its escapes. The observed gamma spectra shows close agreements as the Doppler broadening were observed on the 4.44, 6.92, and 7.12 MeV gamma peaks and their escapes but not on the 6.13 MeV peaks and its escapes. The FWHM of the broadened 4.44, 6.92, and 7.12 gamma peaks were approximately 50, 50, and 42 keV respectively, while the narrow peak of 6.13 MeV had a FWHM of only 6 keV. Upon closer inspection, the broadened peaks also have double peak features and they are asymmetric with the left peak slightly higher than the right peak. The peak shape is similar to the gamma spectrum with the angle of observation at 70 to 80 degree relative to the beam direction mentioned in Kolata et al. [109].

5.5 Data processing

For each 60 mins experiments, the transmission data was divided into 10 data subsets by the time/order of the recorded events into 10 data subsets (e.g., if there are a total of 10 million events registered and recorded by the detector, the first million events recorded will be used as the first data subset, event 1 million and 1 to 2 million will be used as the second data subset, etc.). All transmission data recorded (the 5 mins open air measurement, and each of the ten equally divided transmission data subset from each of the 60 mins experiments) then underwent the same data processing procedures. Both $LaBr_3$ spectra from channel 0 (ch0) and channel 1 (ch1) underwent energy calibration, background subtraction, and peak fitting prior to the analysis for each of the peak counts. Details on each of the procedures will be explained in the following subsection.

5.5.1 Background subtraction

One vital step in spectral analysis is background subtraction. Gamma spectra processed in this study underwent background subtraction for different peaks before and after energy calibration. Prior to calibration, background subtraction was required to facilitate gamma peaks identification and Gaussian fitting. After calibration, background subtraction was required such that only counts in the gamma peaks were registered and recorded. All the Compton background and gamma background from bremsstrahlung, neutron activation, and proton interaction with the cyclotron's internal material were subtracted.

Each of the transmitted energy spectra collected were analyzed using ROOT, a data analysis library developed by CERN [111]. The background fitting was accomplished using the ShowBackground() fitting function in TSpectrum class. This ShowBackground() fitting function was based on the Background() fitting method in the TSpectrum class and it used the Sensitive Nonlinear Iterative Peak (SNIP) clipping algorithm to calculate the background spectrum [112, 113]. For details about the

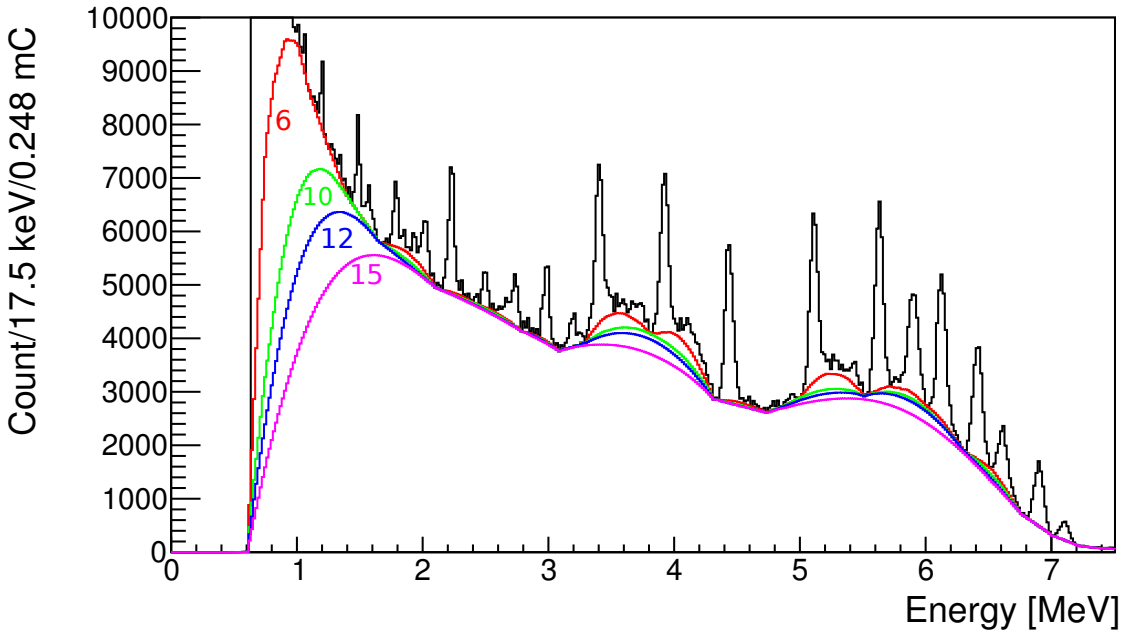

Figure 5-4: Transmission gamma spectra obtained by the off-axis (ch0) $LaBr_3$ detector with different background fitting. The number next to the curve indicate the maximal width of clipping window (number of iterations) used for the background fitting parameters in the Sensitive Nonlinear Iterative Peak (SNIP) clipping algorithm.

algorithm, see Ryan et al. [114] and Morhac et al. [115]. There were a few important input parameters for the background fitting. The first parameter was the maximal width of clipping window (number of iterations). In the analysis, the number of iterations varied between 6 and 15, depending on the peaks of interest. As the number of iterations increased, the background fit became smoother, lower, and cutting less into the gamma peaks as shown in Fig. 5-4 and 5-5. Other than the number of iterations, no additional smoothing was performed. The goal of using different numbers of iterations for each individual gamma peaks was to remove as much background counts as possible without reducing the actual peak counts. Since the general peak locations, peak widths of the gamma peaks, and the shape profile of gamma spectra from different experimental measurements were similar, the number of iterations used for each individual peaks and each detector channel remained the same between all experiments. However, each peak used a different number of iterations and the optimal number of iterations were found by visual inspection. Fig. 5-4 and 5-5 shows the background fitting with different number of iterations plotted on top of the trans-

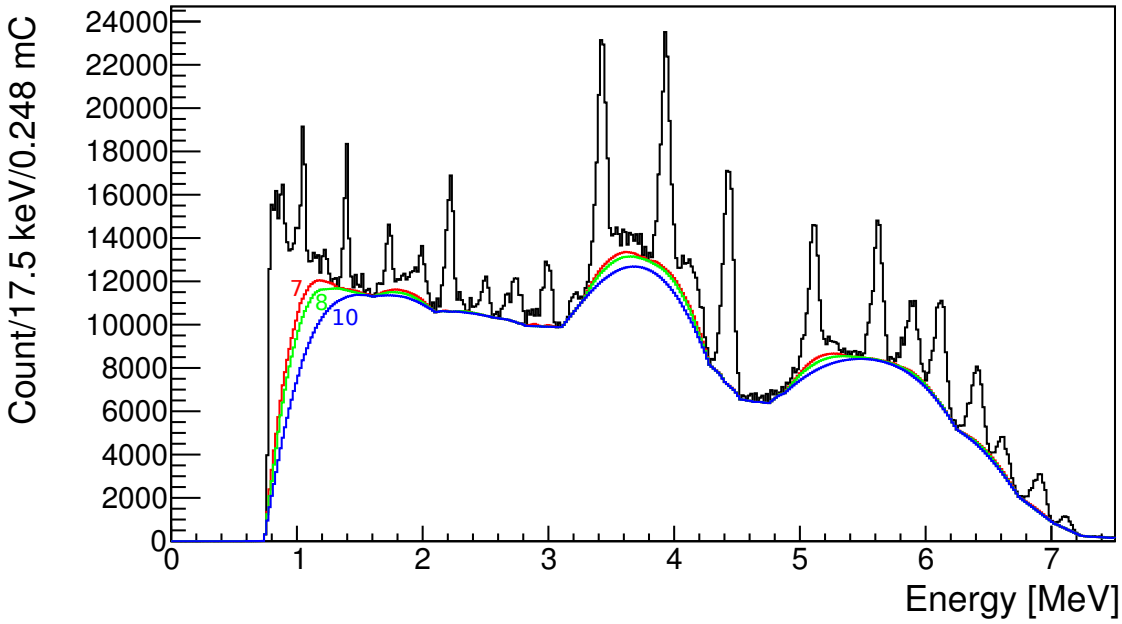

Figure 5-5: Transmission gamma spectra obtained by the on-axis (ch1) $LaBr_3$ detector with different background fitting. The number next to the curve indicate the maximal width of clipping window (number of iterations) used for the background fitting parameters in the Sensitive Nonlinear Iterative Peak (SNIP) clipping algorithm.

mitted gamma spectra for calibrated gamma spectrum from channel 0 and channel 1. The number of iterations used for different gamma peaks are tabulated in Table. 5.1. After the background spectrum were calculated using the method described above, the background spectrum was subtracted from the original transmission spectrum. Fig. 5-6 and 5-7 shows the background subtracted gamma spectra have more isolated and prominent gammas peaks for peak fitting to record the transmitted counts for analysis.

5.5.2 Energy calibration

Each transmission spectra were also calibrated in order to convert the recorded gamma energy in ADC (analog to digital) unit to MeV. First, the 2.21, 3.00, 3.42, 3.93, 4.44, 5.11, 5.62, 6.41, 6.61, 6.92, and 7.12 MeV gamma peaks were fitted with Gaussian function with three parameters in their corresponding background subtracted gamma spectra using the Fit method under the TFormula class in ROOT. The fit

gamma peak energy	number of iterations for ch0	number of iterations for ch1	lower bound for ch0 peak fitting [ADC/MeV]	upper bound for ch0 peak fitting [ADC/MeV]	lower bound for ch1 peak fitting [ADC/MeV]	upper bound for ch1 peak fitting for [ADC/MeV]
2.212	15	10	5400/2.082	5800/2.342	3350/2.082	3650/2.342
3.003	15	10	7400/2.873	7800/3.133	4550/2.873	4850/3.133
3.416	10	7	8300/3.286	8800/3.546	5200/3.286	5500/3.546
3.927	10	7	9500/3.797	10000/4.057	5900/3.797	6200/4.057
4.438	10	8	10700/4.308	11100/4.568	6600/4.308	6950/4.568
5.108	6	8	12100/4.978	12500/5.238	7600/4.978	7900/5.238
5.619	6	8	13100/5.489	13500/5.749	8200/5.489	8600/5.749
5.895	6	8	13600/5.765	14050/6.025	8600/5.765	8950/6.025
6.130	10	8	14050/6.000	14500/6.260	8950/6.000	9250/6.260
6.406	12	10	14500/6.276	14950/6.536	9300/6.276	9650/6.536
6.605	12	10	14950/6.475	15300/6.735	9650/6.475	9900/6.735
6.917	12	10	15400/6.787	15850/7.047	9950/6.787	10250/7.047
7.116	12	10	15850/6.987	16150/7.247	10300/6.987	10550/7.247

Table 5.1: Parameters used for the experimental spectral analysis, including the number of iterations used in background fitting, lower bound and upper bound for peak fitting, for both uncalibrated and calibrated spectra, both detectors, and each gamma peaks.

minimization algorithm used in the Fit method was based on the Minuit package originally written in FORTRAN and converted into C++ [116]. Since both detectors had minimal gain shift (≈50 ADC), the ADC boundaries used for each peak fitting were fixed and listed in Table. 5.1. After the peaks were fitted, the center of the Gaussian fit in ADC units of each of the gamma peaks were recorded. All the recorded peak centers in ADC units along with the peak energies in MeV were fitted with a quadratic equation using the TFormula class in ROOT for energy calibration. Fig. 5-6 shows the graphical results of Gaussian peak fitting for each of the gammas peaks for calibration in one of the data subsets.

5.5.3 Peak fitting and Counts

After calibration and background subtraction, seven peaks were fitted with a Gaussian function at 3.42, 3.93, 4.44, 5.11, 5.62, 6.41, and 7.12 MeV in the corresponding background subtracted calibrated spectra as shown in Fig. 5-7. Table. 5.1 lists the boundaries used for the peak fitting, at approximately 0.13 MeV above and

below the theoretical gamma peak energies. The background subtracted counts at 3.42, 3.93, 4.44, 5.11, and 5.62 peaks were recorded by tallying the background subtracted counts within two standard deviations from the mean of the Gaussian fitted peaks. The 3.42, 3.93, and 4.44 MeV counts, which consisted of the 4.44 MeV gammas and their escape peaks were summed to use as the 4.44 MeV counts. Only the escape peaks at 5.11 and 5.62 MeV were included for the 6.13 MeV counts since the 6.13 MeV peak consisted of both 6.13 MeV peak and 7.12 MeV double escape peaks, and there was no consistent method to analyze their contribution individually. The last gamma counts recorded was the 7.02 MeV counts which was the summation of non-background subtracted counts from two standard deviations below 6.41 MeV to two standard deviations above 7.12 MeV. These gammas originated from the 6.92 and 7.12 MeV gammas, including the first escapes. Due to the negligible high energy gamma background in this region and how close the two energies were to one another, this non-background subtracted integrated count was used as 7.02 MeV counts for the subsequent analysis.

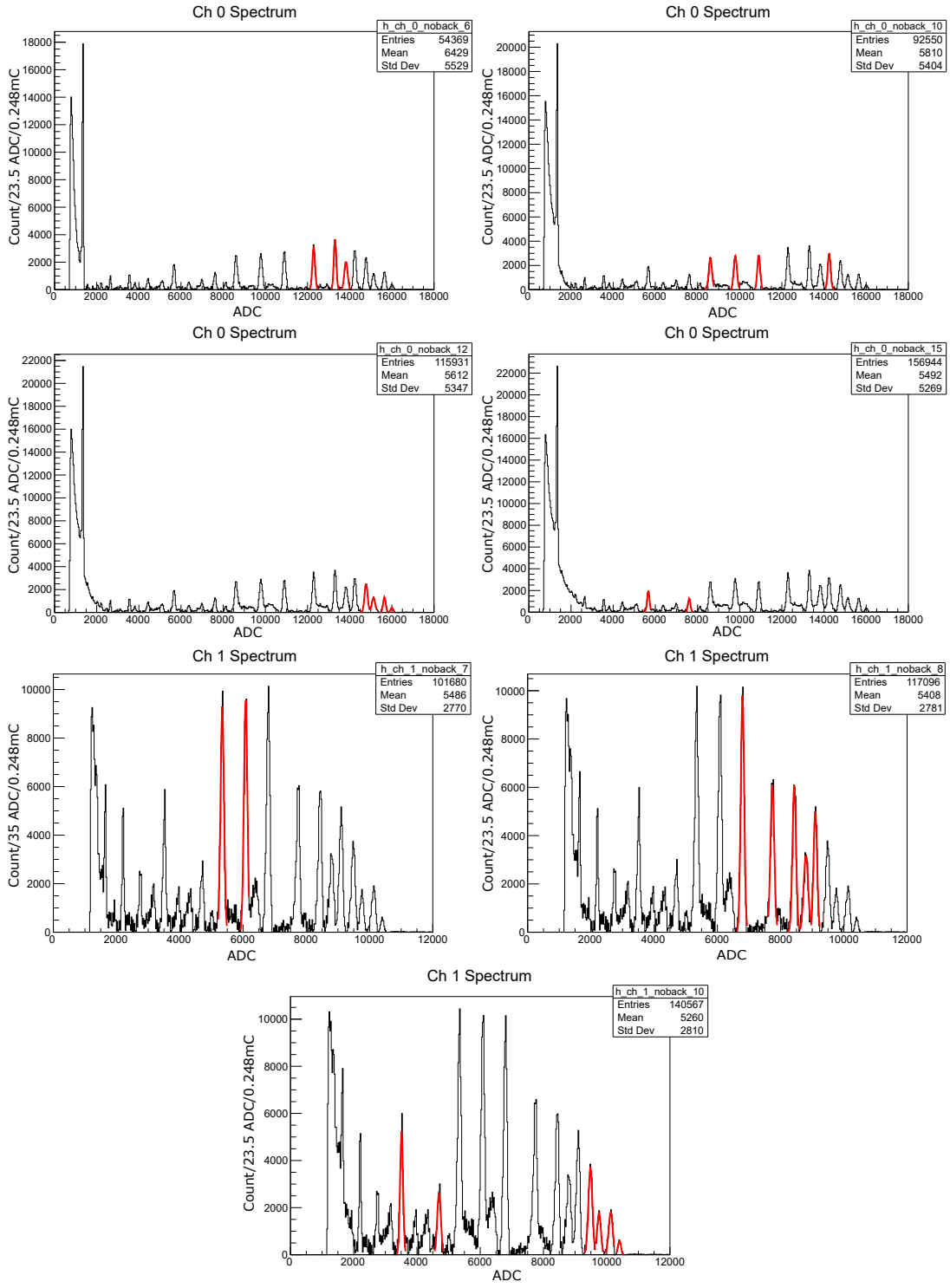

Figure 5-6: Background subtracted gamma spectra showing different Gaussian peak fittings used to locate the center of different gamma peaks on the uncalibrated transmission spectrum at different background subtraction settings. The top four spectra are from channel 0 while the bottom three spectra are from channel 1.

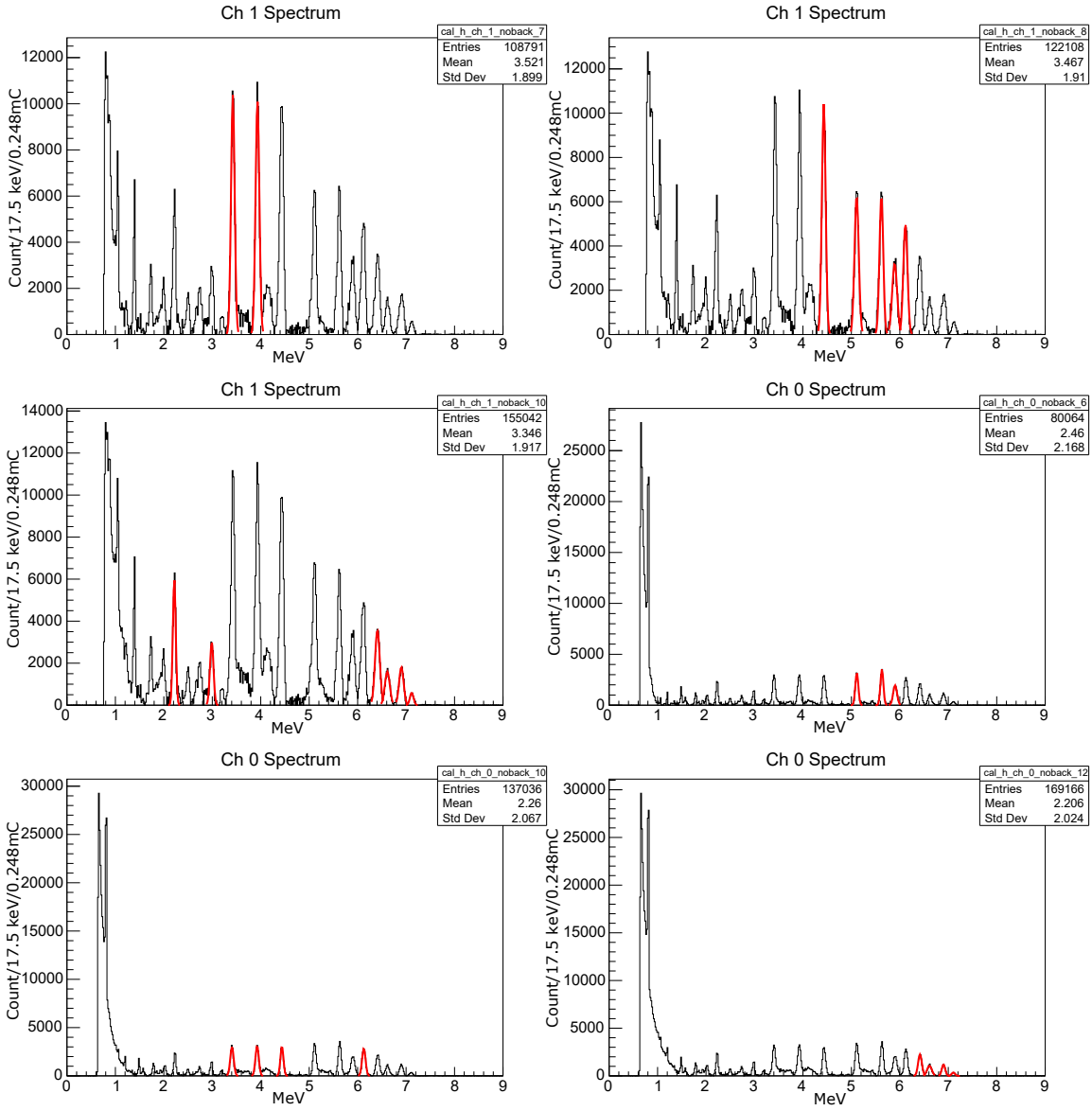

Figure 5-7: Background subtracted gamma spectra showing the Gaussian fitted peaks to locate the integration boundaries for the calibrated transmission spectrum at different background subtraction settings. The top three spectra are from channel 1 while the bottom three spectra are from channel 1.

5.6 Mock cargoes

5.6.1 Homogeneous cargoes

The first 11 MMGR experiments were conducted on 10 different homogeneous materials including aluminum, iron, copper, tin, lead, and depleted uranium, with some at multiple areal densities. The same uranium material was used in two different experiments. The iron used in the experiment met the ASTM A247 standard, which contained multiple impurities. Other than iron, the cast iron consisted of 2.60 to 3.75 % carbon, 1.80 to 3.00 % silicon, and 0.60 to 0.95 % manganese by weight [117]. These impurities have lower atomic numbers than iron and reduced the theoretical and measured Z_{eff} from MMGR. Theoretical Z_{eff} for iron was calculated using a method that will be discussed in Sec. 6.2. Values of the Z_{eff} and areal density along with depth and density of all homogeneous mock cargoes are tabulated in Table. 5.2.

Material	Z_{eff}	Areal density [g/cm^2]	Depth [cm]	Density [g/cm^3]
Aluminum (Al)	13	59.4	22.00	2.70
Aluminum (Al)	13	113.4	42.00	2.70
Iron (Fe)	$\sim$24	56.0	7.78	7.19
Copper (Cu)	29	48.8	5.44	8.96
Copper (Cu)	29	60.3	6.73	8.96
Copper (Cu)	29	88.9	9.92	8.96
Tin (Sn)	50	49.0	6.70	7.31
Tin (Sn)	50	73.1	10.00	7.31
Lead (Pb)	82	57.6	5.07	11.35
Uranium (U)	92	35.4	1.85	19.10

Table 5.2: Information on the homogeneous mock cargoes used for MMGR experiments. Z_{eff}, areal density, depth and density of each materials are tabulated. Because the cast iron used contained at most 3.75 % carbon, 3.00 % silicon, and 0.95 % manganese by weight, a theoretical Z_{eff} was calculated using a method that will be discussed in Sec. 6.2 and indicated with ($\sim$) in the table

5.6.2 Heterogeneous cargoes

In a realistic screening situation, interrogated cargoes and materials will not be homogeneous. Interrogation gammas will transmit through the walls of the cargo container and one or more cargoes, while the cargoes itself can be a mixture of different materials. To address this effect, eight MMGR experiments were also performed on six different heterogeneous mock cargoes. Three different experiments used the same Sn+Al mock cargo. Each heterogeneous material was composed of two different homogeneous materials placed back to back such that the interrogation gamma beam passed through both materials. The areal density for each constituent of the heterogeneous cargoes and their corresponding Z_{eff} are tabulated in Table. 5.3. The method used to calculate the theoretical Z_{eff} will be discussed in detail in Sec. 6.2. All 19 experiments with homogeneous and heterogeneous cargoes were conducted with average current on water and collimator at 6.0 μA and 0.56 μA respectively.

Material 1 + Material 2	Z_{eff}	Total areal density [g/cm^2]	Areal density 1 [g/cm^2]	Areal density 2 [g/cm^2]
Pb + Al	∼35	61.0	28.8	32.2
Cu + Al	∼21	60.8	28.6	32.2
Pb + Cu	∼47	57.4	28.8	28.6
Pb + Sn	∼63	106.6	57.6	49.0
Cu + Sn	∼39	97.8	48.8	49.0
Sn + Al	∼29	96.1	49.0	47.1

Table 5.3: Information on the heterogeneous mock cargoes used for MMGR experiments. Calculated theoretical Z_{eff} are indicated with (∼). The areal density of the constituent materials are also tabulated for reference.

Chapter 6

MMGR Reconstruction and Experimental Results

This chapter will discuss the experimental results from the author's core PhD works with the first section detailing the reconstruction algorithm of effective atomic number (Z_{eff}) and areal density (x) for the scanned materials using MMGR for all 19 experiments. The calculation for theoretical Z_{eff} will be discussed since eight of the experiments were performed on heterogeneous materials (materials consisting of two pure materials). After a detailed discussion on the reconstruction results, extrapolations and estimations were performed for a deployable system in the future. The limitations of MMGR will also be discussed. This concludes with a penetration study following the ANSI N42.46 standard to provide readers with a rough estimate on the penetrability of the MMGR system.

6.1 Reconstruction algorithm

After obtaining the transmitted counts from the spectra in the three regions of interest (4.4 MeV, 6.13 MeV, and 7.02 MeV), the counts measured by the detector at ch1 (on-axis) was first normalized by counts at ch0 (off-axis) as given in Eq. 6.1 to counteract the instability of the proton beam. This instability originated from the variation in beam focusing, vacuum quality, and temperature of internal parts of the

cyclotron, resulting in variation to the beam position and proton energy, ultimately affecting the production of gammas over time. This first normalization was performed with the following formula:

$$C_n(E) = \frac{C_1(E)}{C_0(E)} \tag{6.1}$$

where $C_0(E)$ and $C_1(E)$ are the recorded counts from ch0 and ch1 respectively, using the spectral processing method mentioned in Sec. 5.5. After normalizing the counts with the off-axis detector, experimental transmission ratios between the mock cargo data and open air data for each energy E were calculated using:

$$R_{exp}(E) = \frac{C_{n,mat}(E)}{C_{n,air}(E)} \tag{6.2}$$

where $C_{n,mat}(E)$ and $C_{n,air}(E)$ are the normalized counts at energy E from one of the 10 transmission data subsets with mock cargo and the 5 mins open air transmission spectrum, respectively. The motivation for this open air peak count normalization was to minimize the effects of the variations in open air spectrum and beam condition between different experiments and/or different days.

From Z of 1 to 100 and areal density (x) of 1 to 150, a table of theoretically calculated attenuation at each combination of Z and x are calculated for each energy E using the following formula:

$$R_{calc}(E, Z, x) = \exp\left(-x \cdot \mu(E, Z)\right) \tag{6.3}$$

where $\mu(E, Z)$ is the mass attenuation ratios at energy E and x obtained from the XCOM, a photon cross section database created by the National Institute of Standard and Technology (NIST) [2]. Three tables were generated for each energy of 4.44, 6.13, and 7.017 MeV. Each cell in the table contained the calculated attenuation at the specific Z and x value. With the computed tables of attenuation and measured transmission ratios at different energies, an objective function similar to χ^2 test was constructed to simultaneously determine the combination of Z and x of the mock cargo material. This objective function listed in Eq. 6.4 consists of two different

parts with σ representing the uncertainty of the quantity in the corresponding square bracket. The first part of the equation used ratios of the transmission ratios (4.44 over 7.017 MeV and 6.13 over 7.017 MeV) to provide better Z discrimination and also to cancel out certain systematic uncertainties. The second part of the equation used the absolute transmission ratio of 7.017 MeV due to a lack of high energy background above 7.2 MeV, which provided better areal density discrimination. See Sec. 6.1.1 for the experimental evidence demonstrating the importance of the absolute transmission ratio. The experimental ratios of transmission ratios and absolute ratios were then compared with the computed attenuation ratio in a similar fashion as the χ^2 test. For each ratio, an optimal set of weights (w_1, w_2, w_3) was used for the best reconstruction performance. Using the above metric, the estimated value of Z_{eff} and x corresponded to minimum F in Eq. 6.4.

$$F = \sum_{i=1}^{2} w_i \left\{ \frac{\frac{R_{exp}(E_i)}{R_{exp}(7.017)} - \frac{R_{calc}(E_i,Z,x)}{R_{calc}(7.017,Z,x)}}{\sigma\left[\frac{R_{exp}(E_i)}{R_{exp}(7.017)} - \frac{R_{calc}(E_i,Z,x)}{R_{calc}(7.017,Z,x)}\right]} \right\}^2 + w_3 \left\{ \frac{R_{exp}(7.017) - R_{calc}(7.017,Z,x)}{\sigma\left[R_{exp}(7.017) - R_{calc}(7.017,Z,x)\right]} \right\}^2 \tag{6.4}$$

where E_1 is 4.44 MeV and E_2 is 6.13 MeV.

6.1.1 Optimization of the weights used in the algorithm

As mentioned in Sec. 5.5, each of the 60 mins experimental transmission data were divided equally into 10 smaller data subsets. For the results presented and plotted in the thesis, transmission data from all 60 mins of the experiment were divided by the time/order of the recorded events into 10 data subsets (e.g., if there are a total of 10 million events registered and recorded by the detector, the first million events recorded will be used as the first data subset, event 1 million and 1 to 2 million will be used as the second data subset, etc.). After dividing the 60 min data equally, date processing mentioned in Sec. 5.5 was performed on each of the spectra. For each data subset, the Z_{eff} and x was found using the method mentioned in Sec. 6.1. In Eq. 6.4,

the three weights (w_1, w_2, w_3) used for the reconstruction were optimized using the following procedure. Different combinations of the three weights in 0.1 increments with a total sum of 1.0 were used for the reconstruction of all 19 experiments. In order to determine the best weights, the total χ^2 values, $\bar{\delta}$, and $\bar{\sigma}$ for the Z_{eff} and x reconstructions were calculated and recorded. Total χ^2_Z is defined as $\sum_{exp=1}^{19}(\delta_{Z,exp}/\sigma_{Z,exp})^2$, where $\delta_{Z,exp}$ is the difference between the average reconstructed Z_{eff} of the 10 data subsets and the theoretical value for each experiment, and $\sigma_{Z,exp}$ is uncertainty of the reconstructed Z_{eff} of the 10 data subsets for each experiment, calculated from the variations of the reconstructed values. $\sigma_{Z,exp}$ and $\delta_{Z,exp}$ represented the reconstruction precision and accuracy of Z_{eff} prediction. The same set of calculations applied for reconstructed x as well. In addition, $\bar{\delta}$ and $\bar{\sigma}$ are the mean δ and σ across all 19 experiments. These calculated values for a selection of different weights were recorded in Table. 6.1.

The reconstruction estimates using best performing weights should have high accuracy followed by high precision, hence the desire for $\bar{\delta}$ and $\bar{\sigma}$. According to Table. 6.1, the weight combinations of 0.2, 0.6, and 0.2 have the best reconstruction accuracy with high precision and were chosen as the optimal weights for the final reconstructions. Another conclusion drawn from the table was the importance of w_3, the weight for the difference between the experimental and theoretical 7.017 MeV absolute transmitted ratio in Eq. 6.4. If the absolute ratios were not used ($w_3 = 0$), both the reconstruction accuracy ($\bar{\delta}$) and precision ($\bar{\sigma}$) increased by approximately 3 times for Z_{eff} and 10 times for x, demonstrating the importance of w_3 for reconstruction accuracy, especially for areal density.

w_1	0.2	0.2	0.2	0.3	0.2	0.3
w_2	0.5	0.6	0.7	0.5	0.8	0.7
w_3	0.3	0.2	0.1	0.2	0	0
χ^2_Z	16.569	15.025	14.048	20.068	30.401	26.589
χ^2_x	25.534	23.307	28.267	25.825	30.940	31.361
$\overline{\delta_Z}$	4.526	4.521	4.516	4.663	11.457	11.316
$\overline{\delta_x}$	3.253	3.185	3.270	3.343	31.775	31.986
$\overline{\sigma_Z}$	6.597	6.863	6.866	6.520	14.231	14.225
$\overline{\sigma_x}$	3.678	3.822	3.678	3.551	49.097	48.852

Table 6.1: Selections of weight combination used for Eq. 6.4 along with the χ^2_Z, χ^2_x, $\bar{\delta_Z}$, $\bar{\delta_x}$, $\bar{\sigma_Z}$, and $\bar{\sigma_x}$ values from the reconstruction using each of the combinations. Total χ^2_Z is defined as $\sum_{exp=1}^{19}(\delta_{Z,exp}/\sigma_{Z,exp})^2$, where $\delta_{Z,exp}$ is the difference between the average reconstructed Z_{eff} from the 10 data subsets and the theoretical value for each experiment, and $\sigma_{Z,exp}$ is the uncertainty (from variance) of the reconstructed Z_{eff} from the 10 data subsets for each experiment. The same set of calculations also applied for the reconstructed x. In addition, $\bar{\delta}$ and $\bar{\sigma}$ are the mean δ and σ across all 19 experiments.

6.2 Effective Z calculation

In a more realistic cargo scenario, the photons would transmit through multiple materials with different Z and x. The theoretical Z_{eff} would lie somewhere between the Z of those materials. In this study, 8 MMGR experiments were performed on six different heterogeneous mock cargoes containing two pure materials. The Z_{eff} of these materials were calculated using the following two steps.

First, the mass attenuation coefficients of the material at each of the gamma energies (4.44, 6.13, and 7.02 MeV) were weighted by the mass fraction of individual material using Eq. 6.5, where W_i is the mass fraction of material i in the mixture and $\mu_i(E)$ is the mass attenuation coefficient of material i at energy E found in the XCOM database created by NIST [2].

$$\mu(E) = W_1 \cdot \mu_1(E) + W_2 \cdot \mu_2(E) \tag{6.5}$$

The calculated $\mu(E)$ values of the mixture were then used in Eq. 6.6 to estimate the theoretical effective Z_{eff} for the heterogeneous material. In the formula, the attenuation using the three calculated $\mu(E)$ were compared with the μ_{nist} from the XCOM database at different single Z values in a similar fashion as the reconstruction Eq. 6.4. The Z value from a single material with the best matching gamma attenuation were then used as the theoretical Z_{eff} for the specific heterogeneous material.

$$\begin{aligned} Z_{\text{eff}} = \arg\min_{Z} \Bigg\{ & w_1 \left(\frac{\exp(-x \cdot \mu(4.44MeV)}{\exp(-x \cdot \mu(7.02MeV)} - \frac{\exp(-x \cdot \mu_{nist}(Z, 4.44MeV)}{\exp(-x \cdot \mu_{nist}(Z, 7.02MeV)} \right)^2 \\ & + w_2 \left(\frac{\exp(-x \cdot \mu(6.13MeV)}{\exp(-x \cdot \mu(7.02MeV)} - \frac{\exp(-x \cdot \mu_{nist}(Z, 6.13MeV)}{\exp(-x \cdot \mu_{nist}(Z, 7.02MeV)} \right)^2 \\ & + w_3 \left(\exp(-x \cdot \mu(7.02MeV) - \exp(-x \cdot \mu_{nist}(Z, 7.02MeV) \right)^2 \Bigg\} \end{aligned} \quad (6.6)$$

where $\mu(E_i)$ is the calculated mass attenuation coefficient at energy E_i using Eq. 6.5, $\mu_{nist}(Z, E)$ is the mass attenuation coefficient from the XCOM database at energy E for material Z, x is the areal density of the mock cargo, and (w_1, w_2, w_3) are the weights used in Eq. 6.4 for the reconstructions.

6.3 Results

6.3.1 Reconstruction example

With the optimal weights of 0.2, 0.6, and 0.2, reconstructed Z_{eff} and x were estimated and recorded using Eq. 6.4. Fig. 6-1 shows the heatmaps of the reconstruction results of two data subsets with mock copper and mock lead cargo in the F space with respect to Z and x. The transmission data used in the first heatmap was from the 9^{th} data subset of the experiment with 48.8 g/cm^2 of copper ($Z = 29$). The reconstructed Z_{eff} and x were 29 and 48 g/cm^2 respectively, with a F value of 0.0182. The transmission data used in the second heatmap was from the 6^{th} data subset of the first experiment using 35.4 g/cm^2 of uranium ($Z = 92$) experiment. The reconstructed Z_{eff} and x were 88 and 38 g/cm^2 respectively, with a F value of 1.7482. In

these two data subsets, the reconstructed values closely matched the actual values of the mock cargo.

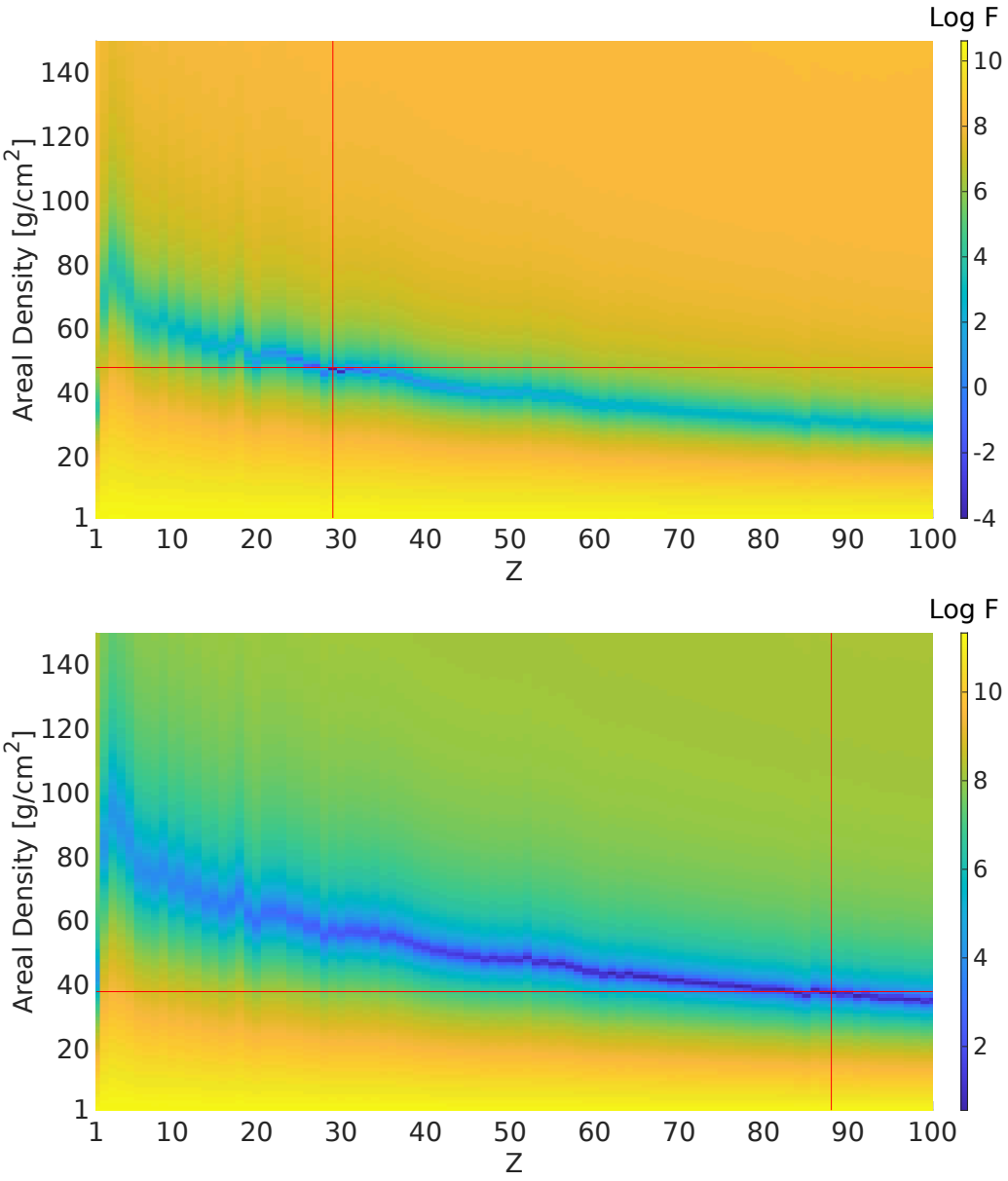

Figure 6-1: Heatmap of the reconstruction objective function F as a function of Z and x in the range of 1-100 and 1-150 g/cm^2, respectively. The data used in the top heatmap was from the 9^{th} data subset of the experiment with 48.8 g/cm^2 of copper ($Z = 29$). The red line indicates the predicted Z_{eff} and x estimation of 29 and 48 g/cm^2 respectively, with a F value of 0.0182. The data used in the bottom heatmap was from the 6^{th} data subset of the first experiment using 35.4 g/cm^2 of uranium ($Z = 92$) experiment. The red line indicate the predicted Z_{eff} and x estimation of 88 and 38 g/cm^2 respectively, with a F value of 1.7482.

6.3.2 Reconstruction results

All 10 data subsets from each of the 19 experiments were processed using the same reconstruction procedures. For the result presented in Figure 6-2, the 60 mins experimental transmission data were divided by the time/order of the recorded events (e.g., if the detector registered and recorded a total of 10 million events, the first million event recorded will be used as the first data subset, event 1 million and 1 to 2 million will be used as the second data subset, etc.). The mean and standard deviation of the 10 reconstructed Z_{eff} and x were computed across the data subsets for each of the experiments. These were compared to actual known values of the mock cargo. The difference between the actual and average reconstructed value of each experiment were also recorded. Figure 6-2 plots the reconstruction results for homogeneous and heterogeneous materials respectively, with the detailed numerical results reported in Table. 6.2. The error bars in Figure 6-2 represent the standard deviation over the reconstructed values of the 10 data subsets for that particular mock cargo experiment. Standard deviation was calculated as the square root of the variance of the 10 reconstructed values for that particular mock cargo experiment. Results for the reconstructed Z_{eff} and x for the data subsets in each of the experiments (19 experiments, each with 10 data subsets) were also plotted in Fig. B-1 and can be found in Appendix B.

As seen in Figure 6-2, the reconstructed values of Z_{eff} and x were very close to the actual values for most of the results and seems to be well within the statistical uncertainty. There is also significant separation between low-Z materials such as aluminum, medium-Z material such as tin, and high-Z material such as lead. Furthermore, there is a distinct separation between materials with different x. The difference in reconstructed Z between lead and uranium are small, however, partially due to the insufficient photon transmission statistics in tests with high-Z materials, especially when x is also high. With all of the reconstruction results, it is possible to compare the reconstructed and actual values of Z_{eff} and x in a χ^2 test, as a way to determine whether the deviations were due to random fluctuations such as counting

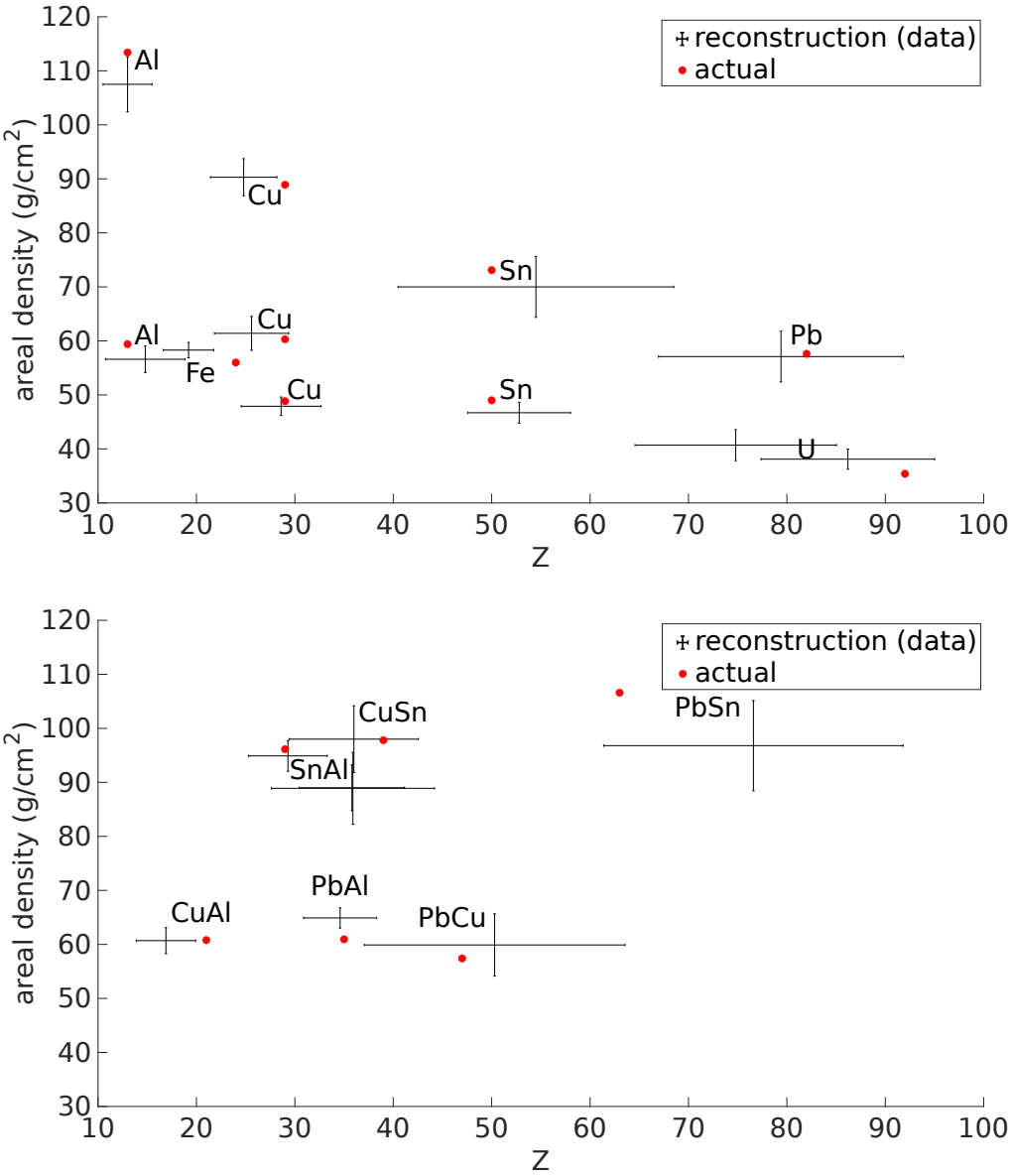

Figure 6-2: Reconstruction results of all homogeneous material (top) and heterogeneous material (bottom) MMGR experiments. Each of the experiments were divided into 10 data subsets by the gammas' recording time (time sequencing). The red dots indicate the actual Z and x value of the materials. The error bars represent the standard deviation over the reconstructed Z_{eff} and x in the data set for a particular mock cargo, centered at the mean of the reconstructed values of the same data set. Two separate experiments were performed on the same depleted uranium mock cargo, and three separate experiments were performed on the same Sn+Al heterogeneous mock cargo.

Material	Actual Z_{eff}	Average Reconstructed Z_{eff}	$\sigma_{Z_{\text{eff}}}$	Actual x (g/cm^2)	Average Reconstructed x (g/cm^2)	σ_x (g/cm^2)
Aluminum 1 (Al)	13	14.8	4.0	59.4	56.6	2.5
Aluminum 2 (Al)	13	13.0	2.5	113.4	107.5	5.1
Iron (Fe)	∼24	19.2	2.6	56.0	58.3	1.4
Copper 1 (Cu)	29	28.6	4.1	48.8	47.9	1.7
Copper 2 (Cu)	29	25.6	3.8	60.3	61.4	3.1
Copper 3 (Cu)	29	24.8	3.4	88.9	90.3	3.4
Tin 1 (Sn)	50	52.8	5.2	49.0	46.7	2.0
Tin 2 (Sn)	50	54.5	14.0	73.1	70.0	5.6
Lead (Pb)	82	79.4	12.4	57.6	57.1	4.7
Uranium (U)	92	86.2	8.8	35.4	38.1	1.9
Uranium (U)	92	74.8	10.2	35.4	40.7	2.9
Pb + Al	∼35	34.6	3.7	61.0	64.9	1.9
Cu + Al	∼21	16.9	3.0	60.8	60.7	2.4
Pb + Cu	∼47	50.3	13.2	57.4	59.9	5.8
Pb + Sn	∼63	76.6	15.2	106.6	96.8	8.4
Cu + Sn	∼39	36.0	6.6	97.8	98.0	6.2
Sn + Al	∼29	35.9	8.3	96.1	88.9	6.7
Sn + Al	∼29	29.3	4.0	96.1	94.9	2.8
Sn + Al	∼29	35.8	5.3	96.1	89.0	4.2

Table 6.2: Average reconstructed Z_{eff} and areal density x for all MMGR experiments with actual values and reconstruction uncertainties listed. Each of the experiments were divided into 10 data subsets by the gammas' recording time (time sequencing). The $\sim$ symbol indicates the actual Z_{eff} value of the heterogeneous cargo calculated using the method as described in Sec. 6.2

Set of experiments	Reduced χ^2_Z	Reduced χ^2_x	$\overline{\delta_Z}$	$\overline{\delta_x}$	$\overline{\sigma_Z}$	$\overline{\sigma_x}$
Homogeneous	0.978	1.188	4.318	2.576	6.456	3.116
Heterogeneous	0.750	1.462	4.800	4.021	7.424	4.793
All	0.835	1.295	4.521	3.185	6.863	3.822

Table 6.3: Values of reduced χ^2, $\overline{\delta}$, which is the average difference between the reconstructed and actual value (representing accuracy), and $\overline{\sigma}$ which is the average standard deviation of the reconstructed values across the data set (representing precision), for three categories of experiments (homogeneous, heterogeneous, and all 19 experiments). Each of the experiments were divided into 10 data subsets by time sequencing (the recorded time of the gammas as mentioned in Sec. 6.1.1).

statistics or some residual, unaccounted-for systematic effect. Using the same definition of total χ^2_Z mentioned in 6.1.1, the total χ^2 of Z_{eff} and x between the average reconstructed values and the actual values for all 19 experiments 15.03 and 23.30, respectively. These correspond to p-values of 0.66 and 0.18 respectively, indicating that the deviations were dominated by random fluctuations, not systematic effects. Numerical values of reduced χ^2, $\overline{\delta}$ (the average difference between the reconstructed and actual value) and $\overline{\sigma}$ (the average standard deviation of the reconstructed values across the data set) for the three categories of experiments (homogeneous, heterogeneous, and all 19 experiments) are listed in Table. 6.3. On average, the reconstructed Z_{eff} and x were 4.52 and 3.19 from the actual values respectively, with a standard deviation (precision) of 6.86 and 3.82. However, as the standard deviation of the reconstructed values were experimental data driven (calculated from the reconstruction values), systematic error such as cyclotron instability may still contribute a large part.

The reconstruction values of the two uranium experiments were analyzed in order to investigate the effects of systematic error. In particular, uranium experiment 2 had a mean reconstructed Z_{eff} of 74.8, well below the expected Z value of 92. Superficially, this appears to just be statistical. As shown in Figure 6-2, all the predictions appear to follow the Gaussian distribution, in which 13 out of 19 (68 %) experiments have the theoretical Z_{eff} within one standard deviation from the mean reconstructed Z_{eff} while all are within two deviations from the mean. However, this only proves the data did follow the Gaussian distribution from the data driven standard deviations but did not provide information regarding the effects of systematic error from the experiments.

As such, further investigation was conducted to determine the outlying data subsets in the two uranium experiments with Z_{eff} more than a standard deviation away from the mean of the predictions (data subset 1 on uranium experiment 1, and data subset 10 on uranium experiment 2). As shown in Fig. 6-3, data subset 1 on uranium experiment 1 predicted Z_{eff} and x at 66 and 43 g/cm^2 respectively, while data subset 10 on uranium experiment 2 predicted Z_{eff} and x at 52 and 48 g/cm^2

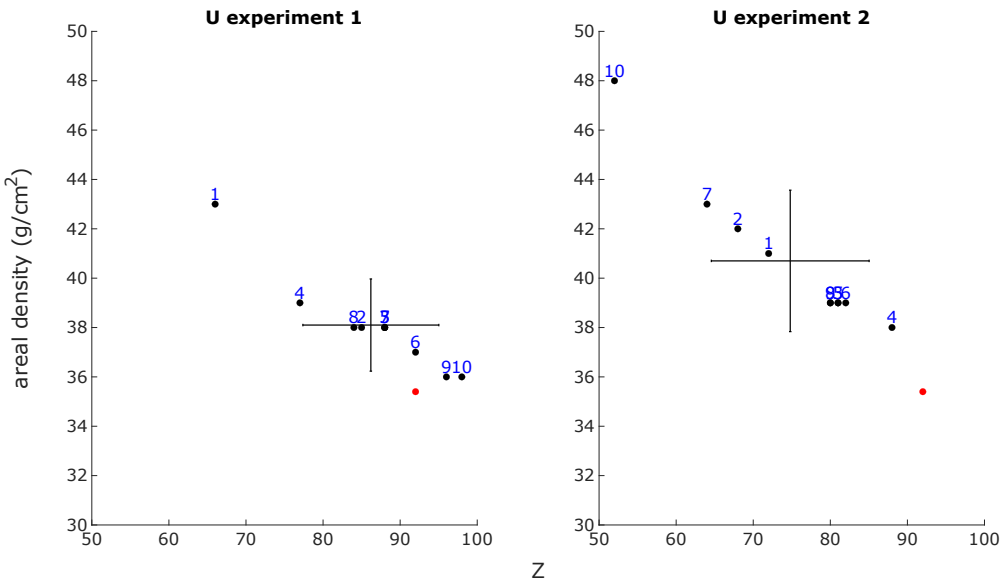

Figure 6-3: Reconstructed Z_{eff} and x for both uranium experiments (experiment 1 on left and experiment 2 on right), with error bars representing the standing deviation calculated from the 10 time sequenced data subsets. The error bars are centered at the mean of the reconstructed values of the same experiment. The red data point indicates the actual Z and x of the mock cargo while the black data point indicates the reconstructed values with the index number of the data subsets labelled on top of the data points.

respectively. These were classified as outliers in the experiment. As the division of the data subset was done using time sequencing methods, these outliers were the first indication of time dependant systematic errors such that the change in gamma production during the experiments were not eliminated by the normalization in the reconstruction procedures.

Multiple analysis were performed on the two uranium experiments with a combination of different methods as follows: 1) remove the outlying portion of the data to observe improvement in prediction performance, 2) reduce the number of data subsets to 5 (each data subset would contain approximately 12 mins of data instead of 6 mins) to observe the effect of increasing counting statistics, 3) use the 5 mins open air measurements after each of the experiments for normalization instead of the open air measurements before the experiments to observe any changes on reconstruction accuracy and precision, and 4) using random sampling instead of time sequenced

sampling to divide the 60 mins experimental data into data subsets.

To divide the data by random sampling instead of the recorded event number, a random seed was generated during the data processing procedure for each of the experiments. For each of the recorded gamma events in the experiment, a random number (between 0 to the number of data subsets) was generated using the same random seed. The gamma event was then assigned to the corresponding data subset using the random number generated. In other words, the data was randomly sampled into multiple portions without replacement. For each experiment, a total of 10 groups of randomly sampled data subsets were created, with each group containing 5 or 10 data subsets. As an example, the data for "Rand. sampl. (10 seeds), w/ outlier (10 subset)" used in Table 6.4 contains 10 groups of 10 randomly sampled data subsets with each group using a different random seed for sampling. For each group in the 10 data subsets, the σ_Z, and σ_x was determined along with the mean reconstructed Z_{eff} and x. The 10 average predicted Z_{eff},x, σ_Z, and σ_x from each of the 10 groups were then averaged to give an overall average Z_{eff}, x, σ_Z, and σ_x. The results of all of the reconstruction results from the two uranium experiments using different combinations of sampling method, outlier filtering, number of data subsets, and the 5 mins open air measurements are tabulated in Table 6.4.

The main motivation to divide the data by random sampling is that any time dependent systematic variations would be distributed into all data subsets. This would yield predictions close to an experiment where the beam varies consistently and uniformly throughout the experiment instead of varying from time to time. If the main source of time dependant systematic variation stems from beam focusing, randomly sampled data will correspond to an experiment in which the beam spot is consistently a little defocused instead of varying between focused and defocused at random time during the experiment. As a result, the systematic error and unstable data was "smeared" so predictions would be more precise in theory. The results in Table. 6.4 confirms the existing systematic time dependant variations for both uranium experiments. The experimental standard deviations of Z_{eff} and x ($\sigma_{Z_{\text{eff}}}$ and σ_x) from predictions using time sequenced data subsets are more than a factor of

U experiment number	1	1	1	1	2	2	2	2
	Z_{eff}	$\sigma_{Z_{\text{eff}}}$	x	σ_x	Z_{eff}	$\sigma_{Z_{\text{eff}}}$	x	σ_x
using 5 mins open air measurement before experiment								
Time seq.								
w/ outlier (10 subset)	86.2	8.8	38.1	1.9	74.8	10.2	40.7	2.9
w/o outlier (9 subset)	88.4	6.0	37.6	1.0	77.3	7.2	39.9	1.6
w/ outlier (5 subset)	84.8	4.4	38.6	0.5	75.4	6.9	40.4	1.7
w/o outlier (5 subset)	77.6	11.3	40.0	2.9	79.2	10.5	39.6	2.4
Rand. sampl. (10 seeds)								
w/ outlier (10 subset)	85.3	3.1	38.6	0.7	83.4	4.9	39	1.1
w/o outlier (9 subset)	85.7	3.7	36.2	0.8	84.5	7.3	36.4	1.6
w/ outlier (5 subset)	84.9	2.5	38.6	0.6	83.7	2.9	39	0.5
w/o outlier (5 subset)	85.5	1.9	36.6	0.6	85.5	4.2	36.1	0.8
using 5 mins open air measurement after experiment								
Time seq.								
w/ outlier (10 subset)	82.8	5.9	38.3	1.2	81.3	4.6	38.8	1.0
w/o outlier (9 subset)	81.8	5.3	38.4	1.2	82.6	2.8	38.6	0.7
w/ outlier (5 subset)	86.0	2.4	37.6	0.5	82.2	2.9	38.8	0.4
w/o outlier (5 subset)	81.0	3.8	38.2	1.2	87	1.1	37.8	0.4
Rand. sampl. (10 seeds)								
w/ outlier (10 subset)	84.5	1.6	38.7	0.5	83.8	3.1	38.8	0.7
w/o outlier (9 subset)	85.0	3.2	36.2	0.6	86.3	4.4	35.9	0.9
w/ outlier (5 subset)	84.6	1.6	38.7	0.4	83.2	1.3	39	0.1
w/o outlier (5 subset)	85.9	2.2	36.2	0.2	87.1	3.0	35.8	0.6

Table 6.4: Reconstructed Z_{eff}, $\sigma_{Z_{\text{eff}}}$, x, and σ_x for the two uranium experiments using different combinations of sampling method, outlier filtering, number of data subsets, and the 5 mins open air measurements. The Z_{eff} and x for both time sequenced and randomly sampled data are the average values over all of the data subsets. The $\sigma_{Z_{\text{eff}}}$ and σ_x for the time sequenced data are the experimental reconstruction standard deviations calculated from the group of (5, 9, or 10) data subsets from each experiment. The $\sigma_{Z_{\text{eff}}}$ and σ_x for the randomly sampled data are calculated by first calculating the standard deviation from the group of (5 or 10) data subsets processed with the same random seed, then calculating the average $\sigma_{Z_{\text{eff}}}$ and σ_x across the 10 groups of data subsets with each of the subsets processed with a different random seed. Outliers are the first 10^{th} of the data from uranium experiment 1 and last 10^{th} of the data from uranium experiment 2.

two larger than the experimental standard deviations using randomly sampled data subsets. As an example, $\sigma_{Z_{\text{eff}}}$ reduced from 8.8 to 3.1 for uranium experiment 1 with outlier when dividing the data to 10 subsets by random sampling instead of time

sequencing. There is a reduction in $\sigma_{Z_{\text{eff}}}$ and σ_x across all results shown in Table 6.4, when the data division method changed from time sequenced to randomly sampled while keeping other parameters the same. This strongly indicates systematic time dependant variations occurred during the experiment.

Another observation drawn from the result is the increase in reconstruction accuracy for all cases by removing the outlier portion of the data (first 10^{th} of the data from uranium experiment 1 and last 10^{th} of the data from uranium experiment 2). This observation is expected as the outlier in prediction is an indication higher variations in the data that led to inaccurate Z_{eff} and x estimation. The same table shows the overall reconstruction precision is improved by using the 5 mins open air measurement after the experiment instead of the 5 mins open air measurement before the experiment. However, reconstruction accuracy is only improved on experiment 2 when the 5 mins open measurement after the experiment is used. This reflects that the open air measurements would indeed affect both the reconstruction accuracy and precision but the effect varies from experiment to experiment. Unfortunately, only one-third of all experiments performed had open air measurements after the experiment. As such, the effects of using the open air measurements after the experiment could not be investigated for all 19 experiments

The last important finding is the decrease of $\sigma_{Z_{\text{eff}}}$ and σ_x of the randomly sampled data with decreasing number of data subsets while keeping other parameters the same. For example, $\sigma_{Z_{\text{eff}}}$ was reduced by approximately 1.5 times when the number of data subsets reduced from 10 to 5 for randomly sampled data subsets with outlier, using 5 mins open air measurements before experiments. This reduction of 1.5 times is very close to 1.44, which is the square root of 2, representing a decrease of standard deviation if the reconstruction uncertainty is driven mainly by counting statistics.

One result of particular interest is the decrease of reconstruction precision for the prediction with 5 data subsets using time sequenced sampling and with the outliers removed. For these two experiments specifically, the first 10^{th} of the experimental data was removed from experiment 1 while the last 10^{th} of the experimental data was removed from experiment 2. The data was then equally divided into 5 data sub-

	SD($C_n(4.44)$)	$\sigma(C_n(4.44))$	SD($C_n(6.13)$)	$\sigma(C_n(6.13))$	SD($C_n(7.02)$)	$\sigma_{C_n(7.02)}$
U exp. 1	0.0393	0.0138	0.0070	0.0082	0.0074	0.0019
U exp. 2	0.0168	0.0124	0.0131	0.0083	0.0026	0.0020
Cu exp.	0.0132	0.0099	0.0071	0.0091	0.0045	0.0023
	SD($\frac{R_{exp}(4.44)}{R_{exp}(7.02)}$)	$\sigma(\frac{R_{exp}(4.44)}{R_{exp}(7.02)})$	SD($\frac{R_{exp}(6.13)}{R_{exp}(7.02)}$)	$\sigma(\frac{R_{exp}(6.13)}{R_{exp}(7.02)})$	SD($R_{exp}(7.02)$)	$\sigma(R_{exp}(7.02))$
U exp. 1	0.0591	0.0303	0.0084	0.0278	0.0029	0.0011
U exp. 2	0.0282	0.0285	0.0302	0.0270	0.0010	0.0011
Cu exp.	0.0043	0.0171	0.0129	0.0236	0.0018	0.0014

Table 6.5: SD($C_n(Energy)$), $\sigma(C_n(Energy))$, SD($\frac{R_{exp}(Energy)}{R_{exp}(Energy)}$) and $\sigma(\frac{R_{exp}(Energy)}{R_{exp}(Energy)})$ values for the two uranium and the copper experiments. The data was divided into 5 data subsets using time sequenced sampling. $C_n(Energy)$ are the recorded counts used in Eq. 6.1 while $\frac{R_{exp}(Energy)}{R_{exp}(Energy)}$ are the ratio used in Eq. 6.4. SD represent the experimental standard deviation calculated from the 5 data subsets. σ represent the average calculate σ from error propagation.

sets for reconstruction by time sequencing (gammas' recorded order), i.e. each data subsets contained 9/50 of the original 60 mins data. Table. 6.5 lists the experimental standard variations from the calculated values over the 5 data subsets (labeled as s.d.) and average calculated standard deviation from error propagation (labeled as σ) using the counts and error from the data processing. In the table, $C_n(E)$ and $\frac{R_{exp}(E)}{R_{exp}(E)}$ are calculated using the same definition as Eq. 6.1 and 6.2. The results of uranium experiment 1 shows $C_n(4.44)$ and $\frac{R_{exp}(4.44)}{R_{exp}(7.02)}$ varies more in experiment (0.0393 and 0.0591) than from the error propagation calculations (0.0138 and 0.0303). A similar conclusion can be drawn for the $C_n(7.02)$ and $R_{exp}(7.02)$. As for uranium experiment 2, experimental and error propagated standard deviations are comparable. Note that the calculated σ of $C_n(E)$ and $\frac{R_{exp}(E)}{R_{exp}(E)}$ from error propagation did not account for the correlation effects of the measurements. As ch0 and ch1 measurements at the same energy are positively correlated, and measurements at 6.13 and 7.02 MeV are positively correlated, the actual calculated standard deviation from error propagation should be much smaller than the one listed on the table in which correlation effects are unaccounted for. As seen on the $C_n(E)$ and $\frac{R_{exp}(E)}{R_{exp}(E)}$ for the copper experiment with more accurate and precise reconstruction predictions, the $\frac{R_{exp}(4.44)}{R_{exp}(7.02)}$ is only 0.0043 while the $\sigma(\frac{R_{exp}(4.44)}{R_{exp}(7.02)})$ is 0.0171. These results once again demonstrate the systematic uncertainty associated with the experiment, possibly stemming from the instability of the cyclotron, leading to high variation in $R_{exp}(E)$. Furthermore, for uranium, the reconstructed Z are more sensitive to the variation of F value in the minimization

	$\overline{\delta_Z}$	$\overline{\sigma_Z}$	$\overline{\delta_x}$	$\overline{\sigma_x}$
Time seq.(10 subset w/ outliers)				
homogeneous	4.3	6.5	2.6	3.1
heterogeneous	4.8	7.4	4.0	4.8
all	4.5	6.9	3.2	3.8
rand. sampl. (10 subset w/ outliers & 10 seed avg.)				
homogeneous	3.1	5.4	2.2	2.8
heterogeneous	4.6	7.6	3.7	4.8
all	3.7	6.2	2.8	3.6
rand. sampl. (5 subset w/ outliers & 10 seed avg.)				
homogeneous	4.0	2.0	3.9	1.9
heterogeneous	2.8	5.1	2.0	3.2
all	3.5	4.4	3.1	2.5

Table 6.6: Values of $\overline{\delta}$, which is the average difference between the reconstructed and actual value (representing accuracy), and $\overline{\sigma}$, which is the average standard deviation of the reconstructed values across the the data set (representing precision), for three categories of experiments (homogeneous, heterogeneous, and all 19 experiments). $\overline{\sigma}$ is the average σ across the set of experiments, where each individual σ for the time sequenced data are the experimental reconstruction standard deviations calculated from the data subsets of each of the experiments. Each individual σ for the randomly sampled data are calculated by first calculating the standard deviation from the group of (5 or 10) data subsets processed with the same random seed, then calculating the average σ and across the 10 groups of data subsets with each of the subsets processed with a different random seed. The average σ across the set of experiments in the three categories was then averaged again and listed as the $\overline{\sigma}$.

formula. An average change of 0.2 in F for uranium would lead to a Z_{eff} change of -6 to +1.38, while an average change of 0.2 in F for copper would only lead to a change of -1 and +1. Due to the lack of experimental data on uranium and high Z materials, the exact cause of the variation in Z_{eff} and x estimates could not be determined. The cause may stem from a combination of sensitivity of Z_{eff} on F value, quality of the background and peak fittings on the gamma spectra and the time dependant instability of the cyclotron during the experiment.

Numerical values of $\overline{\delta}$, which is the average difference between the reconstructed and actual value, and $\overline{\sigma}$, which is the average standard deviation of the reconstructed values across the data set for three categories of experiments (homogeneous, hetero-

geneous, and all 19 experiments) are summarized in Table. 6.6. Once again, there was an overall improvement of reconstruction accuracy and precision when the data division method changed from time sequencing to random sampling, reflecting the time dependant systematic uncertainty in the experiments. Furthermore, additional improvement was seen when the number of data subsets used were reduced from 10 to 5, likely due to the increase in counting statistics. Figure 6-4 shows the reconstructed values of Z_{eff} and x along with their experimental uncertainties for data divided by random sampling while Table 6.7 lists the values for each experiment. As with the time sequenced results, there was a significant separation between low-Z materials such as aluminum, medium-Z material such as tin, and high-Z material such as lead. On average, the reconstructed Z_{eff} and x were 3.7 and 2.8 from the actual values respectively, with a standard deviation (precision) of 6.2 and 3.6. These results would be a close representation of "stable" measurements with a slightly "defocused" proton beam, where the measured gamma spectra do not contain time dependant variations due to the instability of the cyclotron. Any time dependant variations on the data would be smeared by random sampling. With the average target current and average graphite collimator current of 6.0 and 0.56 μA respectively, and 6 mins measurement on each data subsets, these reconstruction results demonstrated the feasibility of using multiple monoenergetic photons generated from low energy nuclear reactions to accurately reconstruct the areal density and Z_{eff} of a variety of homogeneous and heterogeneous materials with a broad range of Z. However, with overlapping uncertainty (error bar) between lead and uranium predictions, one could not distinguish between the two using the current setup. In Sec. 6.4, extrapolation of current experimental data to a more intense gamma source was performed to estimate the source current and modification required for material discrimination between high-Z material. The result in Figure 6-4, Table 6.7, and Table. 6.6 only contain reconstructions using open air measurements before the experiment to keep the reconstruction parameters consistent throughout the whole table. However, the reconstruction accuracy might be improved by using different open air measurements due to the cyclotron stability.

Material	Actual Z_{eff}	Average Reconstructed Z_{eff}	$\sigma_{Z_{\text{eff}}}$	Actual x (g/cm^2)	Average Reconstructed x (g/cm^2)	σ_x (g/cm^2)
Aluminum 1 (Al)	13	14.9	3.4	59.4	56.2	2.7
Aluminum 2 (Al)	13	13.7	4.4	113.4	108	5.6
Iron (Fe)	∼24	23.9	3.5	56.0	57.2	2.6
Copper 1 (Cu)	29	28.4	3.3	48.8	48.5	1.4
Copper 2 (Cu)	29	32	3.9	60.3	59	1.9
Copper 3 (Cu)	29	24.5	2.5	88.9	91.1	3.7
Tin 1 (Sn)	50	50.9	7.8	49.0	47.7	2.5
Tin 2 (Sn)	50	48	10.4	73.1	73.5	5.0
Lead (Pb)	82	81	10.4	57.6	56.7	3.7
Uranium (U)	92	85.3	3.1	35.4	38.6	0.7
Uranium (U)	92	83.4	4.9	35.4	39	1.1
Pb + Al	∼35	40.9	5.4	61.0	62.2	2.8
Cu + Al	∼21	16.8	2.7	60.8	61.6	2.7
Pb + Cu	∼47	52.4	13.7	57.4	58.6	5.0
Pb + Sn	∼63	75.5	17.7	106.6	97.8	10.8
Cu + Sn	∼39	39.1	6.9	97.8	95.8	5.4
Sn + Al	∼29	35.3	5.0	96.1	89.8	4.2
Sn + Al	∼29	34.9	4.6	96.1	91.1	3.8
Sn + Al	∼29	33.3	4.6	96.1	91.8	3.4

Table 6.7: Average reconstructed Z_{eff} and areal density x for all MMGR experiments with actual values and reconstruction uncertainties listed. Each of the experiments was divided into data subsets by random sampling. The experimental data were divided into data subsets using random sampling. Each individual σ for the randomly sampled data were calculated by first calculating the standard deviation from the group of 10 data subsets processed with the same random seed, then calculating the average σ and across the 10 groups of data subsets with each of the subsets processed with a different random seed. The $\sim$ symbol indicates the actual Z_{eff} value of the heterogeneous cargo calculated using the method as described in Sec. 6.2.

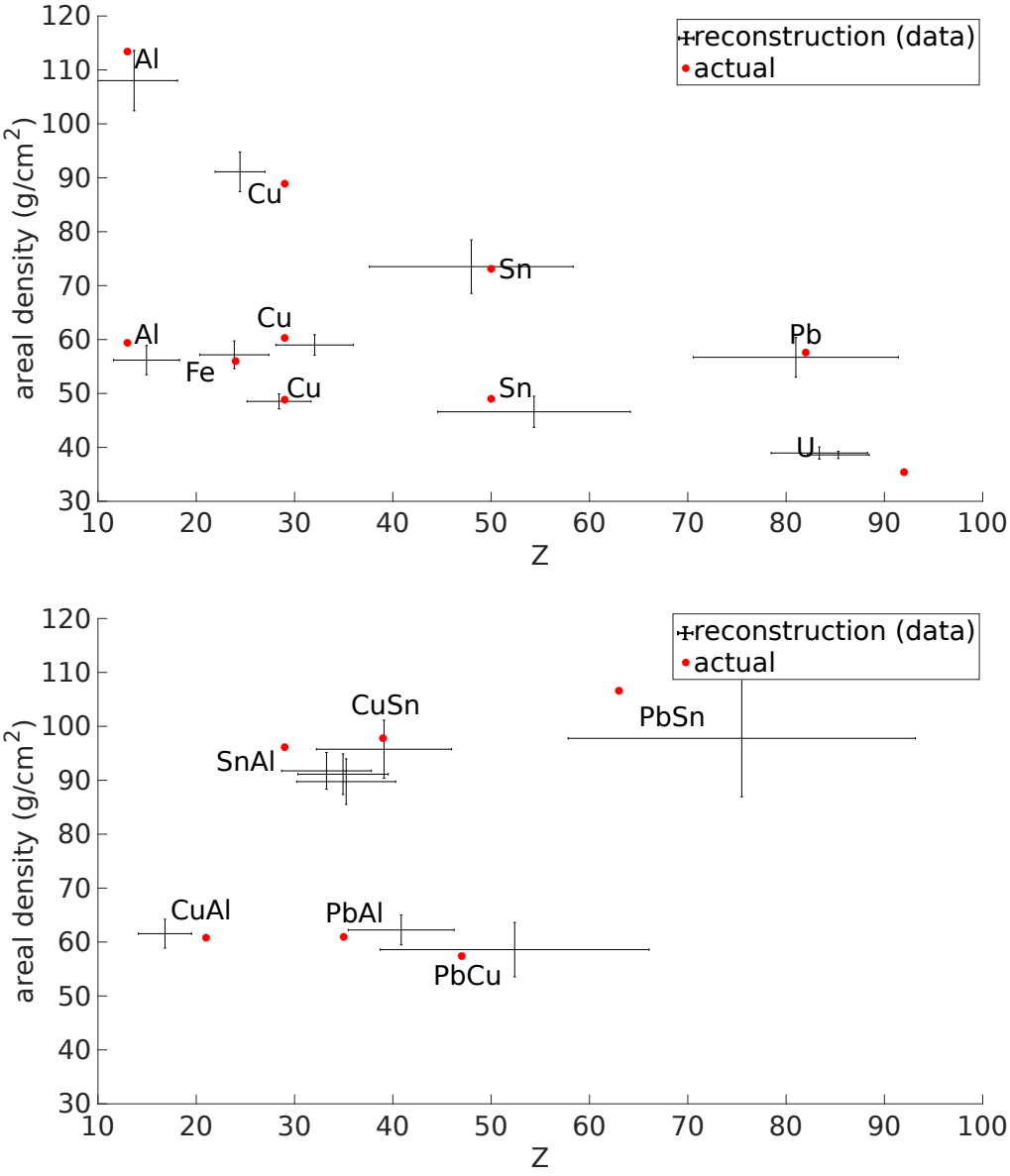

Figure 6-4: Reconstruction results of all homogeneous material (top) and heterogeneous material (bottom) MMGR experiments. The error bars represent the standard deviation (σ) of the reconstructed Z_{eff} and x in the data set for a particular mock cargo, and they are centered at the mean of the reconstructed values of the same data set. The red dots indicate the actual Z and x value of the materials. Two separate experiments were performed on the same depleted uranium mock cargo, and three separate experiments were performed on the same Sn+Al heterogeneous mock cargo. The experimental data were divided into data subsets using random sampling. Each individual σ for the randomly sampled data were calculated by first calculating the standard deviation from the group of 10 data subsets processed with the same random seed, then calculating the average σ and across the 10 groups of data subsets with each of the subsets processed with a different random seed.

6.4 Extrapolation and estimations for a future deployable system

With overlapping uncertainty (error bar) between lead and uranium predictions, one could not distinguish between the two using the current setup. It is then important to establish a metric to quantify the separation between two predictions. In order to estimate the system requirement by extrapolating experimental results to different reconstruction precision, the following figure of merit formula was used:

$$FOM = \frac{Z_2 - Z_1}{\sqrt{\sigma_2^2 + \sigma_1^2}} \tag{6.7}$$

where Z_1 and Z_2 are the actual Z values of two different materials and σ_1 and σ_2 are their corresponding reconstruction uncertainties within the 10 data subset. The FOM between lead and uranium in the current "ideal" experiment was 0.69 based on the results listed in Table. 6.7. For the record, the average current on the graphite collimator and water for each of the 5 mins lead experiment were 6.80 and 0.694 μA respectively, while they were 6.46 and 0.429 μA for the uranium experiment.

Using the same FOM formula, if the FOM increased to 2, the uncertainty for both measurements needed to be reduced by a factor of 2.23. Similarly, if the FOM increased to 3, the uncertainty for both measurements needed to be reduced by a factor of 3.34. These calculations assumed the uncertainty solely stemmed from counting statistics and the "ideal" radiography system would have an average reconstruction inaccuracy of zero. With such an assumption, the counts need to increase by 5.0 times and 11.2 times respectively in order to achieve a FOM of 2 and 3. Results showing the separation with FOM of 0.69 and 2 can be seen in Fig. 6-5. Another extrapolation was performed regarding scanning resolution and speed. In the experimental setup, the pixel size was approximately 2.54×2.54 cm. If the current detector setups and scanning time was maintained, the current of the cyclotron needed to be at approximately 34 and 76 μA respectively, in order to achieve a FOM of 2 and 3. If three instead of a single detector was used for the transmission measurement, the

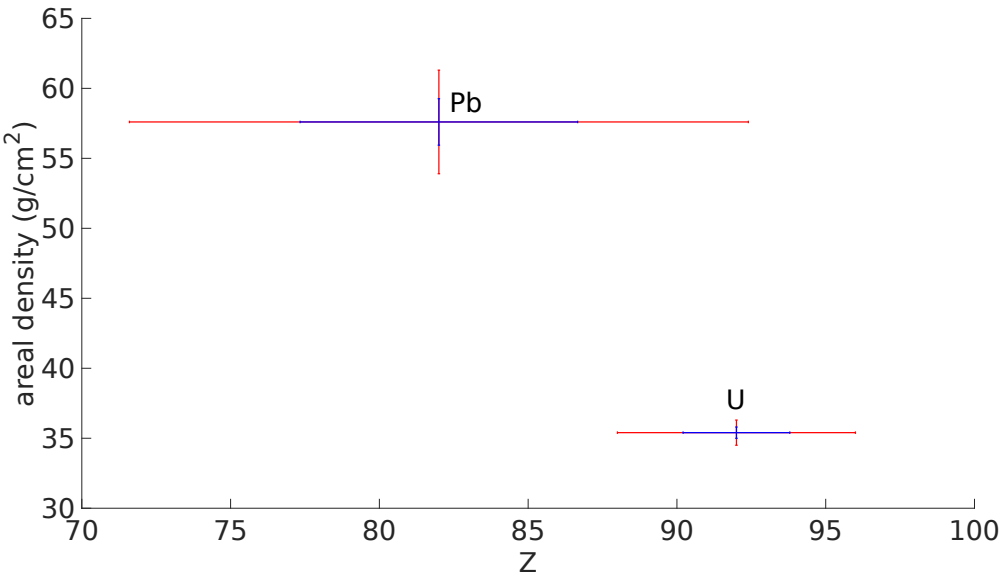

Figure 6-5: The separation of Pb and U with FOM of 0.69 and 2 using Eq. 6.7 and using experimental data with performance extrapolation.

current needed to be just 11 and 25 μA. In the future, if the cyclotron produces 19 MeV protons instead of 12 MeV, the 4.4, 6.13, 6.92, and 7.12 MeV gamma yield would increase by 2.6, 3.9, 2.0 and 4.0 times respectively. This will further lower the current to approximately 3.5 and 8.0 μA respectively in order to achieve FOM of 2 and 3.

Realistically, a screening rate of 5 mins per pixel with a pixel size of 2.54×2.54 cm makes cargo scanning an impractical feat. The estimated time needed to scan a 40 ft cargo will be almost 2400 mins. With the end goal being a 6 mins scan time with a resolution of 3×3 cm, a FOM of 2, and using three detector arrays, the current of the 19 MeV cyclotron will need to be approximately 1 mA in order to achieve the needed reconstruction precision. However, this current could be reduced by using NaI(Tl) detectors with higher detection efficiency or a coarser scan was conducted before a finer scan. Another factor that has not been taken into account yet is the generation of 15.1 MeV gammas from (p, p') reaction on ^{12}C if a 19 MeV beam is used. 15.1 MeV gammas will have even less gamma background and better separation with other gammas. Its attenuation also has stronger Z dependence, which improves the reconstruction accuracy in theory.

A potential MMGR system is pictured in Fig. 6-6. The cyclotron is placed inside

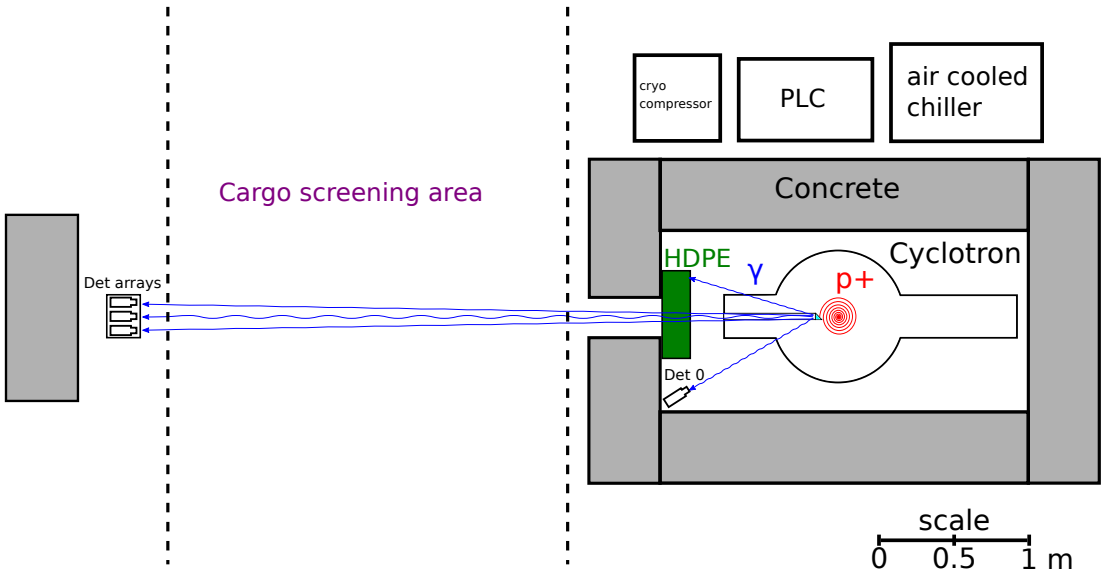

Figure 6-6: An example of a floor plan for a deployable MMGR system with all equipment and auxiliary systems labelled.

an enclosed area with 50 cm of concrete shielding, generating multiple monoenergetic gammas. From attenuation calculations, 50 cm of concrete would attenuate 96.5% of gammas at 5 MeV. Assuming the height of shielding is 250 cm, the total weight of shielding needed will be 23 tonnes. If 25 cm of concrete is used, the weight will drop to approximately 11.5 tonnes, shielding 81% of gammas at 5 MeV. From scaling of the dose measurements in Table. 4.1, the unattenuated gamma dose at the location of the detector will be approximately 0.6 mR/s for a scan with 19 MeV protons at 650 μA with a speed of 4 cm/s. Meanwhile, the gamma dose from gamma attenuated by 50 cm of concrete at a distance of 3 m will be 0.046 mR/s. The gammas generated by the cyclotron are then collimated and transmitted through the screening cargo container. Three vertical arrays of detectors are used to measure the transmission spectrum. It is important to have 8 inch of HDPE covering the concrete collimator opening to reduce the amount of neutron reaching the cargo container. In this floor plan, the detector arrays are located 4.5 m away from the center of the cyclotron, which is very close to the distance of 4 m distance in MMGR experiments conducted in this study. As mentioned previously, an air cooled chiller need to be installed so the cyclotron can remain adequately cool during transportation for a (usable) mobile

system. However, the cyclotron cannot be transported fully charged. The system setup time will consist of charging up the magnet, setting up concrete shielding, and assembling the detector arrays.

6.5 Limitations of MMGR

One major disadvantage of this on-axis MMGR technique is that only the Z_{eff} would be determined for a mixture of different materials (heterogeneous cargoes), despite its efficiency at determining Z of homogeneous cargoes. As seen in Sec. 6.2, a knowledgeable smuggler would be capable of masking SNM (high Z) with large amounts of low Z material in order to lower the reconstructed Z_{eff} from MMGR. One method to overcome this vulnerability is to screen the containers from multiple angles. Using a tomography approach, the Z_{eff} predictions at different scanning angles can be combined so that the system could distinguish masked SNM from other benign cargoes. Further research will need to be conducted in order to explore the feasibility of combining MMGR with multiple angle tomography technique. However, MMGR combined with imaging could already counteract the mixed material limitation in some hypothetical scenario. For example, if a smuggler decided to mask a kilogram of uranium in a cube (3.75 by 3.75 by 3.75 cm) with lead. The amount of lead needed to lower the combine Z value to 82 calculated with Eq. 6.6 is approximately 41 cm. If the lead was in a cube of 41 by 41 by 41 cm, it would weigh 780 kg and an image of a big block of high-Z material would be suspicious enough to raise an alarm. There may be other criteria to raise an alarm for further screening (e.g. pixels of a certain size and above some threshold of ΔZ values with the surrounding material). As such, there might be multiple methods to minimize the vulnerability and reduce some current requirements for the radiography system.

6.6 Penetration study with ANSI N42.46 standard

One of the most important specification for a screening system is its penetrability through the cargoes. Written in the ANSI N42.46 (American National Standard for Determination of the Imaging Performance of X-Ray and Gamma-Ray Systems for Cargo and Vehicle Security Screening), a test standard was defined to determine the penetrability of a system by "measuring the maximum thickness of steel through which the orientation of a specified test object can be determined in an x-ray or gamma-ray image" [118]. The test object is a 30 cm long and 30 cm wide arrowhead-shaped steel with its thickness at 20% of the expected measured penetration (combine thickness of steel blocking plate and test object). This thickness is also known as 20% contrast. The greatest total thickness of blocking plates plus thickness in which the orientation of the test object can be identified is classified as the maximum penetration for that specific test object location. According to this standard, the blocking plate needs to be at least 60 by 60 cm in size.

Instead of running numerous simulations for which there is currently a lack of sufficient information, such as gammas origins and absolute yield, the penetration test was performed instead with the following method:

1. Gamma counts and uncertainties measured at Ch1 (on-axis) detector without background subtraction were recorded for a 5 mins open air experiment with the average current on water and graphite collimator at 7.06 μA and 0.829 μA respectively. The experimental setup used to measure this open air data was exactly the same method as mentioned in Sec. 5.2. The counts and uncertainties were tallied in 4 regions: 1 to 1.5 MeV, 1.5 to 2 MeV, 2 to 3.3 MeV, and 3.3 to 4.44 MeV.

2. For each energy region, a mass attenuation coefficient at the median energy was found using the NIST database [2].

3. Using the test object dimension provided in the ANSI N42.46 standard, an

attenuation template was created to display the fraction of beam that would pass through only the backplate assuming 2.54×2.54 cm pixels. This attenuation template is plotted as a heatmap in Fig. 6-7.

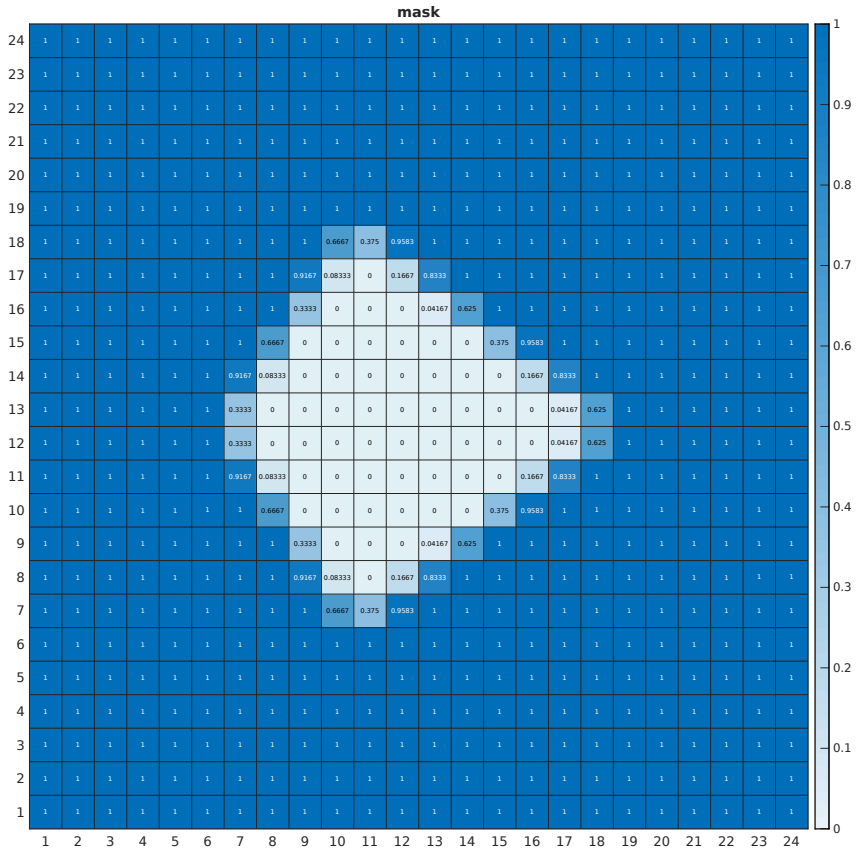

Figure 6-7: The attenuation template representing the fraction of the beam that is hitting the backplate calculated from the specification mentioned in the ANSI N42.46 standard. This template was used for subsequent calculation. The pixel size is 2.54×2.54 cm and the test object points to the right in this template.

4. The penetration test setup assumes the usage of three vertical detector arrays for the scanning image. Each pixel would be "scanned" by three different detectors. The cyclotron was assumed to be running 14 μA (double of the open air measurement) and producing 12 MeV protons. The scanning speed was also assumed to be 4.064 cm/s, in other words, 5 mins for 40 feet or 0.0104 mins per pixel.

5. The mean estimated counts at each pixel in the test was then calculated by first attenuating the measured open air gammas using the attenuation template, steel thickness, and the mass attenuation coefficient for each energy region and then summing them. The scaling from number of detectors, cyclotron current, and scanning speed were also taken into account.

6. An image of the scan was then generated in which the calculated counts at each pixel was randomly sampled with the assumption that the counts are Poisson distributed with λ equal to the mean from the estimated counts.

7. A total of 20 images were generated for each total thickness with the object orientated at random positions (up, down, left, or right).

8. Tests were ran at increasing thicknesses until the orientation of the object for any of the 20 images was falsely identified by visual inspection. The last thickness in which all 20 orientations were correctly identified was considered the maximum penetration thickness. Fig. 6-8 provides an example of one such image.

The maximum penetration thickness was found to be approximately 45 cm. A figure of merit was found by calculating the difference in counts between the pixel with backplate only and full thickness divided by the quadratic sum of their corresponding uncertainties. It is found to be approximately 3.10. At 48 cm, only 59 out of 60 orientations of the test object were correctly identified. This 45 cm penetration thickness is considered to be the upper bound of the penetration as the calculation performed only takes into account the attenuation of gammas but not the scattering of gammas from the increasing thickness of the test object and backplate. In order to have a more accurate estimation on the penetration thickness, GEANT4 simulations with detailed detector geometries and experimental setup would be needed. However, one needs to keep in mind that a future system may have higher protons energy and higher source current, which would increase gamma yield and increase the penetrability of the system.

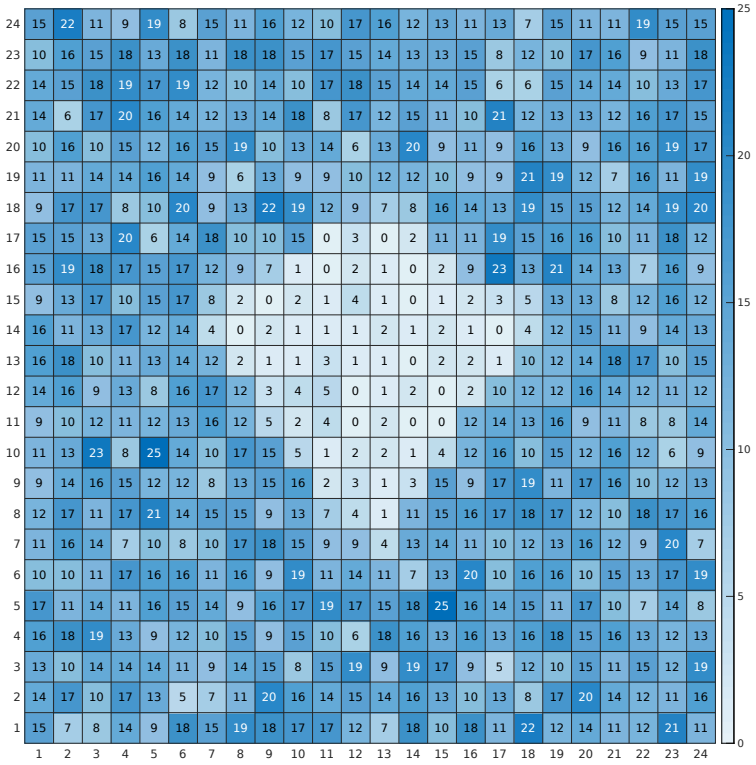

Figure 6-8: A simulated image from the penetration study. The calculated counts at each pixel was randomly sampled using Poisson distribution with λ equal to the mean estimated counts. The test object is oriented downward in this image and the total thickness of the task object with the backplate is 45 cm.

Chapter 7

Conclusions and recommendations

This chapter concludes this PhD study and provides some recommendations for future works to further improve radiography performance and better understand other deployment related issues.

7.1 Conclusions

This thesis work demonstrated the feasibility of using multiple monoenergetic photons generated from low energy nuclear reactions to accurately reconstruct the areal density and Z_{eff} of a variety of homogeneous and heterogeneous mock cargoes with a broad range of Z. As a continuation and extension of previous work, we were not only able to achieve an average Z_{eff} reconstruction accuracy and uncertainty at 3.7 and 6.2, we also successfully demonstrated the use of a compact superconducting cyclotron with a hybrid graphite water target to generate the needed monoenergetic photons at 4.4, 6.1, 6.9, and 7.1 MeV from low energy $(p, p'\gamma)$ nuclear reactions on carbon and oxygen. With such accuracy and precision, one could distinguish between SNM such as uranium from other high-Z benign material such as tungsten.

This experiment utilized a small compact superconducting cyclotron (the ION-12^{SC}), demonstrating that a mobile MMGR screening system could be achieved and possibly deployed at ports and other border crossings for cargo screening. Some extrapolation and estimations were also performed to predict the performance of future

superconducting cyclotron based MMGR system. Recommendations and suggestions on possible improvements such as system deployments, operations, cooling, and transportation were also discussed.

7.2 Recommendations for future works

The first and foremost recommendation is to focus on improving precision by lowering the uncertainty of reconstruction. Since precision of the measurements was limited by statistical precision of the collected spectrum, there are two areas of focus for future work: increase gamma intensity and system stability. To increase gamma intensity, future work should focus on using accelerators with higher energies as this will increase the yield of the photons, as shown in calculations described in Figure 4-6. For example, increasing the proton beam energy from 12 MeV to 19 MeV would increase the gamma yield by two to four times, while 19 MeV protons are only slightly above the neutron production thresholds for graphite and oxygen. Increasing proton beam energy is not the only way to increase gamma yield. Increasing currents are also necessary and will lead to direct increase of gamma production. Based on the results from this study, a 19 MeV proton beam at approximately 1 mA is required to differentiate lead and uranium with a 2σ discrimination if the scan was performed at a speed of 4 cm/s with a resolution of 3 cm by 3 cm resolution. However, with the addition of 15.1 MeV gammas from $(p, p'\gamma)$ on carbon using 19 MeV protons, further research will have to be conducted to accurately evaluate the reconstruction performance. With such a huge increase of beam current required, the power induced by proton on target will be almost 19 kW. As such, accelerators with external beams are required in order to improve target cooling.

Besides increasing gamma production, beam stability is also important for a precise reconstruction. As discussed in Sec. 6.3 and Appendix. B, the current cyclotron in use was not very stable, led to instability of gamma production and increased in reconstruction uncertainty (less precise). As such, an external beam, improvements on RF and target cooling are needed to achieve better reconstruction precision by

stabilizing the proton beam. With advancements in high temperature superconductors and compact cyclotron development, cyclotrons would become more compact, cheaper in cost, and more stable in performance, thus more attractive to users. Another recommendation would be to improve reconstruction performance by further optimizing background fitting and subtraction with the possibility of using GEANT4 simulation to model the gamma background. With better methods to subtract gamma background, the uncertainty on the recorded counts in the gamma transmission spectrum could be reduced to improve reconstruction precision. Studies on correlations between gamma productions and measurement on different detector and gamma energies would also improve σ calculation for the minimization formula and would possibly improve reconstruction accuracy and precision.

For a deployable and reliable system, the cyclotron should have a long uptime (time accessible for use) and very short downtime from maintenance and repairs. The initial setup time should also be minimized. More studies need to be done in order to explore the feasibility of transporting a cooled cyclotron and the possibility of using an air-cooled chiller instead of water-cooled chiller to make the cyclotron independent from other auxiliary systems. In addition, development and advancement in high temperature superconductors may lead to superconducting cyclotrons operating at higher temperatures, thus reducing the requirement on cooling power and cooling time.

In the current system, the cyclotron, chiller, electronics, and the cryo compressor should all fit in a medium duty truck without exceeding the weight limit. However, more studies need to be done to explore the radiation shielding requirement to reduce the shielding weight. By scaling the dose measurements listed in Table. 4.1, the unattenuated gamma dose at 4.5 m from the cyclotron will be approximately 0.39 mR/s for a scan at a speed of 4 cm/s with 19 MeV protons at 650 μA. If 25 cm thick and 250 cm tall concrete shielding are placed around the cyclotron, the concrete will have total weight of 11.5 tonnes, which will be the largest contributor to the total system weight.

As mentioned before, a knowledgeable smuggler would be able to mask SNM (high

Z) with large amounts of low Z material in order to lower the reconstructed Z_{eff} from MMGR. One possibility to overcome this vulnerability is to screen the containers in multiple angles with a tomography approach. Future studies need to explore the feasibility and practicality to combine MMGR with multiple angle tomography technique. Furthermore, only limited heterogeneous experiments were conducted in the study. More experiments with different heterogeneous cargoes would be needed to adequately evaluate the system performance in a realistic scenario.

Finally, future works should also focus on the detector choice. Instead of using expensive $LaBr_3$ detectors, it might be more economical to use cheaper NaI with better detection efficiency but lower resolution for the detector arrays. Experiments need to be conducted and new reconstruction algorithms may need to be developed to evaluate the performance difference with such changes.

Appendix A

List of cyclotron maintenance, repairs, and upgrades

Below lists all the events that resulted in a non-operational cyclotron, including and descriptions of the upgrades and events.

- Feb 9th 2017: Cyclotron installed.
- Feb 2017: The RF fingers burned out and needed repairing. Downtime of approximately 1 week. A design fix was performed to address this problem involving reinforced RF fingers.
- May 2017: Magnet discharged for a power outage, then unable to cool down due to needing a helium recharge. Cyclotron down for 4 weeks ($\sim$1 for ramp down, $\sim$3 for helium recharging).
- Jun 2017 - Jul 2017: Cyclotron quenched from MIT chilled water failure. Cyclotron non-operable for $\sim$6 weeks due to humidity issues (4 weeks), a leak in the two RF amplifiers (1 week), and then modifications to address issues from replacing the RF amplifiers (1 week). This did not include the visits to the Ionetix facilities in East Lansing.
- Apr 2018: Cyclotron quenched and unable to ramp due to a broken magnet power supply fan. Down for 3 weeks while awaiting spare parts and repairs.

- May 2018 - Jun 2018: Excessive RF heating due to corrosion related RF heating issues. Problem affected operations for approximately 1 year. A design fix has been implemented to address this problem. Cyclotron down for 5 weeks for repair (4 weeks lead time, 1 week active repair). Repairs included replacing the leaf springs, which held the dummy Dee against the stops with coil spring and aluminum connectors to improve the cooling on the dummy Dee and ion source for better ion source performance and beam stability. Modifications to install steel liner at the contact point of the dummy Dee support arms to reduce corrosion due to mixed metals contact of aluminum, steel, and copper. Installation of a new RF stem support block with a micrometer screw that allowed accurate adjustment of the position of the Dee to maximize beam output and reduce arcing.

- Jul 2018: RF arcing issues due to a broken ceramic RF stem insulator. Cyclotron down for 1 week for new ceramic RF stem insulator shipment.

- Aug 2018: RF arcing issues due to another broken ceramic insulator. This issue with the broken ceramic insulator was found to be related to the previous upgrades addressing the RF heating and corrosion. The newly modified Dee arms were not aligned properly and imposed excessive pressure on the insulator. Cyclotron down for 3 weeks for complete replacement of Dee arms and the RF box.

- Oct 2018: Magnet quenched due to a power outage. Cyclotron down for 1 week. Vacuum plumbing work performed to reroute the beam chamber to evacuate the cryovessel due to the broken cryovessel turbo.

- Nov 2018 - Dec 2018: Magnet quenched from a power outage. Cyclotron down for 3 weeks.

- Apr 2019 - May 2019: Magnet ramped down and warmed up due to a 4 day planned power outage. Cyclotron down for 3 weeks for vacuum pumping and

cooling of magnets. Improved vacuum purging procedures were written to reduce future cooling time.

- May 2019 - Aug 2019: Arcing issues for 2-3 weeks. Ceramic RF stem insulator discovered to be broken. 9 additional weeks downtime from financial negotiation to complete installation of newly designed Dee and Dee arms. This upgrade introduced direct water cooling to the Dee to increase ion source cooling, performance, and stability. The newly improved design also reduced the length of the ceramic RF stem insulator for longer operation life.

- Sep 2019: MIT chilled water cut off unexpectedly due to a facility repair. A re-pressurized chiller water pump for the Vault was found leaking and needed repairs. Temporary plumbing works conducted to reroute the chiller to use MIT chilled water from CLASS (upstairs) to cool down the cyclotron. Total downtime was approximately 1 week.

Out of the 126 weeks since the installation up until Oct 1st 2019, there was a total of 43 weeks in which CHARON was down, including 29 weeks due to cyclotron related issues and 14 weeks due to facility related issues.

Appendix B

Cyclotron stability study

From Fig. B-1, some reconstruction values of time sequenced data were more than 2 standard deviations from the mean values of the predictions. Examples of these outliers were the second data subset for the 73.1 g/cm^2 tin MMGR experiment and the fifth and tenth data subset for the 57.6 g/cm^2 lead MMGR experiment. Further investigation into the detection of such outliers in order to improve reconstruction accuracy.

The first attempt to detect and predict the occurrence of outliers involved investigating possible correlations between prediction accuracy and the current measured on the target and collimator. In Fig. B-2, there was a sudden drop of current on water and collimator due to two cyclotron trips during the second portion of the 73.1 g/cm^2 tin MMGR experiment. However, a similar sudden change in current also occurred at portion 7 of the experiment but no significant change in reconstruction values were observed. There were similar effects from other experiments but the results were inconclusive. At best, the outliers could be said to be partially related to the trips of cyclotron or change of current from RF frequency tuning during the experiment. The outlying predictions depends not on current along. The portion number on the figures were the data subset index for the corresponding reconstruction.

The second approach is to find out if the gamma production ratios at Channel 0 were different during the experiment. In Fig. B-3, we were able to observe a sudden change of the 4.44 MeV to 7.02 MeV and 6.13 MeV to 7.02 MeV gamma ratios for the

second data subset of the 73.1 g/cm^2 tin MMGR experiment measured by channel 0. However, these ratios were not significantly different for all other outliers. This concludes that using only gamma production ratios at Channel 0 would not be sufficient to detect an outlying prediction.

The cause of instability to the cyclotron could not be identified or eliminated during the experiment due to inconclusive results. One possible explanation could be due to statistical fluctuation in data and the only ways to minimize outliers are to increase the statistics of the MMGR experiment or attempt to keep the cyclotron operation as stable as possible by not altering the operation parameters throughout the experiment. The oulier may cause by a combination of variations in measurement at different channel and different gamma energy. With this shift of focus, gamma count ratios between channel 1 over channel 0 were plotted. From inspecting the 4.44 over 7.02 MeV gamma ratios, 4.44 over 7.02 MeV gamma ratio, and 7.02 MeV ratios in Fig. B-4, at least one or more gamma ratios of most outlying data subsets were indeed more than one standard deviation away from their corresponding 10-portions experimental mean. This shows potential variations of gamma ratios caused by instability of the cyclotron would lead to decreases in reconstruction accuracy. However, this variation could not be detected during a radiography scan to eliminate outliers because the inspected materials would not be known to the inspector. Increasing the counting statistics from MMGR experiments and improving gamma production stability remain as the only ways possible to minimize prediction outliers.

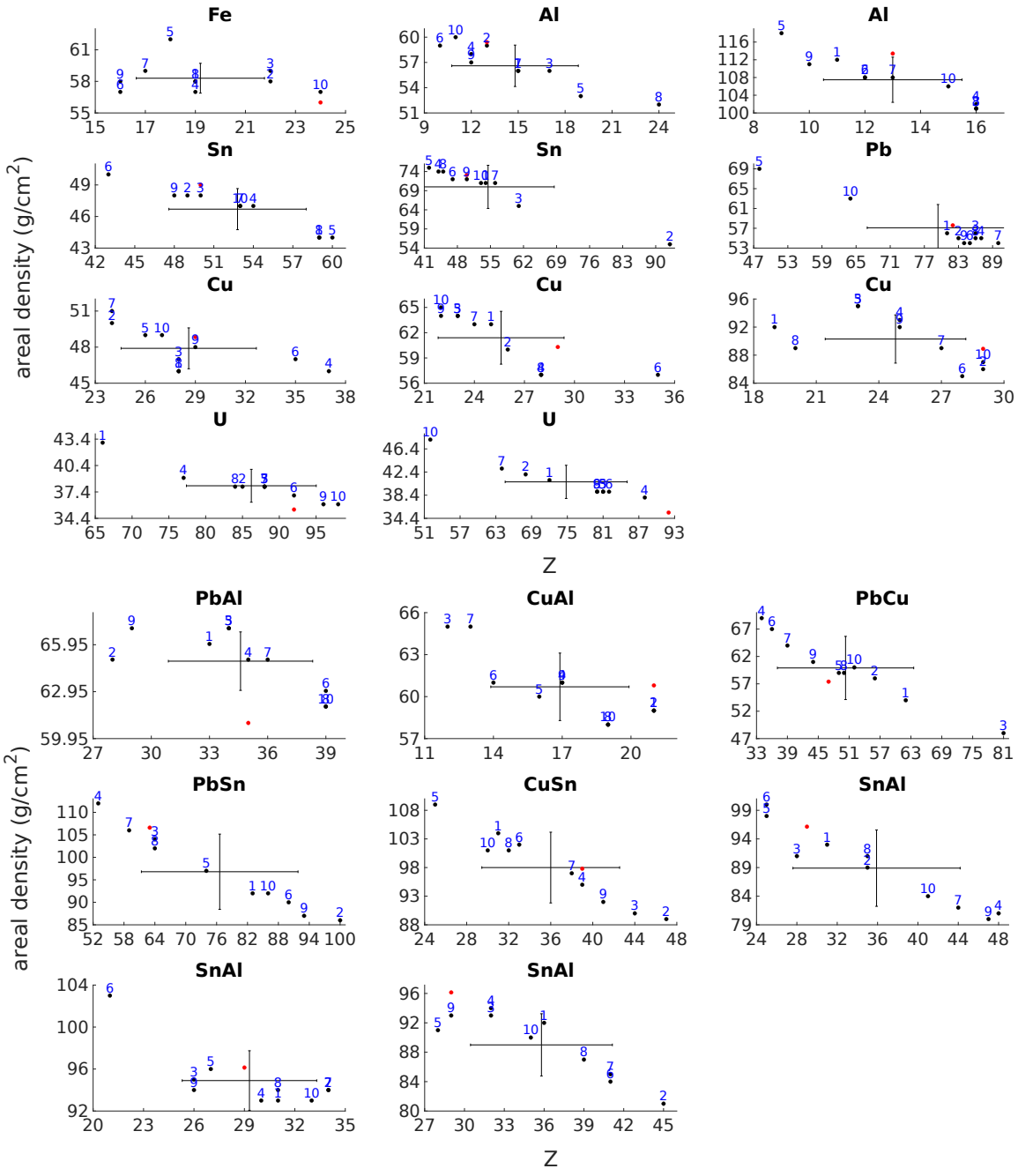

Figure B-1: Reconstructed Z_{eff} and x of each data subset for homogeneous (top) and heterogeneous (bottom) material MMGR experiments. Each of the experiments were divided into 10 data subsets by the gammas' recording time (time sequencing). Each black dot represent the reconstructed value and are labeled with a blue number indicating the portion number of the data subset. The red dots indicate the actual Z and x value of each material. The error bar centered at the mean of the predicted values represent the experimental standard deviation over the Z_{eff} and x in the data set for a particular mock cargo.

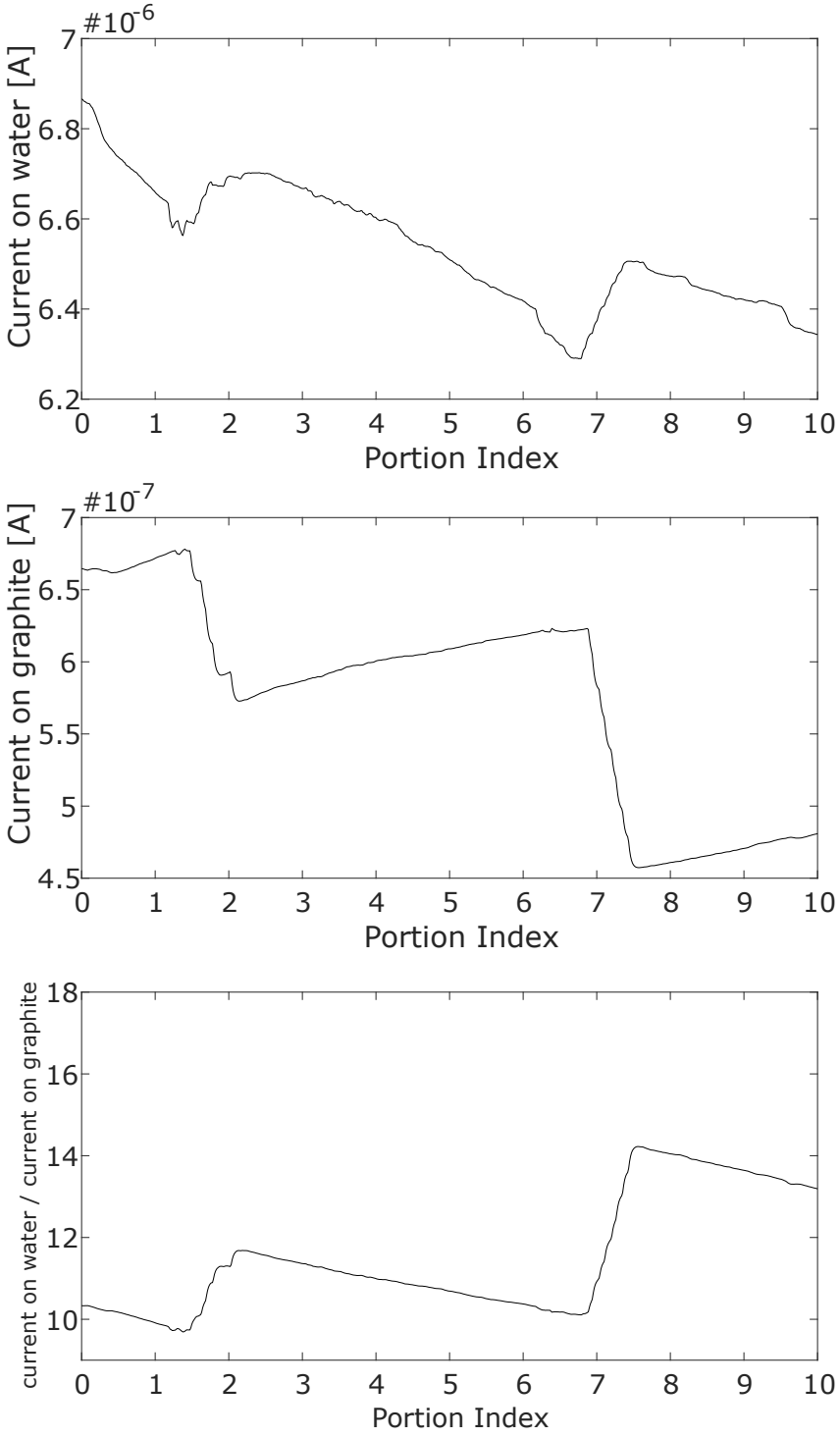

Figure B-2: Top: Current measured on the water for the tin experiment. Middle: Current measured on the graphite collimator for the tin experiment. Bottom: Ratio of current measured on water over current measured on graphite collimator for the tin experiment. Each of the experiments were divided into 10 data subsets by the gammas' recording time (time sequencing). The portion number on the figures were the data subset index for the corresponding reconstruction.

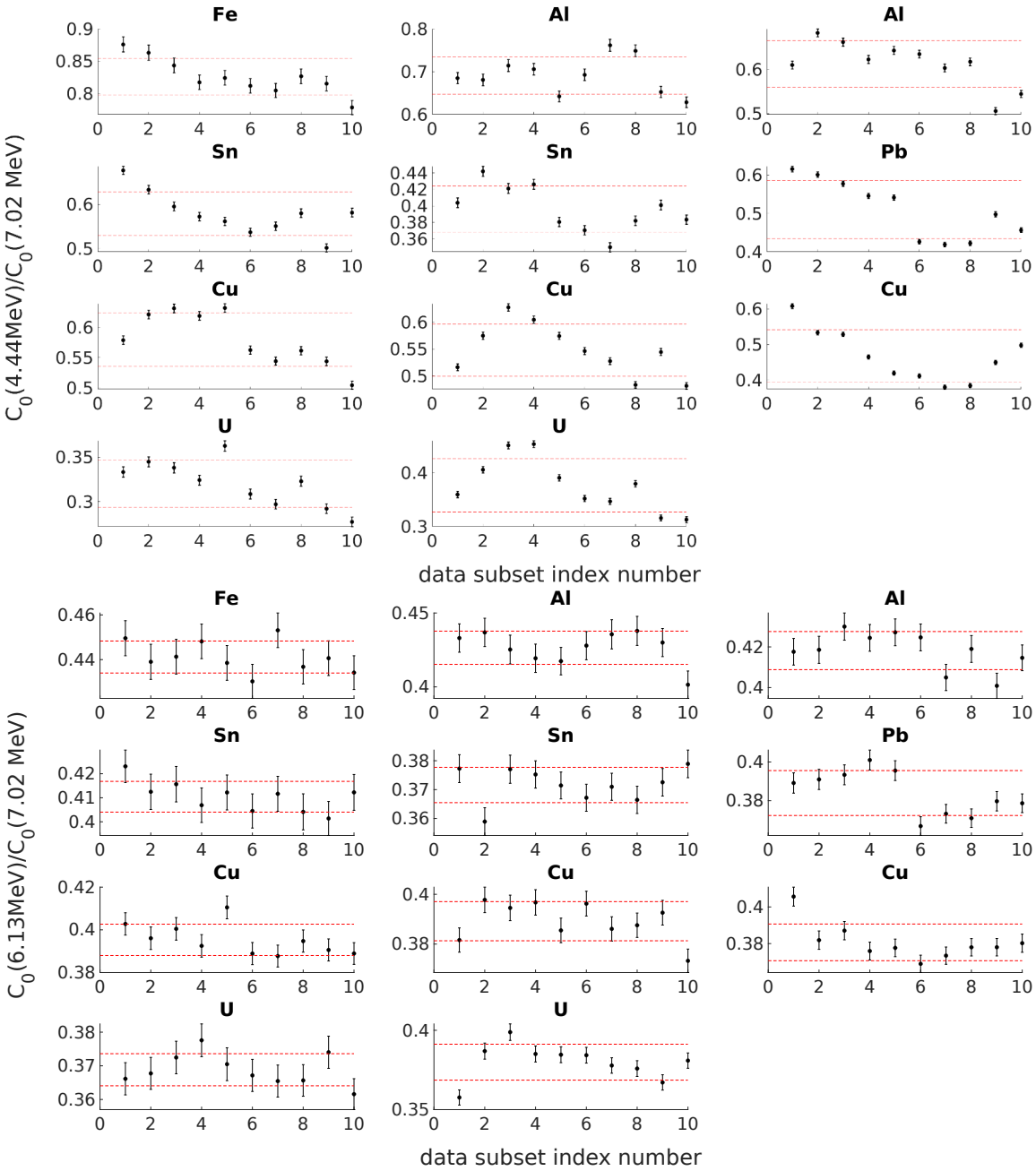

Figure B-3: Top: $\frac{C_0(4.44MeV)}{C_0(7.017MeV)}$ for all experiments with homogeneous cargoes. Bottom: $\frac{C_0(6.13MeV)}{C_0(7.017MeV)}$ for all experiments with homogeneous cargoes. The positions of each subfigure was the same as the top plot of Fig. B-1. The red dotted lines were one standard deviation from the mean of the ratio in each data subset of the same experiment.

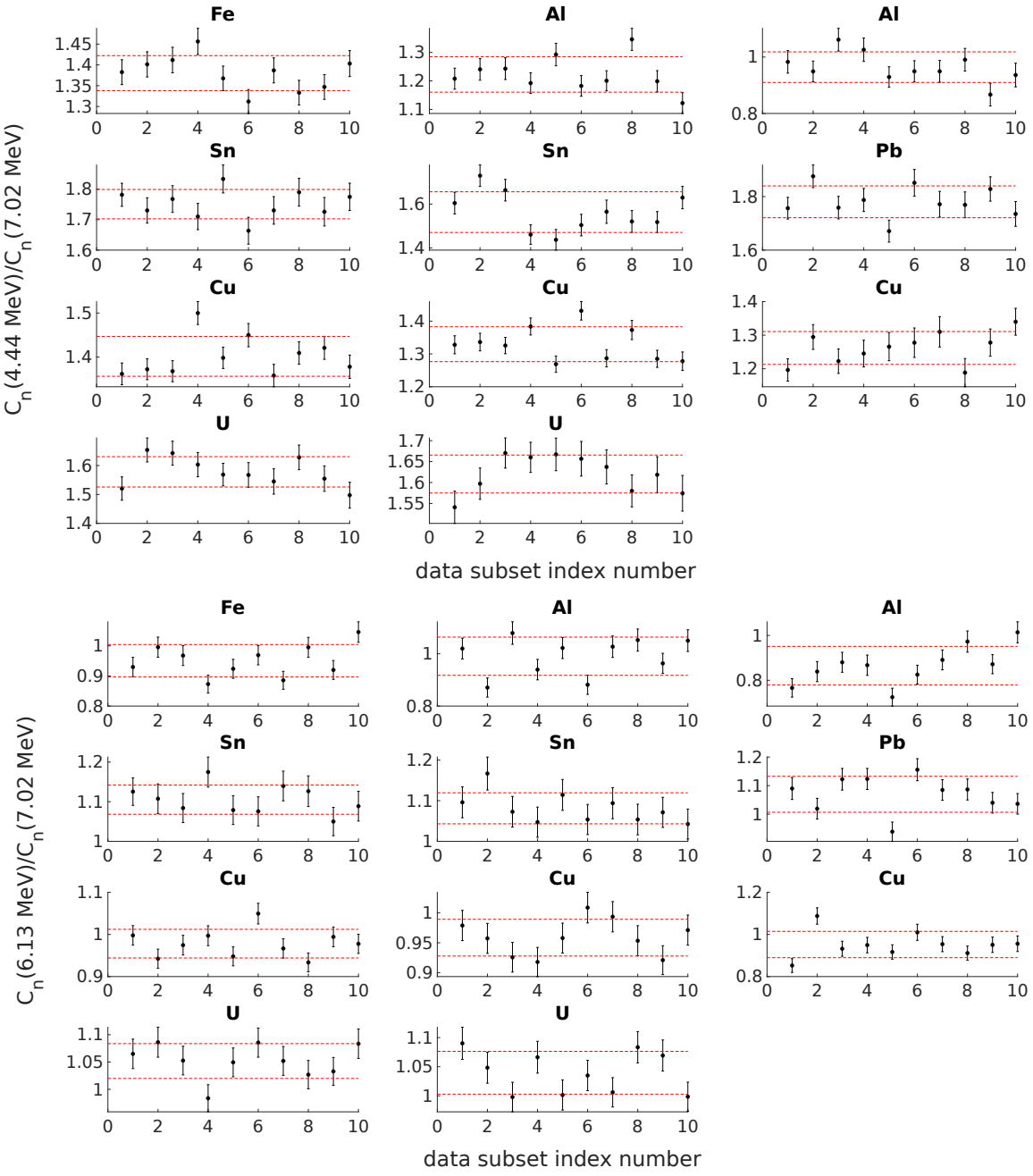

Figure B-4: Top: $\frac{C_n(4.44MeV)}{C_n(7.017MeV)}$ for all experiments with homogeneous cargoes. Bottom: $\frac{C_n(6.13MeV)}{C_n(7.017MeV)}$ for all experiments with homogeneous cargoes. $C_n(E) = \frac{C_1(E)}{C_0(E)}$. The red dotted lines were one standard deviation from the mean reconstruction values for each set of ten reconstructions. The positions of each subfigure was the same as the top plot of Fig. B-1 and the portion number on the figures were the data subset index for the corresponding reconstruction.

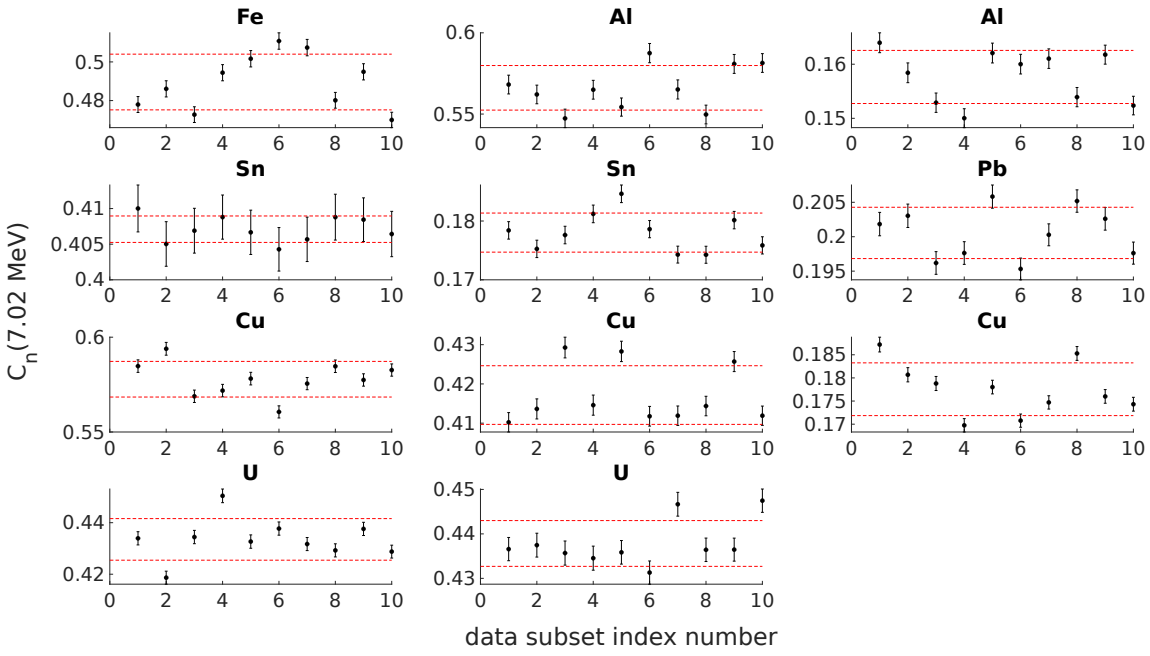

Figure B-5: $C_n(7.017MeV)$ for all experiments with homogeneous cargoes. $C_n(E) = \frac{C_1(E)}{C_0(E)}$. The red dotted lines were one standard deviation from the mean reconstruction values for each set of ten reconstructions. The positions of each subfigure was the same as the top plot of Fig. B-1 and the portion number on the figures were the data subset index for the corresponding reconstruction.

Bibliography

[1] B. S. Henderson, "Analysis of the Frequency and Detectability of Objects Resembling Nuclear/Radiological Threats in Commercial Cargo," *arXiv e-prints*, p. arXiv:1901.03753, Dec 2018.

[2] M. Berger, J. Hubbell, S. Seltzer, J. Chang, J. Coursey, R. Sukumar, and D. Zucker, "XCOM: Photon cross sections database," *NIST Standard Reference Database*, vol. 8, pp. 87–3597, 01 2009.

[3] J. Rahon, A. Danagoulian, T. D. MacDonald, Z. S. Hartwig, and R. C. Lanza, "Spectroscopic neutron radiography for a cargo scanning system," *Nuclear Instruments and Methods in Physics Research Section A: Accelerators, Spectrometers, Detectors and Associated Equipment*, vol. 820, pp. 141 – 145, 2016. [Online]. Available: http://www.sciencedirect.com/science/article/pii/S0168900216300419

[4] J. Rahon and A. Danagoulian, "Hydrogenous content identification in heterogeneous cargoes via multiple monoenergetic neutron radiography," 2019.

[5] B. E. O'Day *et al.*, "Initial results from a multiple monoenergetic gamma radiography system for nuclear security," *Nucl. Instrum. Meth.*, vol. A 506, pp. 68–76, 2016. [Online]. Available: http://www.sciencedirect.com/science/article/pii/S0168900216305198

[6] B. E. O'Day, "A Novel Low-dose Approach to Active Detection of Shielded High-Z Material," Ph.D. dissertation, Massachusetts Institute of Technology, 2015.

[7] B. S. Henderson, H. Y. Lee, T. D. MacDonald, R. G. Nelson, A. Danagoulian *et al.*, "Experimental demonstration of multiple monoenergetic gamma radiography for effective atomic number identification in cargo inspection," *Journal of Applied Physics*, vol. 123, no. 16, p. 164901, 2018. [Online]. Available: https://doi.org/10.1063/1.5025805

[8] M. Descalle, D. Manatt, and D. Slaughter, "Analysis of Recent Manifests for Goods Imported through US Ports," *Lawerence Livermore National Laboratory*, 9 2006.

[9] "IAEA INCIDENT AND TRAFFICKING DATABASE (ITDB) Incidents of nuclear and other radioactive material out of regulatory control: 2019 Fact Sheet," 2019. [Online]. Available: https://www.iaea.org/sites/default/files/19/04/itdb-factsheet-2019.pdf

[10] "Safeguard Categories of SNM," Aug. 2017. [Online]. Available: https://www.nrc.gov/security/domestic/mca/snm.html

[11] W. C. Potter and E. Sokova, "Illicit nuclear trafficking in the NIS: What's new? What's true?" *The Nonproliferation Review*, vol. 9, no. 2, pp. 112–120, 2002. [Online]. Available: https://doi.org/10.1080/10736700208436896

[12] F. S. Lyudmila Zaitseva, "Nuclear Trafficking Issues in the Black Sea Region," Stockholm International Peace Research Institute (SIPRI), Tech. Rep. 39, Apr. 2014. [Online]. Available: https://www.sipri.org/sites/default/files/EUNPC_no-39.pdf

[13] "Top Ten Cases of Nuclear Thefts Gone Wrong," Feb. 2013. [Online]. Available: https://www.smithsonianmag.com/science-nature/top-ten-cases-of-nuclear-thefts-gone-wrong-10854803/

[14] "Countering Weapons of Mass Destruction Office," Dec. 2018. [Online]. Available: https://www.dhs.gov/countering-weapons-mass-destruction-office

[15] K. GILSINAN, "Why Moldova May Be the Scariest Country on Earth," Oct. 2015. [Online]. Available: https://www.theatlantic.com/international/archive/2015/10/moldova-nuclear-weapons-isis/409456/

[16] I. Arguello and E. J. Buis, "The global impacts of a terrorist nuclear attack: What would happen? What should we do?" *Bulletin of the Atomic Scientists*, vol. 74, no. 2, pp. 114–119, 2018. [Online]. Available: https://doi.org/10.1080/00963402.2018.1436812

[17] "Radiation portal monitors: DHS's fleet is lasting longer than expected , and future acquisitions focus on operational efficiencies," Oct. 2016. [Online]. Available: https://www.gao.gov/assets/690/680706.pdf

[18] G. T. Simon Shuster, "Inside the Uranium Underworld: Dark Secrets, Dirty Bombs," Apr. 2017. [Online]. Available: https://time.com/4728293/uranium-underworld-dark-secrets-dirty-bombs/

[19] R. C. M. Charles Meade, "Considering the Effects of a Catastrophic Terrorist Attack," RAND Corporation, Tech. Rep., 2006. [Online]. Available: https://www.rand.org/content/dam/rand/pubs/technical_reports/2006/RAND_TR391.pdf

[20] "CNS Global Incidents and Trafficking Database - Tracking publicly reported incidents involving nuclear and other radioactive materials," Jul.

2019. [Online]. Available: https://media.nti.org/documents/global_incidents_trafficking_2018.pdf

[21] "Decriminalization of the voluntary radioactive sources disposal," 2019. [Online]. Available: https://uatom.org/index.php/en/project-amnesty/

[22] "CSI: Container Security Initiative," May 2019. [Online]. Available: https://www.cbp.gov/border-security/ports-entry/cargo-security/csi/csi-brief

[23] "Non-Intrusive Inspection and Radiation Detection Equipment Program: FY 2015 in Review," May 2016. [Online]. Available: https://www.hsdl.org/?view&did=795092

[24] T. O. Dennis Michelini, Scott Luck, "Written testimony of CBP Office of Field Operations Executive Assistant Commissioner Todd Owen, CBP U.S. Border Patrol Acting Deputy Chief Scott Luck, and CBP Air and Marine Operations, Operations Acting Executive Director Dennis Michelini for a House Committee on Homeland Security, Subcommittee on Border and Maritime Security hearing titled "Deter, Detect and Interdict: Technology's Role in Securing the Border"," Jul. 2017.

[25] M. Kauchak *et al.*, "X-Ray Specs: X-Ray Surveillance and Dangerous Cargo," Apr. 2018. [Online]. Available: https://www.passportsystems.com/pg/company/graphics/passport-systems-article-in-safety-security-international-magazine

[26] "Mobile VACIS Inspection System," Feb. 2005. [Online]. Available: http://www.saic.com/products/security/mobile-vacis/mobile-tech.html

[27] "Mobile Inspection System VACIS M6500," Apr. 2015. [Online]. Available: https://www.leidos.com/insights/mobile-inspection-system-vacisr-m6500

[28] "VACIS P7500 Imaging System Overview," Apr. 2007. [Online]. Available: http://www.saic.com/products/security/pdf/VACIS-P-7500.pdf

[29] "Domestic Nuclear Detection Office," Jun. 2015. [Online]. Available: https://www.dhs.gov/domestic-nuclear-detection-offic

[30] "Model 4525-17500 Radiation Portal Monitor," Aug. 2014. [Online]. Available: https://ludlums.com/images/data_sheets/M4525-17500.pdf

[31] "Global Trade: Trade Statistics," 2019. [Online]. Available: http://www.worldshipping.org/about-the-industry/global-trade/trade-statistics

[32] "Monthly U.S. international trade in goods," Sep. 2019. [Online]. Available: https://www.census.gov/foreign-trade/press-release/current_press_release/ft900.pdf

[33] "TSA TM850 Portal monitor for radiation inspection of large vehicles and trains, especially with dense cargo," 2019. [Online]. Available: https://www.rapiscansystems.com/en/products/tsa-tm850

[34] "TSA VM250 The TSA VM250 automatically screens vehicular traffic without the need for frequent calibration," 2019. [Online]. Available: https://www.rapiscansystems.com/en/products/tsa-vm250

[35] D. Cester, G. Nebbia, L. Stevanato, G. Viesti, F. Neri, S. Petrucci, S. Selmi, C. Tintori, P. Peerani, and A. Tomanin, "Special nuclear material detection with a mobile multi-detector system," *Nuclear Instruments and Methods in Physics Research Section A: Accelerators, Spectrometers, Detectors and Associated Equipment*, vol. 663, no. 1, pp. 55 – 63, 2012. [Online]. Available: http://www.sciencedirect.com/science/article/pii/S0168900211019012

[36] S. Fetter, V. A. Frolov, M. Miller, R. Mozley, O. F. Prilutsky, S. N. Rodionov, and R. Z. Sagdeev, "Detecting nuclear warheads," *Science & Global Security*, vol. 1, no. 3-4, pp. 225–253, 1990. [Online]. Available: https://doi.org/10.1080/08929889008426333

[37] "Efficiency calculations for selected scintillators," 2016. [Online]. Available: https://www.crystals.saint-gobain.com/sites/imdf.crystals.com/files/documents/efficiency-calculations.pdf

[38] "Technical specification for steel dry cargo container 20' x 8' x 9'6" high cube," 2012. [Online]. Available: http://www.steinecker-container.de/container/Container2/Spez-Container/Spez_high%20cube20.pdf

[39] "Working environments," 2016. [Online]. Available: https://www.iroctech.com/library/working-environments/

[40] D. M. S. Richard T. Kouzes, Joseph C. McDonald and S. M. Dowyer, *Radiation detection and interdiction at U.S. borders*. New York : Oxford University Press, 2011, includes bibliographical references and index.

[41] R. Kouzes, "Passive and Active Radiation Detection for National Security," Dec. 2017, presentation at MIT.

[42] "Active interrogation standards," Jan. 2018. [Online]. Available: https://www.nist.gov/programs-projects/active-interrogation-standards

[43] R. C. Runkle, D. L. Chichester, S. J. Thompson *et al.*, "Rattling nucleons: New developments in active interrogation of special nuclear material," *Nucl. Instrum. Meth.*, vol. A 663, no. 1, pp. 75–95, 2012.

[44] H. W. Koch, J. McElhinney, and E. L. Gasteiger, "Experimental Photo-Fission Thresholds in ${}_{92}U^{235}$, ${}_{92}U^{238}$, ${}_{92}U^{233}$, ${}_{94}Pu^{239}$, and ${}_{90}Th^{232}$," *Phys. Rev.*, vol. 77, pp. 329–336, Feb 1950. [Online]. Available: https://link.aps.org/doi/10.1103/PhysRev.77.329

[45] V. V. Verbinski, H. Weber, and R. E. Sund, "Prompt Gamma Rays from ^{235}U(n, f), ^{239}Pu(n, f), and Spontaneous Fission of ^{252}Cf," *Phys. Rev. C*, vol. 7, pp. 1173–1185, Mar 1973. [Online]. Available: https://link.aps.org/doi/10.1103/PhysRevC.7.1173

[46] T. Gozani, "Fission signatures for nuclear material detection," *IEEE Transactions on Nuclear Science*, vol. 56, no. 3, pp. 736–741, June 2009.

[47] T. England and B. Rider, "Evaluation and compilation of fission product yields 1993," Los Alamos National Laboratory, Tech. Rep., 12 1995.

[48] T. Gozani, T. Shaw, M. J. King, J. Stevenson, M. Elsalim, C. Brown, and C. Condron, "Combined Photoneutron And X Ray Interrogation Of Containers For Nuclear Materials," *AIP Conference Proceedings*, vol. 1336, no. 1, pp. 686–692, 2011. [Online]. Available: https://aip.scitation.org/doi/abs/10.1063/1.3586190

[49] W. Bertozzi, S. E. Korbly, R. J. Ledoux, and W. Park, "Nuclear resonance fluorescence and effective Z determination applied to detection and imaging of special nuclear material, explosives, toxic substances and contraband," *Nuclear Instruments and Methods in Physics Research Section B: Beam Interactions with Materials and Atoms*, vol. 261, no. 1, pp. 331 – 336, 2007, the Application of Accelerators in Research and Industry. [Online]. Available: http://www.sciencedirect.com/science/article/pii/S0168583X07007185

[50] "Z backscatter," 2019. [Online]. Available: https://www.rapiscan-ase.com/resource-center/technology/z-backscatter

[51] M. Chadwick *et al.*, "ENDF/B-VII.1 Nuclear Data for Science and Technology: Cross Sections, Covariances, Fission Product Yields and Decay Data," *Nuclear Data Sheets*, vol. 112, no. 12, pp. 2887 – 2996, 2011, Special Issue on ENDF/B-VII.1 Library. [Online]. Available: http://www.sciencedirect.com/science/article/pii/S009037521100113X

[52] B. W. Blackburn, Gongyin Chen, W. A. Franklin, E. E. Ihloff, G. E. Kohse, R. C. Lanza, B. McAllister, D. R. Perticone, and V. Ziskin, "Fast neutron resonance radiography for homeland security," in *2007 IEEE Nuclear Science Symposium Conference Record*, vol. 2, Oct 2007, pp. 1016–1020.

[53] W. Leo *et al.*, *Techniques for Nuclear and Particle Physics Experiments*. Springer-Verlag Berlin Heidelberg, 1994.

[54] S. Ogorodnikov and V. Petrunin, "Processing of interlaced images in 4-10 MeV dual energy customs system for material recognition," *Phys. Rev. ST Accel. Beams*, vol. 5, p. 104701, 2002.

[55] G. Chen, G. Bennett, and D. Perticone, "Dual-energy X-ray radiography for automatic high-Z material detection," *Nucl. Instrum. Meth.*, vol. A 261, no. 1-2, pp. 356–359, 2007.

[56] J. L. Jones, J. W. Sterbentz, W. Y. Yoon, and D. R. Norman, "Bremsstrahlung versus Monoenergetic Photon Dose and Photonuclear Stimulation Comparisons at Long Standoff Distances," *AIP Conference Proceedings*, vol. 1194, no. 1, pp. 43–48, 2009. [Online]. Available: https://aip.scitation.org/doi/abs/10.1063/1.3275665

[57] F. H. Attix, *X-Ray Production and Quality*. John Wiley & Sons, Ltd, 2007. [Online]. Available: https://onlinelibrary.wiley.com/doi/abs/10.1002/9783527617135.ch9

[58] "Rapiscan Eagle P60 Cargo Inspection System," 2012. [Online]. Available: http://itt-kubba.com/products2/eagle/P60/Rapiscan%20Eagle%20P60%20Product%20Overview%20040910.pdf

[59] "Q-value Calculator (QCalc)," 2012. [Online]. Available: https://www.nndc.bnl.gov/qcalc/index.jsp

[60] J. Kiener, M. Berheide, N. L. Achouri, A. Boughrara, A. Coc, A. Lefebvre, F. de Oliveira Santos, and C. Vieu, "γ-ray production by inelastic proton scattering on ^{16}O and ^{12}C," *Phys. Rev. C*, vol. 58, pp. 2174–2179, Oct 1998. [Online]. Available: https://link.aps.org/doi/10.1103/PhysRevC.58.2174

[61] R. W. Peelle, "Differential Cross Sections for the Scattering of Medium Energy Protons on Carbon," *Phys. Rev.*, vol. 105, pp. 1311–1323, Feb 1957. [Online]. Available: https://link.aps.org/doi/10.1103/PhysRev.105.1311

[62] J. Kiener, N. de Séréville, and V. Tatischeff, "Shape of the 4.438 MeV γ-ray line of ^{12}C from proton and α-particle induced reactions on ^{12}C and ^{16}O," *Phys. Rev. C*, vol. 64, p. 025803, Jun 2001. [Online]. Available: https://link.aps.org/doi/10.1103/PhysRevC.64.025803

[63] P. Dyer, D. Bodansky, A. G. Seamster, E. B. Norman, and D. R. Maxson, "Cross sections relevant to gamma-ray astronomy: Proton induced reactions," *Phys. Rev. C*, vol. 23, pp. 1865–1882, May 1981. [Online]. Available: https://link.aps.org/doi/10.1103/PhysRevC.23.1865

[64] M. J. LeVine and P. D. Parker, "A Study of $T = \frac{3}{2}$ States in N^{13}," *Phys. Rev.*, vol. 186, pp. 1021–1037, Oct 1969. [Online]. Available: https://link.aps.org/doi/10.1103/PhysRev.186.1021

[65] B. A. Watson, R. E. Segel, J. J. Kroepel, and P. P. Singh, "Inelastic Scattering of Protons from B^{10} between 5 and 16.5 MeV," *Phys. Rev.*, vol. 187, pp. 1351–1364, Nov 1969. [Online]. Available: https://link.aps.org/doi/10.1103/PhysRev.187.1351

[66] A. Lagoyannis, K. Preketes-Sigalas, M. Axiotis, V. Foteinou, S. Harissopulos, M. Kokkoris, P. Misaelides, V. Paneta, and N. Patronis, "Study of the 10b(p,$\alpha\gamma$)7be and 10b(p,p'γ)10b reactions for pige purposes," *Nuclear*

Instruments and Methods in Physics Research Section B: Beam Interactions with Materials and Atoms, vol. 342, pp. 271 – 276, 2015. [Online]. Available: http://www.sciencedirect.com/science/article/pii/S0168583X14008593

[67] F. Alves, M. Jensen, H. Jensen, R. Nickles, and S. Holm, "Determination of the excitation function for the 10B(p,n)10C reaction with implications for the production of [10C]carbon dioxide for use as a PET tracer," *Applied Radiation and Isotopes*, vol. 52, no. 4, pp. 899 – 903, 2000. [Online]. Available: http://www.sciencedirect.com/science/article/pii/S0969804399001402

[68] C. Boni, E. Cereda, G. Marcazzan, and V. D. Tomasi, "Prompt gamma emission excitation functions for PIGE analysis," *Nuclear Instruments and Methods in Physics Research Section B: Beam Interactions with Materials and Atoms*, vol. 35, no. 1, pp. 80 – 86, 1988. [Online]. Available: http://www.sciencedirect.com/science/article/pii/0168583X88901012

[69] L. van Der Zwan and K. Geiger, "The 11B(p, n)11C cross section from threshold to 4.9 MeV," *Nuclear Physics A*, vol. 306, no. 1, pp. 45 – 52, 1978. [Online]. Available: http://www.sciencedirect.com/science/article/pii/037594747890310X

[70] C. Class, J. Price, and J. Risser, "Angular distributions from the 11B(d, n0)12C and 11B(d, n1)12*C reactions for deuteron energies from 1.5 to 4.7 MeV," *Nuclear Physics*, vol. 71, no. 2, pp. 433 – 440, 1965. [Online]. Available: http://www.sciencedirect.com/science/article/pii/0029558265907303

[71] R. Ramaty, B. Kozlovsky, and R. E. Lingenfelter, "Nuclear gamma-rays from energetic particle interactions." *Astrophysical Journal Supplement Series*, vol. 40, pp. 487–526, Jul 1979.

[72] A. Caciolli, M. Chiari, A. Climent-Font, M. Fernandez-Jimenez, G. Garcia-Lopez, F. Lucarelli, S. Nava, and A. Zucchiatti, "Measurements of γ-ray emission induced by protons on fluorine and lithium," *Nuclear Instruments and Methods in Physics Research Section B: Beam Interactions with Materials and Atoms*, vol. 249, no. 1, pp. 98 – 100, 2006, ion Beam Analysis. [Online]. Available: http://www.sciencedirect.com/science/article/pii/S0168583X06003697

[73] F. Riffle, J. Goss, D. Parsignault, and J. Harris, "Measurement of the absolute total cross section for the reaction 19F(p, n)19Ne," *Nuclear Physics A*, vol. 115, no. 1, pp. 120 – 128, 1968. [Online]. Available: http://www.sciencedirect.com/science/article/pii/0375947468906465

[74] J. L. Jones, J. W. Sterbentz, W. Y. Yoon, D. R. Norman, and D. W. Gerts, "Bremsstrahlung versus monoenergetic photons for photonuclear inspection applications," 2008. [Online]. Available: https://www.osti.gov/servlets/purl/950053

[75] A. Danagoulian, "grasshopper: A simple geant4 application," Dec. 2017. [Online]. Available: https://github.mit.edu/LNSP/grasshopper

[76] S. Agostinelli *et al.*, "GEANT4: A simulation toolkit," *Nucl. Instrum. Meth.*, vol. A 506, pp. 250–303, 2003.

[77] J. Bendahan, "Vehicle and Cargo Scanning for Contraband," *Physics Procedia*, vol. 90, pp. 242 – 255, 2017, conference on the Application of Accelerators in Research and Industry, CAARI 2016, 30 October - 4 November 2016, Ft. Worth, TX, USA. [Online]. Available: http://www.sciencedirect.com/science/article/pii/S1875389217301621

[78] P. B. S. V. K. R. C. L. V. P. Anatoli Arodzero, Salime Boucher, "Security X-ray Screening with Modulated-Energy Pulses," 2019. [Online]. Available: http://www.hstabstractbook.org/index_htm_files/c-PID6138357.pdf

[79] S. Kutsaev, R. Agustsson, A. Arodzero, S. Boucher, L. Faillace, J. Hartzell, and V. Ziskin, "Electron linac with deep energy control for Adaptive Rail Cargo Inspection System," in *2015 IEEE Nuclear Science Symposium and Medical Imaging Conference (NSS/MIC)*, Oct 2015, pp. 1–7.

[80] "What You Can Do with a Class B Driver's License," 2019. [Online]. Available: https://www.idrivesafely.com/defensive-driving/trending/what-you-can-do-class-b-drivers-license

[81] "What are the various vehicle weight classes and why do they matter?" Apr. 2016. [Online]. Available: http://nhcleancities.org/2016/04/various-vehicle-weight-classes-matter/

[82] "Commercial motor vehicle classification," Aug. 2019. [Online]. Available: https://www.thebalancesmb.com/commercial-motor-vehicle-classification-2221025

[83] J. Henderson, "How Much Does a Ford F650 Weigh? 15 Examples of Curb Weights," 2017. [Online]. Available: https://truckomize.com/how-much-does-ford-f650-weigh/

[84] "Tandem Van de Graaff," Feb. 2008. [Online]. Available: https://web.archive.org/web/20100219001009/http://www.bnl.gov/bnlweb/facilities/TVdG.asp

[85] "Cyclone KIUBE," Jul. 2017. [Online]. Available: https://www.iba-radiopharmasolutions.com/sites/default/files/resources/files/cbr_cyclone_kiube_v2_r05.pdf

[86] "Cyclone 30," 2010. [Online]. Available: https://www.iba-radiopharmasolutions.com/sites/default/files/resources/files/cbr_c30_v5_r00.pdf

[87] "Zach Hartwig: Applying diverse skills in pursuit of a fusion breakthrough," May 2017. [Online]. Available: http://news.mit.edu/2017/mit-assistant-professor-zach-hartwig-applying-diverse-skills-in-pursuit-of-nuclear-fusion-breakthrough-0522

[88] Z. Charifoulline, "Residual Resistivity Ratio (RRR) Measurements of LHC Superconducting NbTi Cable Strands," *IEEE Transactions on Applied Superconductivity*, vol. 16, no. 2, pp. 1188–1191, June 2006.

[89] X. Wu *et al.*, "Recent Progress in R&D for Ionetix Ion-12SC Superconducting Cyclotron for Production of Medical Isotopes," in *Proc. 10th International Particle Accelerator Conference (IPAC'19), Melbourne, Australia, 19-24 May 2019*, ser. International Particle Accelerator Conference, no. 10. Geneva, Switzerland: JACoW Publishing, Jun. 2019, paper THPMP052, pp. 3568–3570, https://doi.org/10.18429/JACoW-IPAC2019-THPMP052. [Online]. Available: http://jacow.org/ipac2019/papers/thpmp052.pdf

[90] J. Vincent, G. Blosser, G. Horner, K. Stevens, N. Usher, X. Wu, S. Vorozhtsov, and V. Smirnov, "The ionetix ion-12sc compact superconducting cyclotron for production of medical isotopes," Sep. 2016.

[91] X. Wu, "The ION-12SC Compact Superconducting Cyclotron for Production of Medical Isotopes," 2016. [Online]. Available: http://accelconf.web.cern.ch/AccelConf/cyclotrons2016/talks/thb02_talk.pdf

[92] "Pulse tube crycoolers," 2019. [Online]. Available: https://www.cryomech.com/cryocoolers/pulse-tube-cryocoolers/

[93] ""WAT" Series Chillers," 2017. [Online]. Available: http://www.fluidchillers.com/index.php?option=com_content&view=article&id=5&Itemid=10

[94] "PT415 Cryorefrigerator Capacity Curve," Nov. 2018. [Online]. Available: https://www.cryomech.com/wp-content/uploads/2018/11/PT415-CPA1110-Capacity-Curve.pdf

[95] D. Benford, T. Powers, and S. Moseley, "Thermal conductivity of kapton tape," *Cryogenics*, vol. 39, no. 1, pp. 93 – 95, 1999. [Online]. Available: http://www.sciencedirect.com/science/article/pii/S0011227598001258

[96] "Thermal conductivity." [Online]. Available: http://hyperphysics.phy-astr.gsu.edu/hbase/Tables/thrcn.html

[97] "ASP-2 General Purpose Survey Meter," Franklin, MA, 2007. [Online]. Available: http://www.thermo.com.cn/Resources/200802/productPDF_22585.pdf

[98] "Model 9DP-1 Ion Chamber Survey Meter," Sweetwater, TX, feb 2019. [Online]. Available: https://ludlums.com/images/data_sheets/M9DP-1.pdf

[99] M. Z. M.J. Berger, J.S. Coursey and J. Chang, "ESTAR, PSTAR, and ASTAR: Computer Programs for Calculating Stopping-Power and Range Tables for Electrons, Protons, and Helium Ions (version 1.2.3)," Gaithersburg, MD, 2017. [Online]. Available: https://www.nist.gov/pml/stopping-power-range-tables-electrons-protons-and-helium-ions

[100] S. Kobayashi, "Elastic and Inelastic Scattering of Protons by Oxygen in the Energy Region of 6.9 MeV to 15.6 MeV," *Journal of the Physical Society of Japan*, vol. 15, no. 7, pp. 1164–1174, 1960. [Online]. Available: https://doi.org/10.1143/JPSJ.15.1164

[101] "Model: Air3000 standard chiller specifications," 2018. [Online]. Available: http://www.fluidchillers.com/images/Air_Cooled_Chillers_PDF/AIR3000_2017.pdf

[102] "LaBr3 - 1.5 x 1.5 Lanthanum Bromide Scintillation Detector," Meriden CT, 2019. [Online]. Available: https://www.mirion.com/products/labr3-15-x-15-lanthanum-bromide-scintillation-detector

[103] "Brillance® 380 crystal lanthinum bromide labr3(ce)," Malvern, PA, 2019. [Online]. Available: https://www.crystals.saint-gobain.com/products/standard-and-enhanced-lanthanum-bromide

[104] "V1725 16/8 Channel 14-bit 250 MS/s Digitizer," Viareggio, Italy. [Online]. Available: http://www.caen.it/csite/CaenProd.jsp?parent=11&idmod=952

[105] Z. S. Hartwig, "The ADAQ framework: An integrated toolkit for data acquisition and analysis with real and simulated radiation detectors," *Nucl. Instrum. Meth.*, vol. A 815, no. Supplement C, pp. 42 – 49, 2016. [Online]. Available: http://www.sciencedirect.com/science/article/pii/S0168900216000206

[106] "NuDat 2.7 database," 2016. [Online]. Available: http://www.nndc.bnl.gov/nudat2/

[107] J. Nattress, F. Sutanto, P. W. Fang, Y. Z. Chen, A. Chen, K. Y. Chu, T. S. Duh, H. Y. Tsai, M. W. Lin, and I. Jovanovic, "Characterization of the ^{12}c(p,p')^{12}c reaction (e_p=19.5–30 mev) for active interrogation," 2019.

[108] Z. Janout, S. Pospíšil, and M. Vobecký, "Observation of a Doppler broadening of the 4438 keV gamma-line of 12C in processes 12C(n, n$\prime\gamma$)12C and 9Be(α, nγ)12C," *Journal of Radioanalytical Chemistry*, vol. 56, no. 1, pp. 71–81, Mar 1980. [Online]. Available: https://doi.org/10.1007/BF02516939

[109] J. J. Kolata, R. Auble, and A. Galonsky, "Excitation Energy of the First Excited State of C^{12}, and Observation of a Coherent Doppler Effect," *Phys. Rev.*, vol. 162, pp. 957–962, Oct 1967. [Online]. Available: https://link.aps.org/doi/10.1103/PhysRev.162.957

[110] S. Devons, G. Manning, and J. H. Towle, "Measurement of -transition lifetimes by recoil methods III: E2 transitions in some even-even nuclei," *Proceedings of the Physical Society. Section A*, vol. 69, no. 2, pp. 173–177, feb 1956. [Online]. Available: https://doi.org/10.1088%2F0370-1298%2F69%2F2%2F311

[111] R. Brun and F. Rademakers, "ROOT - an object oriented data analysis framework," *Nucl. Instrum. Meth.*, vol. A 389, no. 1-2, pp. 81 – 86, 1997, new Computing Techniques in Physics Research. [Online]. Available: http://www.sciencedirect.com/science/article/pii/S016890029700048X

[112] "TSpectrum Class Reference," Feb. 2020. [Online]. Available: https://root.cern.ch/doc/master/classTSpectrum.html#a7830480612d1ee301964e6c79319f444

[113] M. Caccia, A. Ebolese, M. Maspero, R. Santoro, M. Locatelli, M. Pieracci, and C. Tintori, "Background removal procedure based on the SNIP algorithm for γ-ray spectroscopy with the CAEN Educational Kit," Viareggio, Italy, Oct. 2017. [Online]. Available: https://www.caen.it/wp-content/uploads/2017/10/ED3163_gamma_spectroscopy_CAEN_edu_kit.pdf

[114] C. Ryan, E. Clayton, W. Griffin, S. Sie, and D. Cousens, "SNIP, a statistics-sensitive background treatment for the quantitative analysis of PIXE spectra in geoscience applications," *Nuclear Instruments and Methods in Physics Research Section B: Beam Interactions with Materials and Atoms*, vol. 34, no. 3, pp. 396 – 402, 1988. [Online]. Available: http://www.sciencedirect.com/science/article/pii/0168583X88900638

[115] M. Morhac, J. Kliman, V. Matousek, M. Veselsky, and I. Turzo, "Background elimination methods for multidimensional coincidence γ-ray spectra," *Nuclear Instruments and Methods in Physics Research Section A: Accelerators, Spectrometers, Detectors and Associated Equipment*, vol. 401, no. 1, pp. 113 – 132, 1997. [Online]. Available: http://www.sciencedirect.com/science/article/pii/S0168900297010231

[116] "TMinuit Class Reference," Feb. 2020. [Online]. Available: https://root.cern.ch/doc/master/classTMinuit.html

[117] "Easy-to-Machine Gray Cast Iron," 2019. [Online]. Available: https://www.mcmaster.com/8923k81

[118] IEEE, "American National Standard for Determination of the Imaging Performance of X-Ray and Gamma-Ray Systems for Cargo and Vehicle Security Screening," *ANSI N42.46-2008*, pp. 1–35, Aug 2008.